

Advanced Characterization of Materials for Superconducting Radiofrequency Accelerator Cavities

James Robert Tuggle Jr.

Dissertation submitted to the faculty of the Virginia Polytechnic Institute and State
University in partial fulfillment of the requirements for the degree of

Doctor of Philosophy

In

Materials Science and Engineering

Michael J. Kelley, Chair

William T. Reynolds Jr.

Fred A. Stevie

Charles E. Reece

Alex. O. Aning

April 4, 2019

Blacksburg, Virginia, USA

Keywords: Materials Characterization, SIMS, EBSD, XPS, SRF, nitrogen doping, Nb₃Sn

Copyright 2019, Jay Tuggle

Advanced Characterization of Materials for Superconducting Radiofrequency Accelerator Cavities

James Robert Tuggle Jr.

Abstract

Particle accelerators are a leading tool for frontier science. Pushing that frontier further demands more machines with higher performance, and more of a very expensive technology: superconducting radio-frequency (SRF) acceleration. From a materials perspective this means reducing residual surface resistance or raising the operating temperature (currently ~ 2 K) of SRF cavities. Both are pursued by materials modification: nitrogen doping/infusion in the first instance and coating with Nb₃Sn in the second. Materials characterization is key to achieving understanding and directing R&D. However, very little has been done. This present work aims to fill the knowledge gap and to provide needed, validated tools to the accelerator science community. In this connection, SIMS, XPS and EBSD have proven especially valuable and represent the majority of discussion in this dissertation.

Advanced Characterization of Materials for Superconducting Radiofrequency Accelerator Cavities

James Robert Tuggle Jr.

General Audience Abstract

Particle accelerators are a powerful tool that helps us expand our knowledge of science and how the universe works. Pushing that knowledge further requires us to use more and more powerful particle accelerators. Particle accelerators are based on a very expensive technology: superconducting radio-frequency (SRF) cavities. These cavities are hollow tubes made from niobium and shaped in such a way as to cause electromagnetic waves to form. These waves are what are used to accelerate particles. The energy input and loss of energy as heat are massive resulting in millions of dollars a year in electric bills at particle accelerator facilities. In order to build bigger and more powerful particle accelerators they must be more efficient or they become prohibitively expensive. In this dissertation I look at several next generation materials used in building particle accelerators. In particular I describe and go into detail about how to characterize these materials. In other words, how we determine the materials properties and how those properties affect the performance.

Acknowledgements

I have been lucky, the list of folks that have positively influenced my life and led me here is long; To thank them all for their contributions would take pages.

I must thank Dr. Michael J. Kelley. When I began graduate school, I was looking for a place to expand, learn, and be mentored. After a few bumps in the road I found my way to Dr. Kelley's group and found what I was looking for. During my time in his group he has been a wealth of knowledge with a practical approach to research and teaching. For me he has been the epitome of a professor and mentor.

I would also like to thank the members of my committee. In particular Fred Stevie, who reviews papers at warp speed and has also proved a wealth of knowledge. Without his book on SIMS and pragmatic teachings I would have never made it out of the gate with the instrument.

I would like to thank Dr. Francis Webster and Dr. Cindy Burkhardt. They are the gold standard for what a professor should be. The perfect mix of teacher, mentor, challenger, and friend. The quality of my undergraduate education had a profound effect on my path and gave me a leg-up over many not lucky enough to have the two of them.

I would like to wholeheartedly thank my family.

My wife, Samantha Tuggle, who has absolutely been the support structure and glue that has held our life together and kept it on track during my time in graduate school. She has played the roll of motivator, therapist, coach, investor, and sounding board, all while being an amazing wife and best friend.

My grandmother, Glenda Tuggle, for always believing, having positive words, and generally teaching me how to be a decent person.

My father, Bob Tuggle, for teaching me to successfully navigate the system when the system doesn't fit and always finding a way to be on my side even when my side was the grey area.

My grandfather, Paul Tuggle, who put tools in my hand as soon as I could hold them. He gave me the opportunity and freedom to build what I could imagine. He taught me tools, machines, and equipment are there to ease your task and improve your results, and that they are not limited by their design, but can and should be modified towards this purpose. He was my first engineering professor and I see him every time I walk in a shop or open a toolbox. This is dedicated to him and he would dig it.

Contents

1 Introduction	12
1.1 Motivation and Significance.....	12
1.2 Research Objectives:	13
1.3 Structure of this Dissertation.....	13
2 Background and Current State of Nitrogen addition	14
2.1 Paradigm Shift: (2013-2016).....	14
2.2 The Diffusion of Nitrogen into Niobium.....	15
2.3 Mechanics Behind N-doping's Cavity Enhancement.....	17
2.4 Low Temperature Doping	22
3 Background and Current State of Nb₃Sn Cavity Coating.....	23
3.1 The 4.2 K Goal	23
4 Secondary Ion Mass Spectrometry for Superconducting Radiofrequency Cavity Materials.....	24
4.1 Introduction	24
4.1.1 Motivation for Work with SRF Materials	24
4.1.2 Secondary Ion Mass Spectrometry.....	25
4.2 Experimental	31
4.2.1 Secondary Ion Mass Spectrometry.....	31
4.2.2 Sample Holder.....	32
4.2.3 Samples and Treatments.....	32
4.3 Results and Discussion.....	33
4.3.1 High Doping Temperature.....	33
4.3.2 Low Temperature Doping	34
4.3.3 As-Received Cavity Materials.....	35
4.3.4 N-Doping Orientation Dependency.....	36
4.3.5 Nb ₃ Sn Contamination.....	39
4.4 Conclusion.....	40
4.5 Acknowledgement.....	41
Appendix A	41
A.1 Orientation Effects on Doping Supplemental	41
5 XPS for SRF Cavity Materials: Determining Material Composition as a Function of Depth	43
5.1 Introduction	43
5.1.1 Motivation	43
5.2 Experimental	44
5.2.1 X-ray Photoelectron Spectroscopy.....	44

5.2.2	Samples	44
5.3	Results and Discussion	45
5.3.1	Sampling Depth	45
5.3.2	Depth Profiling of Nitrogen Doped Niobium	47
5.3.3	Angle Polishing	49
5.3.4	Depth Profiling of Nb ₃ Sn	51
5.3.5	Dependence of Preferential Sputtering on Ion Beam Condition	52
5.3.6	Error in Nb ₃ Sn Depth Profiling Measurements	53
5.4	Conclusion	53
5.5	Acknowledgements	54
	Appendix B	54
B.1	XPS for Surface Characterization of Nb ₃ Sn	54
B.2	XPS of Anodized Nb ₃ Sn	56
B.3	XPS for Nucleation Study	58
B.4	EDS Cross-Section Analysis as an Alternative to XPS Depth Profile	59
6	Electron Backscatter Diffraction of Nb₃Sn Coated Niobium: Revealing Structure as a Function of Depth	64
6.1	Introduction	64
6.1.1	Motivation for Work with SRF Materials	64
6.1.2	Electron Backscatter Diffraction	65
6.2	Experimental	67
6.2.1	Materials	67
6.2.2	Electron Backscatter Diffraction	67
6.3	Results and Discussion	73
6.3.1	Coating Dependence on Cavity Geometry	73
6.3.2	Orientation Dependence of Nb ₃ Sn	74
6.3.3	Patch Defects	75
6.3.4	Surface Anodization Effect on Coating	76
6.3.5	The Initial Overcoat Experiment	80
6.3.6	Continuation of the Overcoat Experiment	81
6.4	Conclusion	83
6.5	Acknowledgment	84
7	Summary and Recommendations	85
	Bibliography	87

List of Figures

Figure 1.1 Image showing 9-cell SRF cavity design for the LCLS-II currently under construction at the SLAC National Accelerator Laboratory.....	12
Figure 2.1 Phase diagram of the nitrogen/niobium system. [15].....	15
Figure 2.2 Arrhenius plot. Line marked D_m shows nitrogen in metal, while line marked $[kp]_{\xi n}$ represents nitride growth. The lower two lines represent the nitridation kinetics. [16]	16
Figure 2.3 Diagram showing nitrogen diffusion profile in both nitride and bulk niobium. [16].....	17
Figure 2.4 Shows comparison of quality factors as a function of the RF accelerating field for several N-doped cavities and a cavity prepared under normal/standard conditions. [6]	18
Figure 2.5 Decoupled R_{BCS} and R_{Res} values as a function of field strength for several different cavity preparations. [6].....	19
Figure 2.6 R_{Res} as a function of trapped flux and as a function of applied magnetic field. [28].....	19
Figure 2.7 R_{Res} as a function of trapped flux for different cavity preparations. Taking the slope provides magnetic flux sensitivity. [30]	20
Figure 2.8 Sensitivity to trapped flux as a function of MFP. [31].....	20
Figure 2.9 Performance of over doped cavity with differing amounts of material removal. [32].....	21
Figure 2.10 R_{BCS} and trapped flux induced resistance as a function of MFP for cavities doped and un-doped. Red shading shows approximate results for 2/6 doping recipe. [33]	21
Figure 2.11 Comparison of Q_0 curves for different heat treatments in the range 160-200 °C, referenced to standard 120 °C bake post oxidation. [34]	22
Figure 4.1 Depth profile of N-doped niobium with EP surface. Specimen was sputter coated with Pt/Pd prior to depth profiling.	26
Figure 4.2 Depth profile of nitrogen implants used to calibrate nitrogen for both polycrystalline and single crystal material.....	27
Figure 4.3 A and B show depth profiles with measured nitrogen concentration (parts per thousand atomic) from N-doped BCP and NP samples.....	28
Figure 4.4 Raster reduction to check source of the ions detected for nitrogen and oxygen.	29
Figure 4.5 Mass spectra, one showing a sample with clearly resolved peaks (blue) and one suffering from metastable hydride interference (orange).	31

Figure 4.6 Schematic of Cameca IMS7f-GEO. Reprinted with permission from CAMECA®.	31
Figure 4.7 (A) Example of nitrides forming on surface of N-doped sample. (B) Shows a cross-section of a sample N-doped at 900 °C for 10 minutes at ~25 mTorr.....	33
Figure 4.8 SIMS analyses of niobium samples doped at varying temperatures.	34
Figure 4.9 SIMS analysis of low temperature doped sample (L81) and undoped sample (L82) in the near surface (first 50 nm).....	35
Figure 4.10 Oxygen and Nitrogen quantification with error for “as-received” samples. .	36
Figure 4.11 Illustration of crater placement, optical images of craters, and depth profile data from SIMS analysis of N-doped (900°C, 10 mins, ~25 mTorr N) bicrystal sample.	37
Figure 4.12 Image showing surface of 700 °C N-doped sample (A) and lightly sputtered (focused gallium ion beam, FEI Helios 600) area of 900 °C N-doped sample (B). Both show clear differences in nitride formation from grain to grain.....	37
Figure 4.13 SIMS results from bi-crystalline samples doped at different temperatures. Grain A and B represent two sides of a grain boundary.	38
Figure 4.14 Inverse pole figures showing overlays of data collected from grains A and B for the 700 °C and 900°C bi-crystalline samples.	39
Figure 4.15 SIMS depth profile of Ti in Nb ₃ Sn coated coupons.	40
Figure A.1 Figure showing steps for grain/orientation specific SIMS analysis. (A) Optical image of 250 x 250 micron grid placed on sample surface using FIB. (B) SEM image of the same grid. (C) EBSD map of grain orientation laid over the grid pattern. (C) SIMS analysis of eight different grains/orientations within the mapped area.	42
Figure 5.1 XPS survey scan of 900 oC polycrystalline N-doped niobium coupon.	45
Figure 5.2 XPS depth profile of 900 °C doped sample. Depth profile is based on high resolution scans performed alternating with argon sputtering of the sample.	47
Figure 5.3 High resolution scans of (A) oxygen, (B) nitrogen, and (C) niobium from depth profile of a 900°C doped polycrystalline sample (Figure 5.2).....	48
Figure 5.4 Two high energy resolution scans covering the Nb3p and N1s binding energies, one from a niobium coupon which has been N-doped (shows N1s) and one which has not been doped.	49
Figure 5.5 Graphic representing angle polished sample; Blue represents N-dope profile, Solid black line shows original surface of the sample, dashed black line shows newly created polished surface used for analysis at varying depths.	50
Figure 5.6 Angle polished sample with 150x150 μm analysis craters spaced along the polished surface. Giving analysis at different depths.	50
Figure 5.7 Concentration vs Depth plot for SIMS analysis of angle polished sample (700 °C N-doped).	51
Figure 5.8 : Depth profile of a niobium coupon coated with Nb ₃ Sn. Analyzed by XPS with argon sputtering used for material removal.	52

Figure 5.9 Depth profiles of a Nb ₃ Sn coated sample sputtered at 1 kV and 5 kV, which demonstrates no difference in preferential sputtering between the two sputtering conditions.....	53
Figure B.1 XPS survey scan of single crystal region of niobium coated with Nb ₃ Sn.....	54
Figure B.2 High resolution scans of O, Sn, and Nb for Nb ₃ Sn coated polycrystalline coupon.....	55
Figure B.3 Anodized samples from left to right, Blank, 10V, 20V, 30V, 40V, and 50V.	56
Figure B.4 FIB cross section with measurements of 50V anodized layer.	57
Figure B.5 XPS depth profile of sample U49 anodized at 50V.....	57
Figure B.6 Depth profile of oxygen concentration for each of the anodized samples. A FIB cross section of the 50V was used to determine oxide thickness (depth) for each of the samples.....	58
Figure B.7 XPS survey scan (A) of niobium surface stopped early in the Nb ₃ Sn coating process. Figure 5.16B shows where Cl peaks would appear if Cl was present.	59
Figure B.8 (A) Image showing FIB cross section of 78 hr Nb ₃ Sn coating. The dashed lines LS-1, LS-2, and LS-3 represent the approximate locations of line-scans. Points P1 and P2 show the approximate location and spot size for the point analyses of Nb ₃ Sn and bulk niobium. (B) EBSD map of corresponding Nb ₃ Sn layer. EDS line scans are marked with dashed lines.....	60
Figure B.9 EDS spectrum from Nb ₃ Sn coating grown for 78 hrs. Analysis placement is shown in Figure 5.17A as “P1”.....	61
Figure B.10 Vertical line scans of Nb ₃ Sn coating. A slight decrease in tin concentration can be seen from the top to bottom of the Nb ₃ Sn layer. Positioning of line scans can be seen in Figure 5.17.....	62
Figure B.11 EDS line scan placed parallel to the surface, through the center of the Nb ₃ Sn coating. For placement of analysis see black dashed line in Figure 5.17B.	62
Figure B.12 Plot of EDS line scan LS-3 and XPS depth profile from the same niobium coupon coated with Nb ₃ Sn for 78 hrs.	63
Figure 6.1 Configuration of dual beam microscope equipped with EDS, EBSD, and FIB.	65
Figure 6.2 Schematic showing diffraction from crystal planes and indicating geometry involved in Bragg’s equation.....	66
Figure 6.3 Kikuchi pattern collected from bulk niobium after vibratory polishing.....	66
Figure 6.4 Magnified grain boundary from bulk niobium in Figure 2.2B, each pixel represents a 30 nm step.	68
Figure 6.5 Two examples of EBSD cross sections (approximately 85 μm in length). Figure 2.2A shows a nanopolished sample, while Figure 2.2B shows a cross section prepared by diffuse ion beam.....	69

Figure 6.6 Leica TIC 3x sample chamber with triple argon ion beams. Sample location is at beam convergence point.....	70
Figure 6.7 Sample mounting for Leica TIC 3x. A.) Cross-section view showing tungsten carbide (WC) mask with standard mounting. B.) Top down view of standard mounting, showing gaps due to rough Nb ₃ Sn surface. C.) Top down view of sandwich method for mounting.	71
Figure 6.8 (A) Cavity cut-out specimen mounted to SEM stub ready for FIB cross-sectioning and polish (B-D). Example orientation maps from FIB preparation of cavity cut-out specimens (E-F).	72
Figure 6.9 IPF of niobium bulk material (A) and the Nb ₃ Sn coating (B) derived from data in Figure 2.2B.	74
Figure 6.10 (A) Map showing Nb ₃ Sn coating on niobium with grain boundary misorientation information overlaid. (B) Legend for grain boundary rotation angles. (C) Data collected from ~250 grains located at the Nb/Nb ₃ Sn interface from multiple samples.	75
Figure 6.11 (A) SEM image of FIB cross sectioned patch defect. (B-C) Orientation maps of patch defects prepared by FIB.	75
Figure 6.12 SEM image (A) and corresponding orientation map (B) of Nb ₃ Sn surface area containing patches. Patches index as single crystal Nb ₃ Sn.....	76
Figure 6.13 EBSD orientation map collected from a sample that was anodized prior to Nb ₃ Sn coating. (1100 °C / 12 hr)	77
Figure 6.14 Histogram comparing grain size of Nb ₃ Sn coated samples with and without pre-anodization.	77
Figure 6.15 Histogram comparing the range of aspect ratio in Nb ₃ Sn coatings with and without pre-anodization.	78
Figure 6.16 Graphic showing relationship of Feret angle to physical geometry of Nb ₃ Sn grain. Where θ_F is the Feret angle and θ_G is the orientation angle of the grain with respect to the x-axis.....	78
Figure 6.17 Histogram showing the distribution of the Feret angle for coatings grown with and without pre-anodization.	79
Figure 6.18 Plot showing Feret angle as a function of grain size for coatings grown with and without pre-anodization.	80
Figure 6.19 Orientation mapping of niobium coated with Nb ₃ Sn. Map (A) was coated in a single step while map (B) was coated then re-coated. Samples were prepared by FIB. ..	81
Figure 6.20 Orientation maps A, B, and C, collected from samples 2, 4, and 6 as found in Table 3.1. Each map shows a 15 μm length of Nb ₃ Sn coating	82
Figure 6.21 Histograms A, B, and C are grain size distributions for samples 1, 2, and 6 as found in Table 3.1.	83

List of Tables

Table 5.1 Variables and calculated attenuation length (λ) values. Values for λ were calculated using Equation 5.1.	46
Table B.1 Composition values expressed in weight % and mole fraction calculated for coated polycrystalline niobium.....	56
Table 6.1 Coating steps for six overcoat samples tested. "1" represents one hour of coating, "1+1" represents one hour of coating plus an additional hour, etc.	81

Chapter 1

1 Introduction

1.1 Motivation and Significance

Particle accelerators are a critical tool for frontier science. The discovery of the Higgs at the Large Hadron Collider or the steady stream of results from synchrotron storage ring light sources are probably the most familiar examples. At the heart of modern high energy accelerators are superconducting radiofrequency resonating cavities, referred to as SRF cavities. First coming into large scale operation in 1994 with the construction of the CEBAF accelerator at Jefferson Lab, SRF technology broke down many historical performance barriers. Superconducting cavities allowed for continuous operation, where room temperature accelerators are generally limited to a 1% duty cycle. The resonant design allowed for relatively small amounts of RF energy to be introduced and amplified greatly, resulting in accelerating gradients of tens of millions of volts per meter. Modern SRF cavities are solid niobium and operate at a temperature of 2 °K, this includes the CEBAF machine and the second-generation LINAC Coherent Light Source (LCLS-II) under construction at Stanford. Figure 1.1 shows a current state of the art 9-cell SRF cavity destined for the LCLS-II.

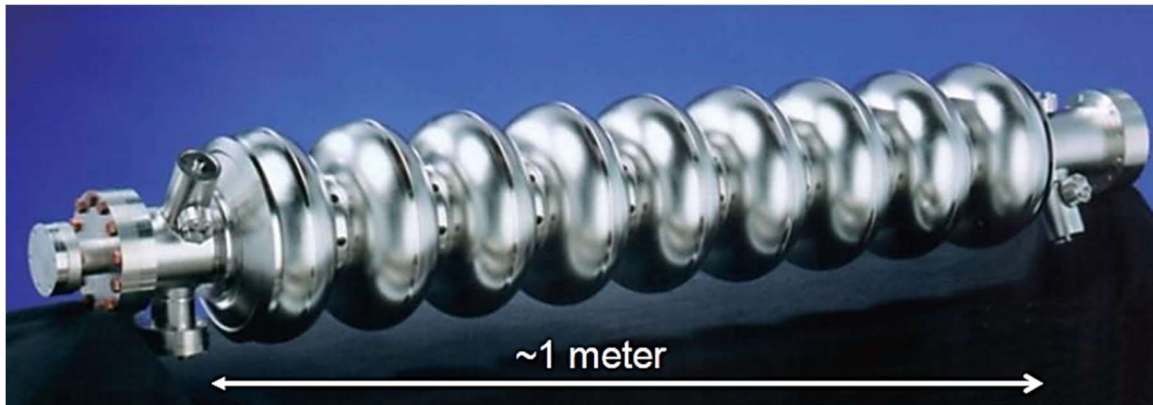


Figure 1.1 Image showing 9-cell SRF cavity design for the LCLS-II currently under construction at the SLAC National Accelerator Laboratory.

The going-forward issue with new accelerator construction is cryoplant construction and operational cost. Large cryoplants come with an electricity bill that numbers in the millions of dollars per year. This cost is so high because, while superconductors are free from resistance during DC current application, they exhibit a small amount of resistance at microwave frequencies. The situation is described in terms of the ratio of power stored in the fields inside the cavity to power deposited in the cavity walls. The power deposited in the walls of the cavity must be (expensively) removed by the cryosystem. The ratio of stored energy to power dissipated is called the quality factor (Q_0). The niobium on copper cavities of CERN's Large Hadron Collider perform with Q_0 values of 10^9 . In comparison, pure niobium cavities have Q_0 values of $\sim 10^{10}$. Next generation machines aim to perform

an order of magnitude better. Further, with today's SRF technology, Q_0 drops (Q-slope) as we push the gradient (the acceleration per unit cavity length E_{acc}) to ever higher values to reduce accelerator size. The performance of pure niobium technology continues to improve with better manufacturing practices, but is approaching limits set by the underlying physics.

Consequently, programs to attain higher Q_0 , especially at higher gradients, occupy much attention of accelerator science researchers. The two leading contenders are materials approaches; adding a small amount (few hundred ppm) of nitrogen to the cavity interior surface or providing it with a few microns thick layer of Nb_3Sn .

1.2 Research Objectives:

Accelerator science is a branch of applied physics. Historically research has proceeded by reasoning what should be better, building cavities, testing them, and varying parameters to optimize performance. As discussed at more length below, progress often comes as a result of a chance discovery; nitrogen doping is an example. Not surprisingly, progress has been slow and reverses have been encountered. Further, this approach has resulted in an incomplete picture of the fundamental mechanisms involved. Our group's approach, however, asserts that processing determines structure, which determines performance. The work described here takes advantage of the availability of materials of known SRF performance and works backward to determine what controls performance. The central theme of this work is to discover how to characterize SRF materials in a way that reveals what matters.

1.3 Structure of this Dissertation

The next chapter (Chapter 2) focuses on background, review, and description of the current understanding for nitrogen addition techniques. Chapter 3 covers the same information for Nb_3Sn cavity coating. The subsequent chapters (Chapters 4 to 6) discuss the development of methods and application of techniques specific to SRF cavity materials. Each chapter is specific to a technique (SIMS, XPS, and EBSD) and written as an independent paper. At the end of each chapter are appendices which contain additional experiments and material outside the intended scope of the paper. Chapter 7 concludes the work with a summary and recommendations moving forward.

Chapter 2

2 Background and Current State of Nitrogen addition

2.1 Paradigm Shift: (2013-2016)

Until 2013 the long-held belief was that elements such as H, C, O and N were contaminants in niobium SRF cavity material, to be avoided at high cost. Decades of research had concentrated on the deleterious effects and reduction of these unavoidable contaminants. [1] [2] [3] [4] [5] So entrenched was the belief that even when presented with data in 1973 showing increasing Q_0 with high levels of nitrogen, it was missed. [1] Then in 2013 nitrogen's role in SRF changed with the first published results from nitrogen doped cavities. [6]

There exist superconducting niobium nitrides (Figure 2.1) which can be formed on the surface of niobium using a process of thermally diffusing nitrogen. [7] [8] Superconducting niobium nitrides have the benefit of a higher superconducting transition temperature than pure niobium. FermiLab was exploring this process by heat treating cavities (800-1000 °C) in nitrogen gas at varying pressures (20-50 mTorr). Treated cavities showed very poor Q_0 values ranging from 10^7 - 10^8 at 2.0 °K. In order to return cavities to their base state, material was removed by electropolishing (EP). Unexpectedly, after the removal of the nitride layer the Q_0 values increased to as high as 7×10^{10} . [6] Even more perplexing, the Q-slope (decreasing Q with increase in accelerating gradient), which is typically seen, reversed. Cavities actually became more efficient at higher accelerating gradients up to 20 MV/m. [9] It should be noted, significant improvements in Q_0 were seen in cavities from Jefferson Lab during the same time period as a result of titanium contamination (Ti-Doping). [10] [11] Due to the ease of doping nitrogen as compared to titanium, N-doping has been the method of choice for both research and manufacture of cavities.

The timing of the discovery doping was quite fortuitous as planning for SLAC's LCLS-II was underway, with delivery of cavities to SLAC set for September of 2018. To fast track the development and implementation of the N-doping process for LCLS-II a joint R&D program was developed between Cornell, FermiLab and Jefferson Lab. [12] [13] [14] This collaborative effort was specifically for the purpose of establishing credibility and viability to N-doping, while providing a commercially viable protocol and performance expectations. [12] While the purpose of the collaboration was utilitarian in nature, it has produced a plethora of publications in a short amount of time, with at least a partial story of the effects and mechanism behind N-doping being elucidated. Here it makes sense to split the discussion of our knowledge on the subject into two sections, first we will discuss diffusion of nitrogen into niobium, followed by a discussion of possible mechanisms behind N-doping's impressive effect on cavity performance.

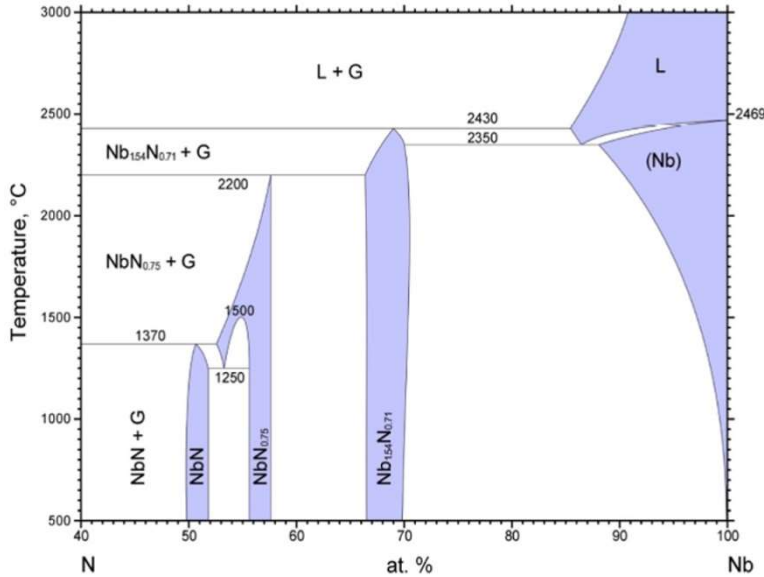


Figure 2.1 Phase diagram of the nitrogen/niobium system. [15]

2.2 The Diffusion of Nitrogen into Niobium

N-doping is really a three-part process, with the formation of nitride being first and ongoing, and then two separate simultaneous diffusion problems. Part one is the formation and growth of niobium nitride (NbN) at the surface. Skipping the formation of a nitride layer would be preferred, and should be possible judging by activation energies seen. (Figure 2.2) [16] However, within the range of temperatures used for N-doping, nitride formation is the thermodynamically preferred process. This has been experimentally verified by work partially completed as part of this dissertation. [17] A large portion (98%) of the nitrogen is used in the formation of nitride. While there are several nitrides that should be thermodynamically stable at temperatures currently used, only NbN is present. [16] This is serendipitous as some nitrides can precipitate out within grains and grain boundaries when cooled. In the case of Nb₂N any nitrogen above the saturation limit (1.06 at% for Nb₂N) will precipitate out in the form of a Widmanstatten structure. [18]

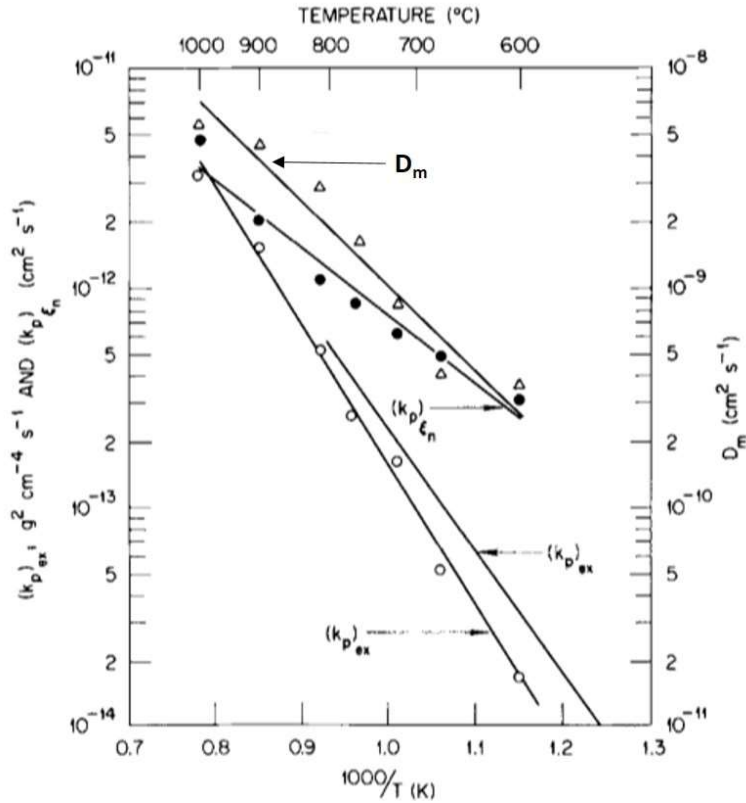


Figure 2.2 Arrhenius plot. Line marked D_m shows nitrogen in metal, while line marked $[k_p]_{eqn}$ represents nitride growth. The lower two lines represent the nitridation kinetics. [16]

Once NbN has formed on the surface, nitrogen diffuses from the gas through the surface nitride layer. This is the second part of the diffusion problem. The third part is the diffusion of nitrogen from the nitride layer into the bulk Nb. Each part can be treated as a separate problem since each boundary (gas/nitride/bulk) can be considered an infinite source. Hence the diffusion curve of interstitial nitrogen will follow a complimentary error function based on Fick's law for both diffusion into the nitride and into the bulk. [19] Figure 2.3 shows a profile of N through both the nitride and bulk niobium regions.

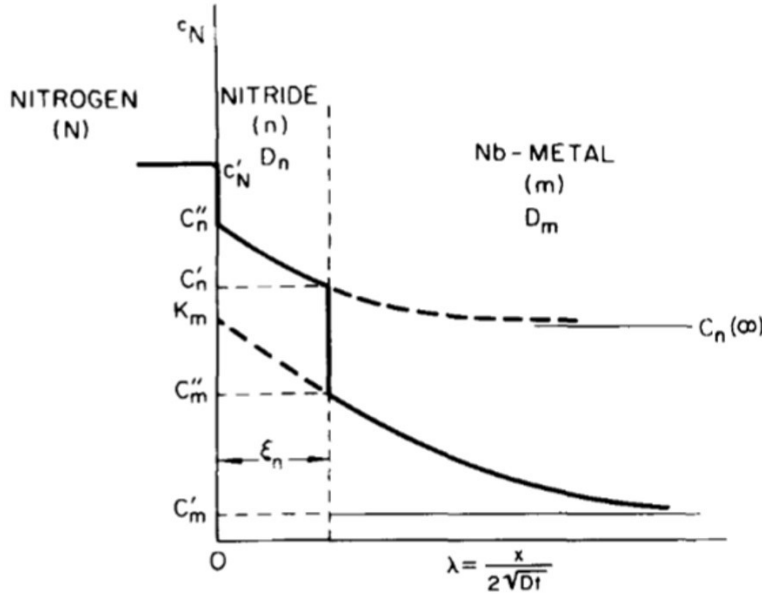


Figure 2.3 Diagram showing nitrogen diffusion profile in both nitride and bulk niobium. [16]

In this Figure, (N) is the nitrogen gas. (n) and (m) mark the nitride and niobium metal regions, where the nitrogen diffusion coefficients D_n and D_m rule accordingly. ξ_n is the nitride thickness. C'_m and C''_m are the initial and saturation concentration of nitrogen in niobium. K_m and $C_n(\infty)$ are the surface concentration and infinite concentration of nitrogen in niobium and nitride respectively. Neither of these are physically present, but are parameters in the error function and are calculated.

2.3 Mechanics Behind N-doping's Cavity Enhancement

Due to the accidental nature of N-doping's discovery and enormous positive impact on build and operation costs, the accelerator community was left in a less than optimal position in 2013. With the benefits of N-doping being so great the process was fast tracked for production with little to no understanding of the fundamental mechanics of how the process worked. As previously mentioned a joint R&D effort between Jefferson Lab, Cornell and FermiLab was formed. This effort was mostly geared towards process optimization for the production of SLAC's LCLS-II project for several years (~2013-2015). However, based on this work and a turn towards more fundamental studies from 2015-2018 at least a partial understanding of the mechanism behind Q_0 improvements, "anti-Q slope" and lower quench fields has taken shape.

The Q_0 for an SRF cavity is inversely proportional to the RF surface resistance of that cavity. The RF surface resistance (R_s) is made up of two components; one is the Bardeen-Cooper-Schrieffer (R_{BCS}) and the other is residual (R_{Res}). (Equation 2.1)

$$R_s(T) = R_{BCS}(T) + R_{Res}$$

Equation 2.1 [20]

The R_{BCS} contribution is temperature dependent and stems from the oscillation of electrons in the RF field. The R_{res} contribution is temperature independent and includes losses from oxides, hydrides and trapped magnetic flux. [21] [20] Surface treatments, such as N-doping, impact a cavity's performance by altering the surface resistance. [22] N-doped cavities (1.3 GHz, 2.0 K) can have R_S values lower than 5 n Ω , opposed to standard cavities where R_S is generally closer to 15 n Ω . [14] This lowering of R_S is attributed to a reduction of the mean free path (MFP). The MFP for N-doped samples has been found to be very low, \sim 8 nm, while typical (EP + 120 $^{\circ}$ C) samples have a MFP of \sim 30 nm. [23] The doped nitrogen "dirties" the RF conducting layer of the cavity, adding scattering centers, and importantly does not lower the critical temperature in the same way as other impurities, such as oxygen. [24]

The medium-field Q-slope (MFQS) is inherent to current cavity treatment and has been shown to be caused by an increase in R_{Res} and R_{BCS} as the RF magnetic field increases. [25] Figure 2.4 shows characteristic MFQS in the "typical" cavity data compared with N-doped cavities showing a reversal or "anti-Q-slope" behavior, increasing in efficiency (to a point) as the accelerating field increases. [6]

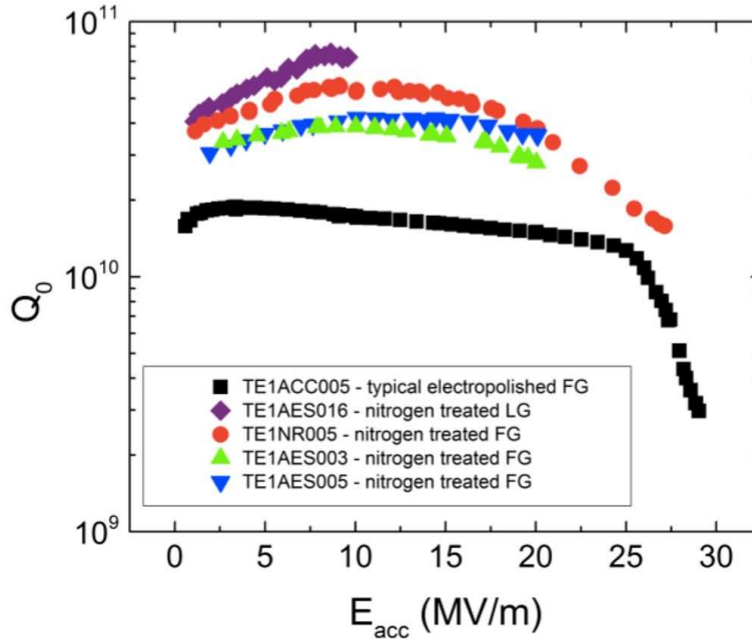


Figure 2.4 Shows comparison of quality factors as a function of the RF accelerating field for several N-doped cavities and a cavity prepared under normal/standard conditions. [6]

By making use of the differences in temperature dependence, the R_{BCS} and R_{Res} can be decoupled from R_S measurements. [25] [26] Figure 2.5 shows decoupled R_{BCS} and R_{Res} values for multiple cavity preparations as a function of field. [6] While there is good improvement in R_{Res} for the N-doped cavities the most striking difference is the drop in R_{BCS} with increasing field strength. As mentioned above it has been shown that there is a link between MFQS, R_{BCS} and R_{Res} . [25] It is clear from the data presented in Figure 2.5 that there is a link between the "anti-Q-slope" behavior of N-doped samples and the R_{BCS} . It also appears probable that there is a heavier dependence of Q-slope on R_{BCS} than R_{Res} .

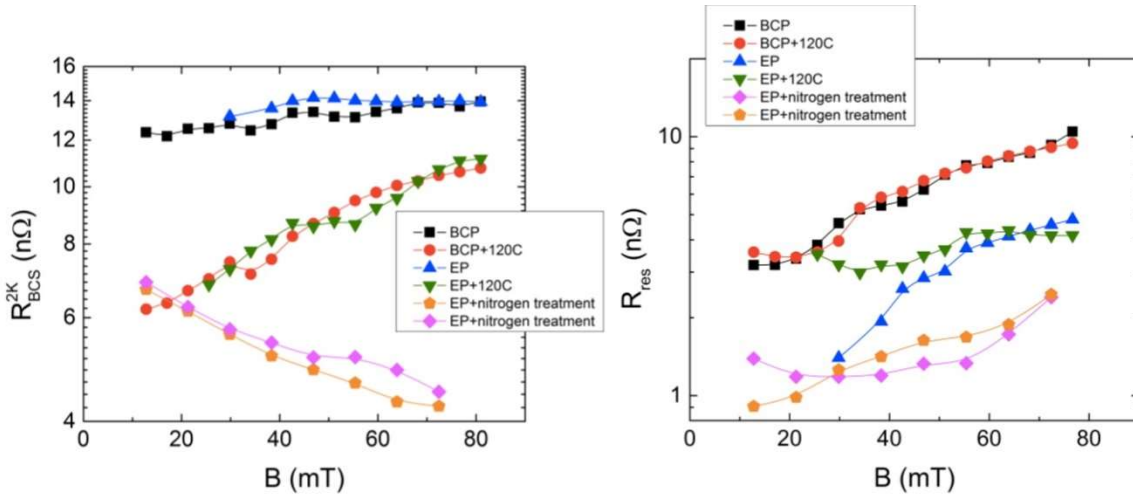


Figure 2.5 Decoupled R_{BCS} and R_{Res} values as a function of field strength for several different cavity preparations. [6]

When niobium enters the superconducting state it expels magnetic fields (Meissner effect). However, this expulsion of fields is not complete and some remain trapped in the material. This trapped flux is detrimental and in well-prepared cavities the main component of R_{Res} . [27] N-doped cavities with reduced MFP are more sensitive to trapped flux. The N-doped cavities R_{Res} losses are 3.6 times higher than 120 °C baked cavities for the same amount of trapped flux. Not only are N-doped cavities more sensitive to trapped flux, but also to applied magnetic fields, incurring 3 times more losses from R_{Res} than 120 °C cavities. Figure 2.6 demonstrates sensitivity increase for both trapped flux and applied magnetic field. [28] Due to this increased sensitivity to magnetic field and trapped flux, care will have to be taken in cool down and shielding. Cavities slowly cooled through the superconducting transition have shown a significant degradation of Q_0 . [12] This means in order to retain high Q_0 values for N-doped cavities; cavities must be cooled with large spatial gradients (fast) to help expel as much flux as possible and steps must be taken to limit the magnetic field (shielding). [29]

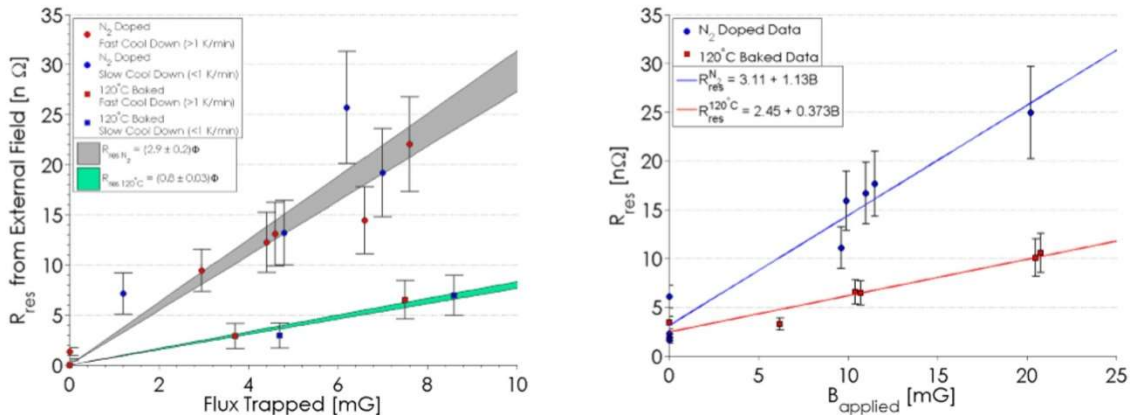


Figure 2.6 R_{Res} as a function of trapped flux and as a function of applied magnetic field. [28]

Figure 2.7 shows data from several different preparations for cavities. The slopes of these lines (Equation 2.2) can be defined as a magnetic flux sensitivity value. [30] The sensitivity

values can then be plotted (Figure 2.8) as a function of MFP and a Gaussian distribution is seen.

$$Sensitivity = \frac{dR_{Res}}{dB_{Trapped}}$$

Equation 2.2 [31]

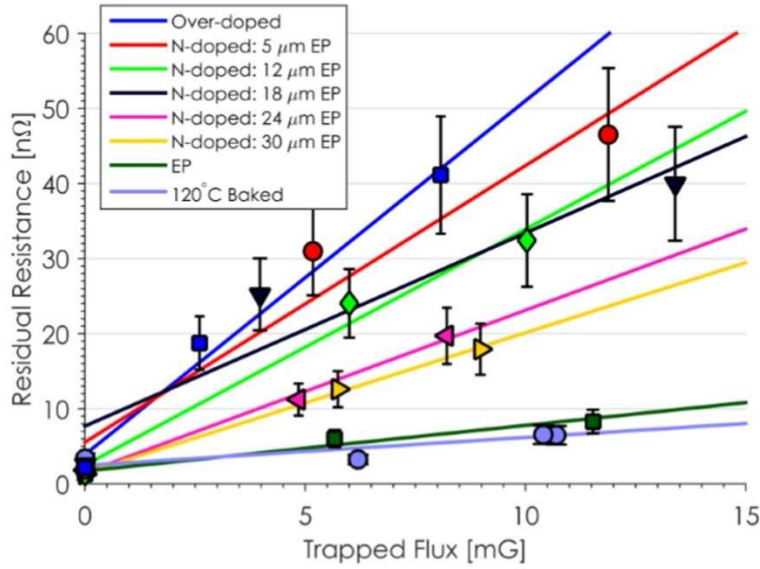


Figure 2.7 R_{Res} as a function of trapped flux for different cavity preparations. Taking the slope provides magnetic flux sensitivity. [30]

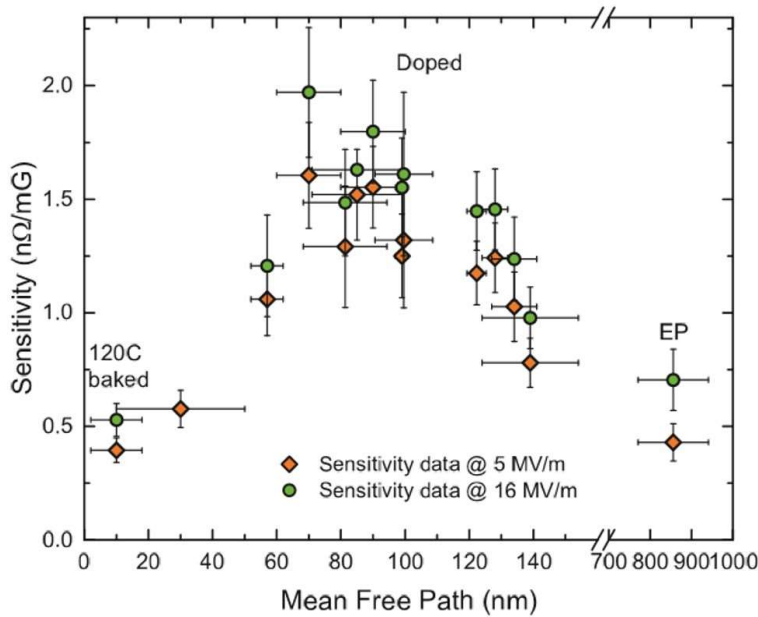


Figure 2.8 Sensitivity to trapped flux as a function of MFP. [31]

The Gaussian distribution shows a maximum sensitivity to trapped flux, which means that cavities with high amounts of N-doping can have very low sensitivity to trapped flux. However, over doped cavities dramatically lower the quench fields of the cavities. [32]

This can be seen in Figure 2.9, which shows an over doped cavity where Q_0 has been measured as a function of E_{acc} . Successive amounts of material have been removed via EP, effectively raising the MFP and subsequently the quench field.

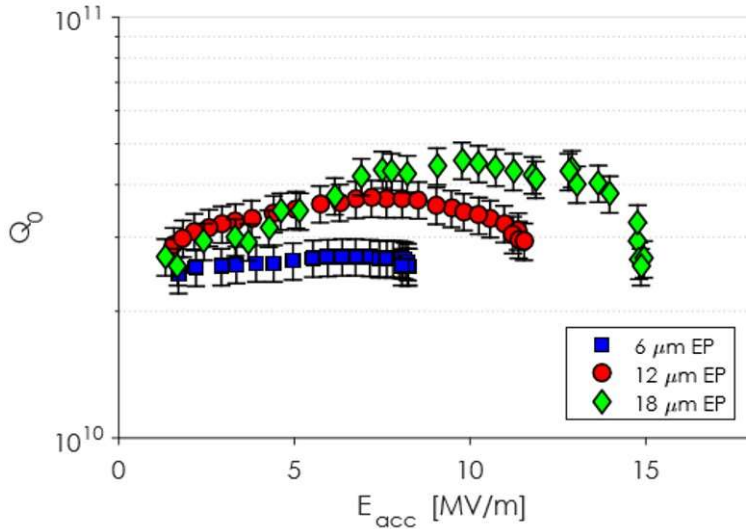


Figure 2.9 Performance of over doped cavity with differing amounts of material removal. [32]

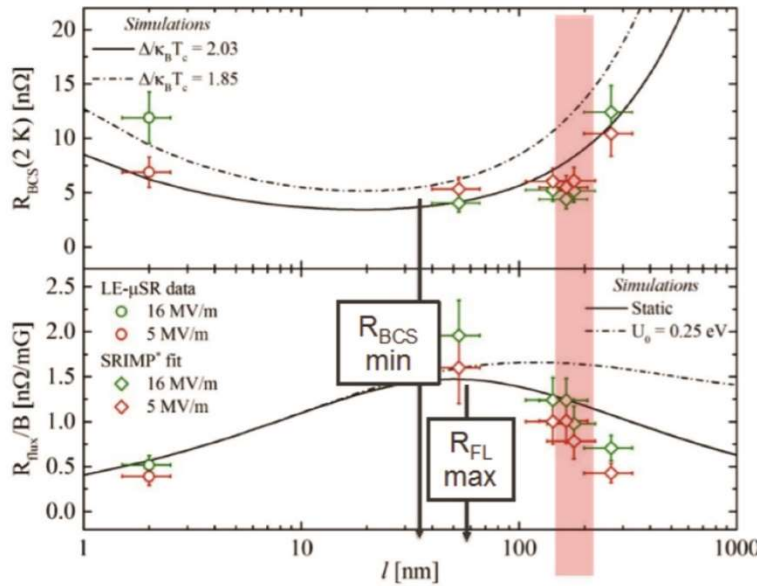


Figure 2.10 R_{BCS} and trapped flux induced resistance as a function of MFP for cavities doped and un-doped. Red shading shows approximate results for 2/6 doping recipe. [33]

This all points to an optimal amount of N-doping, where the doping level is as low as possible to minimize sensitivity to trapped flux, but still reap benefits of high Q_0 values with an “anti- Q slope”. In other words; maximize quench field, minimize trapped flux losses, and maintain minimum R_{BCS} . Before most of these analyses were complete, a “so far optimal” doping recipe was found through brute force trial and error as part of the joint effort between FermiLab, Jefferson Lab and Cornell to establish a protocol for the LCLS-II project. [33] The current (LCLS-II) optimal recipe for N-doping is referred to as “2/6”, which refers to 2 minutes of nitrogen injection and 6 minutes of anneal at 800 °C, followed

by $5\mu\text{m}$ of EP surface removal. [33] However, there is quite a large range of MFP (Figure 2.10) that corresponds to the minimum R_{BCS} resistance of $\sim 4.5\text{ n}\Omega$ and it has yet to be fully explored. Therefore, the optimal doping recipe is still under investigation.

2.4 Low Temperature Doping

As mentioned in previously, it would be of much benefit to be able to N-dope niobium without the formation of the nitride surface. This would remove the need for the laborious surface treatments post doping in order to remove the nitride. Recently this appears to have been accomplished through a process known as “Nitrogen Infusion”. [34] N-infusion involves exposing niobium to nitrogen at low temperatures (120-160 °C) and long times (48 hrs) relative to standard N-doping procedures. Quality factors for N-infusion appear comparable to that of N-doping at $\sim 5 \times 10^{10}$. [34] N-infused cavities do not appear to quench as early as doped cavities, in some cases reaching accelerating gradients of 30-35 MV/m before showing a large negative slope or quench. Figure 2.11 shows Q_0 results for cavities N-infused under a variety of conditions. SIMS and TEM results were reported, but both were qualitative in nature. There was no quantitation of either depth or concentration for SIMS. Precipitates were seen in TEM images, which look similar to niobium nitrides, but are conjectured to be niobium carbides.

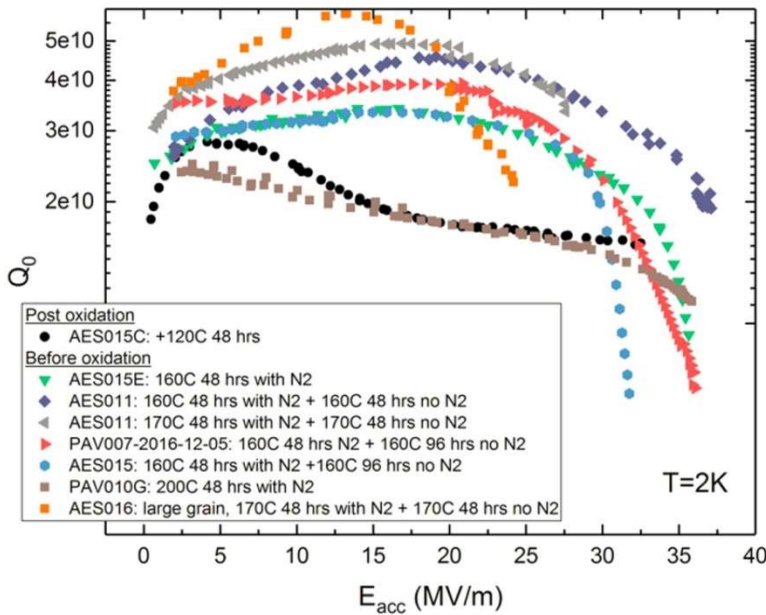


Figure 2.11 Comparison of Q_0 curves for different heat treatments in the range 160-200 °C, referenced to standard 120 °C bake post oxidation. [34]

Chapter 3

3 Background and Current State of Nb₃Sn Cavity Coating

3.1 The 4.2 K Goal

Superconducting radio frequency (SRF) technology continues to grow as the choice for high-end machines because of cost and performance advantages over warm copper. Nonetheless, the initial cryoplant and ongoing electric power costs of the presently-required 2 °K operation are a significant burden for today's niobium cavity machines. Operation at 4.2 °K instead would be a major benefit, cutting the size/cost of cryoplant needed and cutting operating costs by a third. [35]

More than 40 years ago, accelerator science researchers exploring alternatives to pure niobium settled on Nb₃Sn as the most promising alternative. [36] Their preferred embodiment was a few-micron thick layer formed by diffusion coating. Extensive R&D programs at Siemens and at the University of Wuppertal thru the 1980's sought to achieve a readily deployable Nb₃Sn SRF cavity technology. Despite concerted efforts to the contrary, the best and typical cavity performance featured quality factors in the mid 10¹⁰ to low 10¹¹ range at few MeV/m gradients, which fell sharply with increasing gradient. [37] [38] Meanwhile, the performance of pure niobium cavities continued to improve, leaving no place for Nb₃Sn as attained. The decrease of quality factor with increasing gradient was duplicated and became known as the "Wuppertal slope". While the cause was never clearly identified, the consensus view was that the slope was something inherent to Nb₃Sn and research faded due to competing interests. Recently, however, performance results obtained by researchers at Cornell were essentially free of the slope, achieving gradients in excess of 10 MeV/m with diffusion-coated cavities. [39]

With Cornell's results the prospect of success has re-emerged. Further, during the years since Wuppertal, the needs of microelectronics technology have driven development of an arsenal of powerful materials characterization tools that can wrest new insights from systems like Nb₃Sn diffusion coatings. Accordingly, Jefferson Lab and its university partners have been motivated to undertake a research program aimed at diffusion coating Nb₃Sn. A diffusion coating facility, described in detail in [40], was constructed to provide materials for research and coated cavities for performance studies. A goal for the present research is to explore what modern characterization tools might reveal about Nb₃Sn diffusion coatings, choosing the most effective for extensive investigation in the next phase of coating and process parameters, as related to coated cavity performance.

Chapter 4

4 Secondary Ion Mass Spectrometry for Superconducting Radiofrequency Cavity Materials

Historically, many advances in superconducting radio frequency (SRF) cavities destined for use in advanced particle accelerators have come empirically, through the iterative procedure of modifying processing and then performance testing. However, material structure is directly responsible for performance. Understanding the link between processing, structure, and performance will streamline and accelerate the research process. In order to connect processing, structure, and performance, accurate and robust materials characterization methods are needed. Here one such method, SIMS, is discussed with focus on analysis of SRF materials. In addition, several examples are presented, showing how SIMS is being used to further our understanding of materials based SRF technologies.

4.1 Introduction

4.1.1 Motivation for Work with SRF Materials

Superconducting radio frequency particle accelerators are invaluable tools in the push to expand the frontier of scientific understanding. In order to push further, accelerators with higher particle energies, increased beam current, and reduced cost per unit performance must be constructed. Accelerator performance is chiefly controlled by the superconducting niobium cavities at their heart, most especially by the ~ 40 nm rf-active surface layer at the cavity interior. Present technology pays much attention to niobium purity, measured by residual resistance ratio (RRR), and governed by bulk composition specification in the ppm range for interstitial elements (C, N, O). How this translates to composition of the active layer and in turn into performance is not known, as the composition of the active layer is not measured.

Until recently (~ 2013) it was believed elements such as H, C, O and N were contaminants in SRF niobium to be avoided at high cost. [1] [2] [3] [4] [5] However, extensive evidence from cavity processing and testing indicates that introduction of small amounts of nitrogen and perhaps other interstitials can markedly improve energy efficiency, as characterized by quality factor Q_0 . [41] [34] [6] [42] [43] Difficulties encountered in current efforts to implement doping technology for the Linac Coherent Light Source II (LCLS II) suggest that deeper understanding is needed. [44] [45]

Another potential path to improvement is the creation of a micron-thick layer of Nb_3Sn on the cavity interior surface. [39] The viable operating temperature for many applications moves from 2 °K (superfluid helium) to 4.2 °K (liquid helium), with great savings in cryogenics expense and complication. Further, the maximum theoretical surface magnetic field (which scales with accelerating gradient) is approximately doubled. [46] [39] However, the quality factor for current coated cavities typically falls with increasing gradient so significantly that the technology has not been usefully implemented in

accelerators. It is not clear why this occurs nor why, in a few instances, it has not occurred. [47]

A common thread for these and other issues is the need for better understanding of how composition and processing affect the active layer and how that in turn affects performance. A major aspect is composition measurements down to a few tens of ppm at a dimensional scale down to a few nm. Only Secondary Ion Mass Spectrometry (SIMS) has this capability.

4.1.2 Secondary Ion Mass Spectrometry

SIMS originated in the 1970's and has since found wide use in both industrial and research institutions. This is in large part because, of all analytical techniques, SIMS has excellent detection limits, down to 1 ppb in ideal conditions, and the ability to detect all elements.

Since the 70's the general principles of operation have remained the same. A primary ion beam is focused by a series of electrostatic lenses and used to bombard the sample surface of interest. This primary ion beam may consist of many types of ions depending on the goals of analysis. The most common are oxygen ions ($^{16}\text{O}_2^+$, $^{16}\text{O}^-$) or cesium ($^{133}\text{Cs}^+$). The primary beam bombards the sample at a high enough energy to cause the ejection of sample material. A small amount of this material is ejected as ions, and extracted as a secondary ion beam. The mass distribution and intensity of the ejected (secondary) ions can then be measured, from which is inferred the composition of the source. The relationship may be stated as:

$$I_{sec} = I_{prim} Y_{x,sec} D_{sec} C_x$$

$$Y_{x,sec} = Y_{tot} \alpha_x$$

Where I_{sec} is the measured ion intensity (counts/sec) of ions for the particular secondary ion, I_{prim} represents primary ion beam condition, energy and current, as sputter yield is dependent upon both. $Y_{x,sec}$, D_{sec} , and C_x are respectively the secondary ion yield of species x, instrument sensitivity for the particular species under the chosen conditions, and the concentration of the species of interest in the sample. $Y_{x,sec}$ is the product of the total sputter yield, Y_{tot} (sputtered atoms per bombarding ion) and the ionization probability of species x, α_x .

When considering I_{prim} , conditions are chosen in order to maximize I_{sec} while still meeting target spatial resolution and detection limits. This harmonizing of I_{sec} and I_{prim} must consider various trade-offs. For example, simplified greatly, SIMS operates by sputtering material from the sample surface and enough must be sputtered that adequate counts are accumulated in the particular species' peak to provide the measurement. Measuring a specific dopant level requires accumulating a certain number of counts over background at the peak position of the particular ion by sputtering a corresponding amount of material. So, sputtering a larger area provides greater sensitivity at a shallower depth: lateral resolution trades off against depth resolution. Hence, SIMS instruments cannot be optimized simultaneously for spatial resolution and sensitivity. [48] Lateral resolutions can vary from ~50 nm, making it possible to image grain boundary segregation, to hundreds of microns when trace quantification is needed. [49] [50]

For bulk nitrogen measurements in raw materials or N-doped witness coupons, the highest priority for a SIMS analysis method is detection limit and proper quantification. However, with the RF penetration depth controlling cavity performance, measuring nitrogen concentration near the surface (≤ 40 nm) with relatively high depth resolution is of concern. TOF-SIMS instruments are particularly good at high depth resolution and shallow analysis, with depth resolution less than 1 nm in ideal cases. [51] However, dynamic SIMS is capable of better detection limits and sufficient depth resolution. With the need to analyze near surface N, depth resolution must be determined under conditions that provide a sufficient sensitivity.

For an interface, depth resolution can be given as the change in depth between 84% and 16% of the maximum signal. [52] [53] In order to measure depth resolution, an interface was created by sputter coating a N-doped, electropolished (EP) witness sample with ~ 15 nm of platinum and palladium (80/20 by weight). This created an interface in the resulting depth profile (Figure 4.1) which could then be used to calculate the depth resolution. The depth resolution was calculated using the leading and trailing edge of the interface and found to be 6.0 and 6.4 nm respectively. Figure 4.1 shows a depth profile of the Pt/Pd coated sample with the physical location of the interface marked by the dashed line.

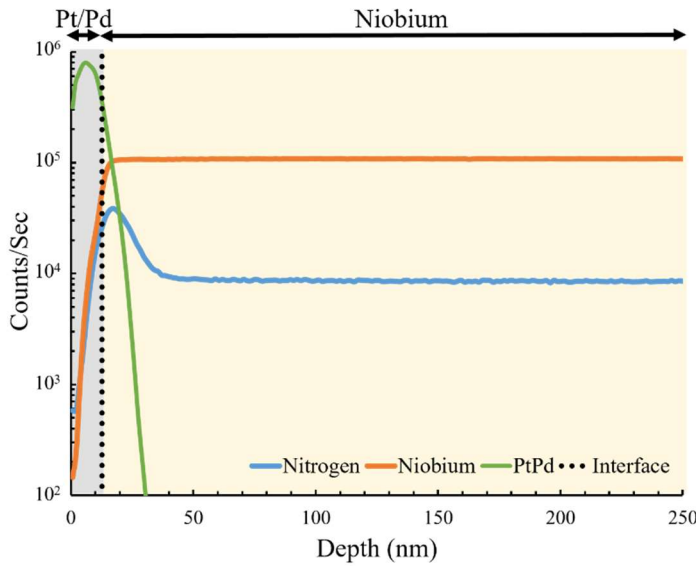


Figure 4.1 Depth profile of N-doped niobium with EP surface. Specimen was sputter coated with Pt/Pd prior to depth profiling.

There are multiple sample-dependent factors which affect the secondary sputter yield (Y_{tot}). Differing grain orientation is one which can cause sputter rates to vary greatly and negatively affect reproducibility and depth resolution. For example, while both implants in Figure 4.2 were created and analyzed under the same conditions, the single crystal depth profile shows a sharper implant peak and quicker drop to detection limit, indicative of better depth resolution. Depth resolution was estimated using roughness measurements and TRIM calculations and found to improve from ~ 109 nm for the polycrystalline implant to ~ 12 nm for the single crystal implant. [54]

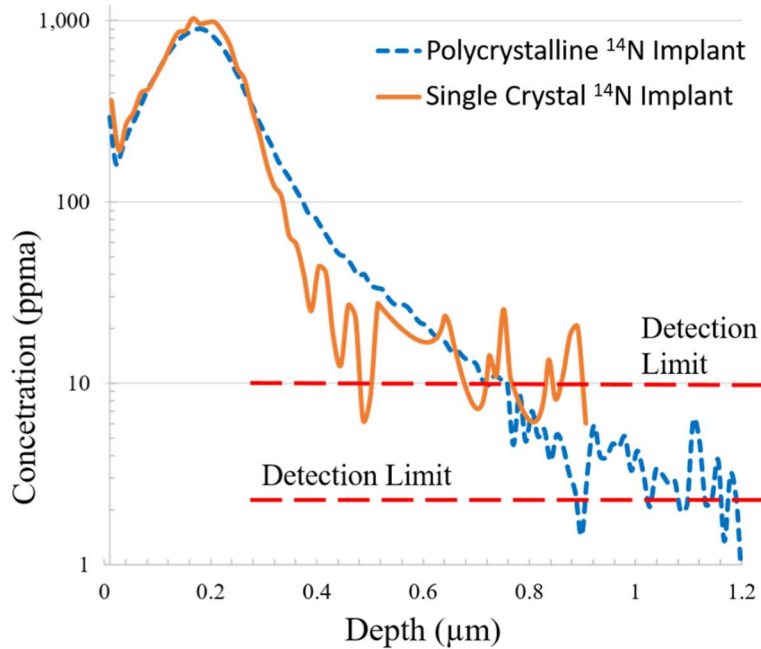


Figure 4.2 Depth profile of nitrogen implants used to calibrate nitrogen for both polycrystalline and single crystal material.

Surface topography will also negatively affect depth resolution and repeatability. [52] As a crater is sputtered, the original surface topography carries down and may increase with time. Normal niobium BCP surface finishes are insufficiently smooth and exhibit poor depth resolution and repeatability. Figure 4.3A shows multiple analyses from a single N-doped sample with BCP surface finish. The highest nitrogen concentration samples have high surface nitrogen which is not shown because the bulk concentration is of primary interest. In contrast to BCP samples, nanopolished (NP) samples have been found to reduce surface roughness to only a few nanometers and exhibit excellent repeatability in nitrogen measurements. [55] Figure 4.3B shows multiple analyses from two NP samples, higher concentration (orange) and lower concentration (blue), which were doped under different conditions. The difference in doping result can be clearly seen using NP samples. However, the error in the single BCP sample was larger than the difference seen, meaning the resulting differences in N concentration could not have been distinguished using normal BCP witness samples.

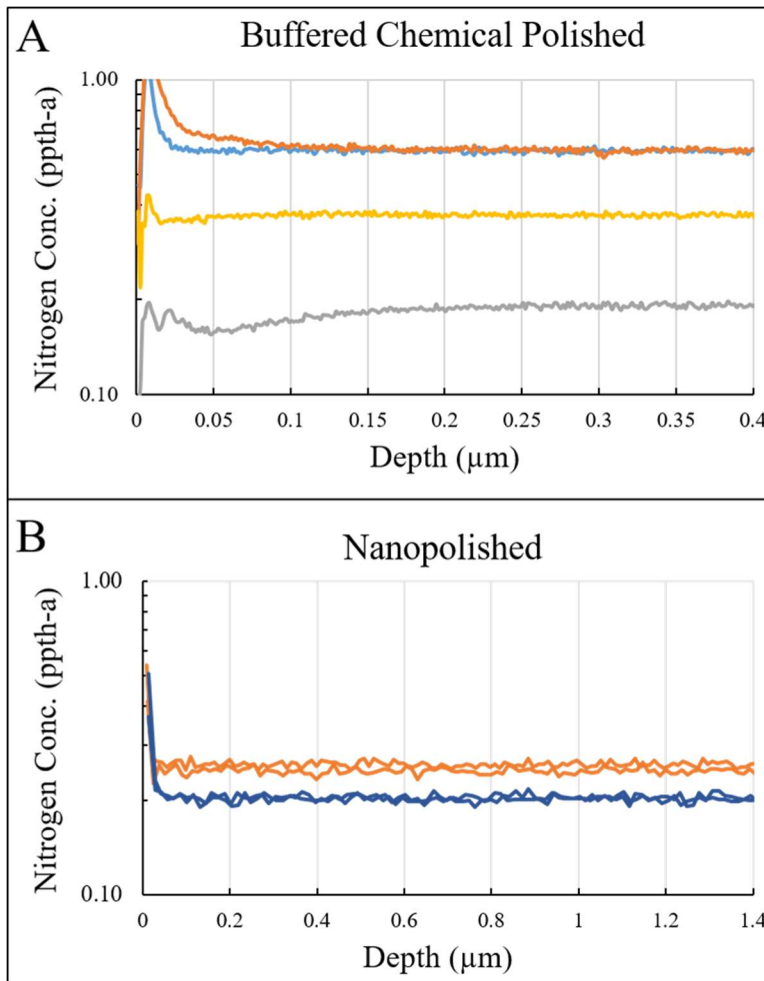


Figure 4.3 A and B show depth profiles with measured nitrogen concentration (parts per thousand atomic) from N-doped BCP and NP samples.

SIMS can be used to analyze species over many orders of magnitude from 100% to a lower detection limit on the order of 1 ppb. For low concentration analysis it is imperative to have low background signal from the species of interest in the instrument. This requires special attention when the species of interest are atmospheric such as oxygen and nitrogen. Oxygen and nitrogen are a large component of the surrounding environment and can be difficult to eliminate from a high vacuum environment. For experiments in which nitrogen and oxygen were of interest, analyses of samples were not started until an instrument vacuum of $\sim 3 \times 10^{-10}$ Torr was achieved. In addition, a cold probe surrounding the sample and cooled via liquid nitrogen was used to condense any gas directly surrounding the sample in vacuum.

Analysis of elements at low concentration requires ensuring the detection limit of the method and instrumentation is acceptable; i.e., lower than the subject species concentration. Implant standards can be used to determine detection limits for a given analysis at the existing vacuum and instrument condition. The detection limit at time of analysis is marked on Figure 4.2. The vacuum condition of the instrument was slightly worse during the single crystal analysis shown here and a significant loss in detection limit is observed.

Because atmospheric species, such as nitrogen and oxygen, are ever present in some amount, it can be difficult to know whether a baseline value for a sample is due to the species of interest within the sample or simply background instrument contamination. One way to empirically determine the nature of a detected signal is by conducting a raster reduction test. First a matrix level signal and impurity species of interest are collected at a larger raster. The raster is then collapsed while keeping the beam current and analysis area constant; 100 nA and 63 μm diameter area were used for the example here. If the raster is collapsed from $250 \times 250 \mu\text{m}^2$ to $150 \times 150 \mu\text{m}^2$, as was the case in Figure 4.4, this will cause the matrix signal to increase by a factor relative to the change in raster size. In the case of our example, it will increase by a factor of approximately three. If the species of interest increases this same amount, then the detected signal originates from the sample, with little background input. If the species of interest increases, but less than the matrix level signal, then there is some impurity detected from the sample, but it is near the detection limit. If the signal does not change, then no impurity species (only background signal) was detected, and the detection limit is at least a factor of three better than before raster collapse.

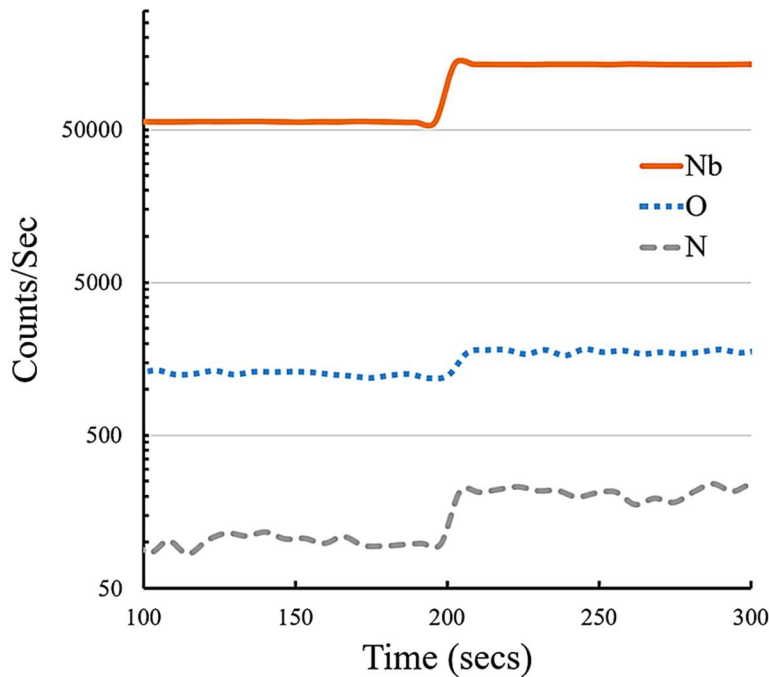


Figure 4.4 Raster reduction to check source of the ions detected for nitrogen and oxygen.

The “as received” materials, discussed later, have relatively low concentrations of both nitrogen and oxygen, making it necessary to check the origin of the species. A raster reduction was done each day that “as-received” samples were analyzed. In Figure 4.4 we can see the raster reduction from an analysis day where the nitrogen detected is still well above the baseline for the method/instrument, proving the nitrogen signal measured is from the sample. The oxygen signal however appears to be approaching the detection limit and has some contribution from outside the sample.

While it is useful to discuss concentration measurements in terms of the factors above to gain insight into SIMS, accurate quantification is non-trivial, requiring standards and SIMS

experiments as opposed to straight forward analysis common to other analytical techniques. This is due in large part to “matrix effects”. Secondary ion yields can vary five or six orders of magnitude across the periodic table and also several orders of magnitude depending on the bulk material (matrix). For an element of interest, a species is chosen which maximizes $Y_{x,sec}$. The ion yield for nitrogen is virtually zero under many analysis conditions, requiring detection of molecular species ($^{93}\text{Nb}^{14}\text{N}^-$ used here) to quantify nitrogen concentration. [53] Due to variation in $Y_{x,sec}$, quantification cannot be based on relative signal intensities only.

The most common method for quantifying SIMS depth profiles is by utilizing ion implant standards. An implant standard must be created for each species of interest by implanting it into the matrix of interest, preferably near the same concentration range. Its depth profile can then be acquired and the ion implantation dose can be used to calculate a relative sensitivity factor (RSF) for that species in that matrix. A reference signal from the matrix (here, Nb) is used to adjust for instrumental factors. Example analyses of nitrogen implants in both poly and single crystalline material appear in Figure 4.2. RSF values, which are inversely proportional to the secondary ion yield, can then be used to convert secondary ion intensity to concentration using:

$$\rho_i = \left(\frac{I_i}{I_m} \right) (RSF)$$

Where ρ_i is the impurity concentration in atoms/cm³, I_i is the measured impurity ion intensity, and I_m is the measured matrix ion intensity. Most concentrations are reported in atomic ppm and denoted by ppm(a).

In order to accurately quantify data using an RSF value, the intensity of the matrix signal, in this case niobium, must stay relatively consistent from sample to sample. This is because the RSF value is calculated by normalizing the secondary ion signal to the matrix (Nb) signal. Early on in the development of a SIMS method it became clear the matrix signal was varying from implant standard to sample, and from sample to sample in some cases. Examination of mass spectra from a number of samples showed a number of samples had interferences caused by ions with fractional masses believed to be metastable hydrides. Figure 4.5 shows the mass spectra from two samples. The blue line shows a sample free of metastables with a niobium peak clearly resolved to baseline followed by several niobium hydride peaks also resolved to baseline. The orange line in Figure 4.5 shows the mass spectrum of a sample in which there is a large amount of metastable interference and the niobium hydride peaks are seen to be much larger. This phenomenon was also observed by Maheshwari [56] and Stevie [11] and is discussed in more detail there. It was shown by heat processing samples the metastable contribution to the secondary ion signal could be eliminated. The vacuum heat treatment now common for niobium cavities (800°C) lowers hydrogen levels in the niobium enough to avoid the formation of metastable hydrides.

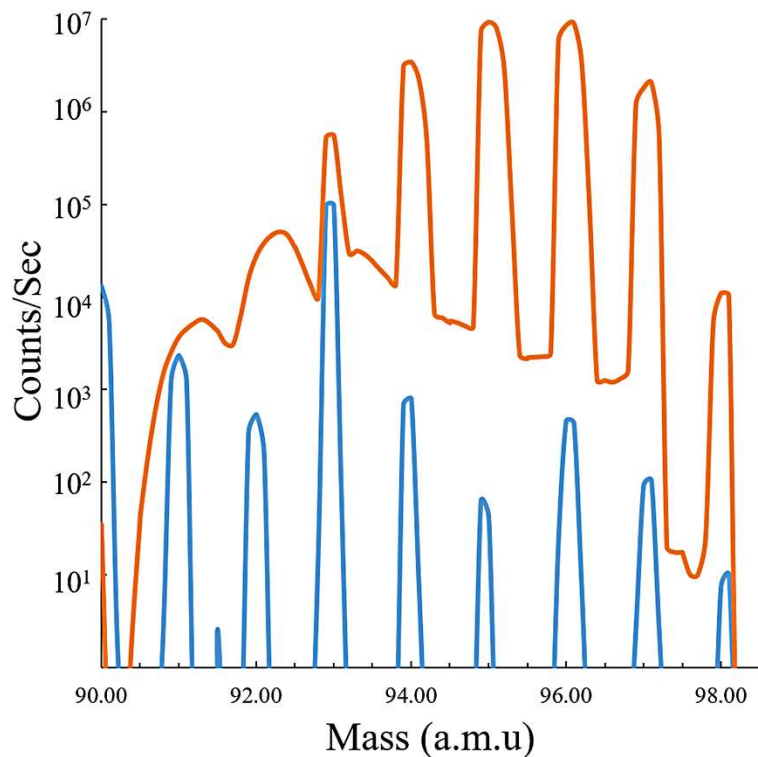


Figure 4.5 Mass spectra, one showing a sample with clearly resolved peaks (blue) and one suffering from metastable hydride interference (orange).

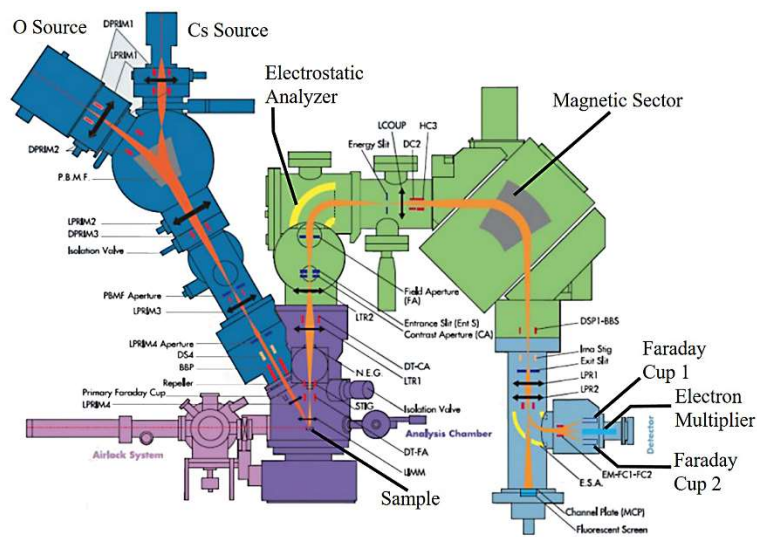


Figure 4.6 Schematic of Cameca IMS7f-GEO. Reprinted with permission from CAMECA®.

4.2 Experimental

4.2.1 Secondary Ion Mass Spectrometry

One of the main differences among variations of SIMS instruments is the mass analyzer type. There are three that are common: quadrupole, magnetic-sector, and time of flight.

Double focusing magnetic sector instruments are typically large and the most expensive. However, they have the ability to operate with high primary currents and have the highest sensitivity. This makes the dual focused magnetic sector instrument, such as the CAMECA IMS-7f GEO used here, the preferred choice for depth profiles and quantitative analyses of trace elements. Figure 4.6 shows a schematic of the CAMECA 7f instrument.

For nitrogen analysis, a Cs^+ primary ion beam was used with negative secondary ions being detected. The species $^{93}\text{Nb}^-$ was used as a reference signal in all cases. Nitrogen ion yield is low for many analysis conditions and virtually zero for negative secondary ions Cs^+ primary with detection of the molecular species ($^{93}\text{Nb}^{14}\text{N}^-$) shows the highest ion yield and was used for detection of nitrogen. Impact energy of 15 kV (10kV source/-5kV sample) was used with a current of 100 nA rastered over a $150 \times 150 \mu\text{m}^2$ area. A $63 \mu\text{m}$ diameter analysis area was used for typical depth profile measurements in order to avoid crater edge effects.

When small spot analysis was needed, the Cs primary beam was reduced to 5 nA with a size of $\sim 5 \mu\text{m}$. The smaller beam was rastered over a $10 \times 10 \mu\text{m}^2$ area. Due to the size of the beam in relation to the raster size, this gives an analysis spot size of $\sim 15 \mu\text{m}$, allowing analysis of single grains.

For analyses requiring higher depth resolution, such as low temperature addition samples, impact energy was lowered to 8 kV (+5 kV/-3 kV). While this maintained approximately the same angle of incidence as the 15 kV beam, 23.7° vs 24.4° respectively, the lower accelerating voltage lowered damage depth sufficiently to show a marked improvement in depth resolution. TRIM calculations show the majority of damage for the 15 kV condition to be $\leq 5.7 \text{ nm}$, while 8 kV is calculated as $\leq 4.0 \text{ nm}$. [54] Empirically, using the interface method described above, the depth resolution improved $\sim 10\%$ from 6.2 nm to 5.6 nm. In addition to the lower impact energy positively affecting depth resolution due to physical effects, the lower sputter rate increases the data density making for a more accurate representation of the near surface region.

4.2.2 Sample Holder

As mentioned, when analyzing for atmospherics at low concentration, good vacuum condition is paramount for low detection limits. A special sample holder for the CAMECA 7f was designed and machined in order to analyze as many samples as possible at one time, thus reducing instrument exposure to atmosphere and normalizing the instrument conditions for up to twelve $6 \times 6 \text{ mm}^2$ sample coupons at one time.

4.2.3 Samples and Treatments

Unless otherwise noted, witness samples were 10 mm square coupons cut by electrical discharge machining from trimmings of the 3 mm thick niobium sheet used to make SRF cavities (“RRR grade”). Typical grain size for polycrystalline material is in the $50 \mu\text{m}$ to $100 \mu\text{m}$ range in the un-annealed state, except for a few instances (as noted) of single or bi-crystals cut from large-grained ingot slices. When necessary to analyze a large number of samples at once, $10 \times 10 \text{ mm}^2$ coupons were trimmed via a diamond blade mounted to an Isomet Low Speed Precision Cutter in order to fit the 6 mm holder previously discussed.

Coupons were prepared with differing surface conditions including: buffered chemical polishing (BCP), electropolishing (EP), and nanopolishing (NP).

Standards used for quantification were prepared by ion implantation with ^{14}N to a dose of 1×10^{15} atoms/cm 2 at 160 keV and ^{16}O to a dose of 2×10^{15} atoms/cm 2 at 180 keV. Implants were prepared with a 7° target tilt. Treatments of standards, such as surface polish were matched as close as possible to that of the analyzed sample.

4.3 Results and Discussion

Provided here are several examples and brief discussion of SIMS utilized to gain insight into SRF materials.

A lamentable side effect of the typical N-doping recipes (here, 800 °C, 20 mins, 25 mTorr N) is the formation of non-superconducting nitrides on the surface that can extend 3-4 microns in depth. Figure 4.7 A and B show examples of nitride formation after nitrogen doping at 900 °C. This nitride layer must be removed, involving electropolishing (5 μm). It would be beneficial, in regards to logistics and cost, to develop an alternate doping recipe which avoids nitride formation. While there are historical works dealing with nitridation kinetics in niobium, some even dealing directly with SRF cavities, those studies take place at higher temperatures and pressures over relatively short “doping” times, making them not directly applicable. [1] [16] [3]

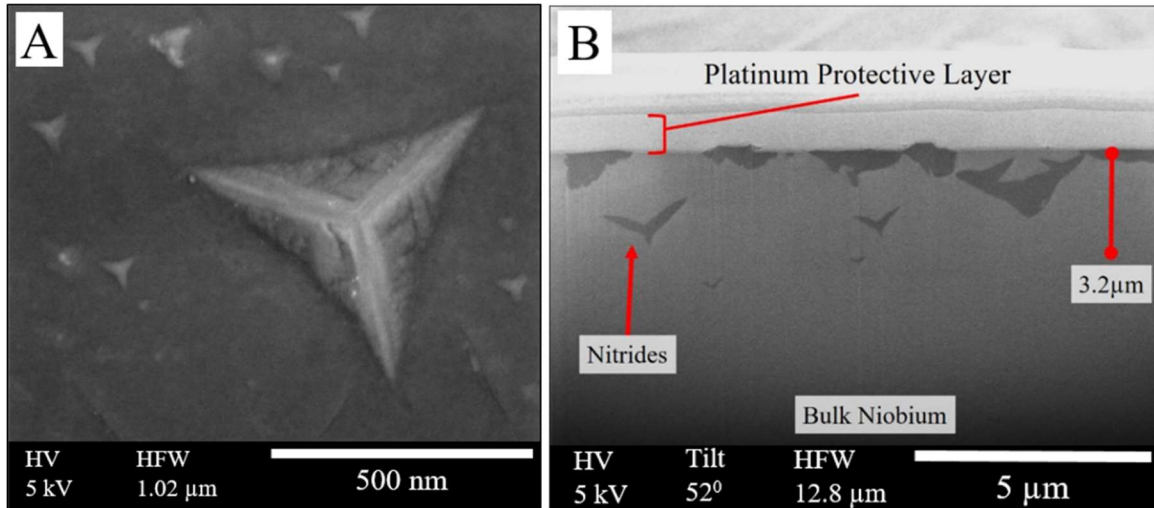


Figure 4.7 (A) Example of nitrides forming on surface of N-doped sample. (B) Shows a cross-section of a sample N-doped at 900 °C for 10 minutes at ~25 mTorr.

4.3.1 High Doping Temperature

In order to investigate the possibility of nitride free doping on similar time scales as currently used, a set of NP samples were prepared varying the doping temperature from 400°C to 900°C. All samples were doped for 20 mins at ~25 mTorr nitrogen, except for 900°C, which was doped for 10 mins at the same pressure. The samples were then analyzed by SIMS under conditions described in the experimental section. Figure 4.8 shows the resulting depth profiles. The red profile shows an undoped sample. There is a large step seen in the doped samples which represents the thickness of the nitride formed, while the

last bit of each profile line is indicative of the amount of nitrogen doped into the bulk niobium. Humps seen in the 400 °C and 500 °C samples seem to indicate a small amount of nitrogen beginning to diffuse into the bulk niobium. As the doping temperature is lowered, less nitride forms. Unfortunately, even with the doping temperature lowered to 400°C, nitride is formed at the surface. This indicates, at least on the time scale currently used, nitrogen impurity level cannot be raised without the formation of niobium nitride.

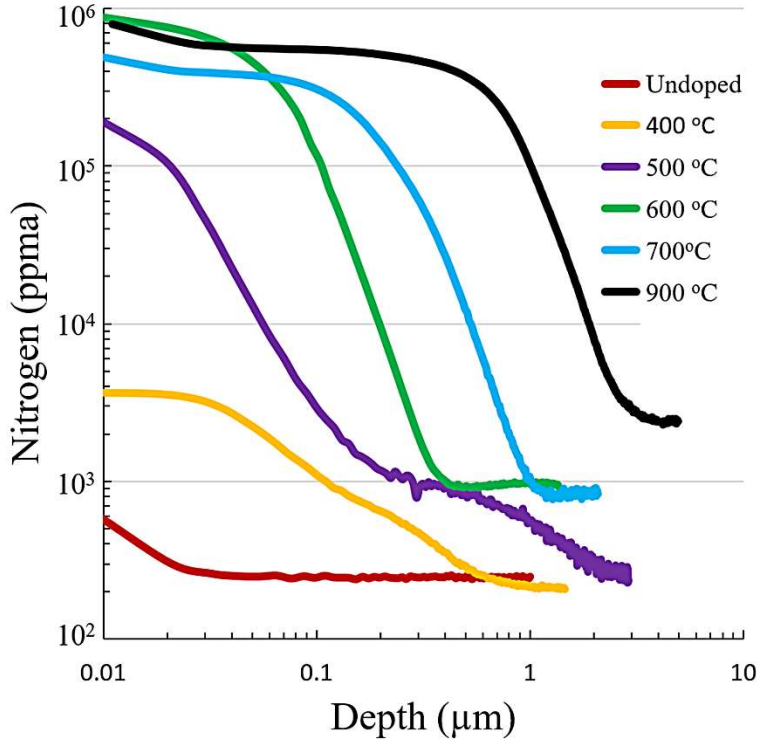


Figure 4.8 SIMS analyses of niobium samples doped at varying temperatures.

4.3.2 Low Temperature Doping

Longer time scale, low temperature experiments are currently under investigation. [34] [57] [58] [41] Referred to as “nitrogen infusion”, cavities show an increase in performance, similar, though not as drastic, as N-doped cavities. Here the process will be referred to as low temperature doping (LTD), as nitrogen appears not to be the sole player in performance gains.

As previously stated, SIMS instruments cannot be optimized simultaneously for depth resolution and sensitivity. [48] For bulk nitrogen measurements or N-doped coupon analysis, the highest priority for a SIMS analysis method is detection limit and proper quantification. For LTD, higher depth resolution is needed to properly describe the sample. SIMS was performed at the lower (8 kV) beam energy, with a depth resolution of 5.6 nm, described in the experimental section.

Preliminary investigation was done using doped (L81) and undoped (L82) NP coupons. Sample L81 was held at 800°C for 3 hours, cooled to 140°C and then exposed to 25 mTorr nitrogen for 48 hours during the same furnace run without exposing the sample to air. Several depth profiles for each sample were averaged and results for the first 50 nm of the

doped and undoped samples can be seen in Figure 4.9. The LTD technique is shown to raise all three impurity levels in the near surface region, having the most dramatic effect on the oxygen concentration.

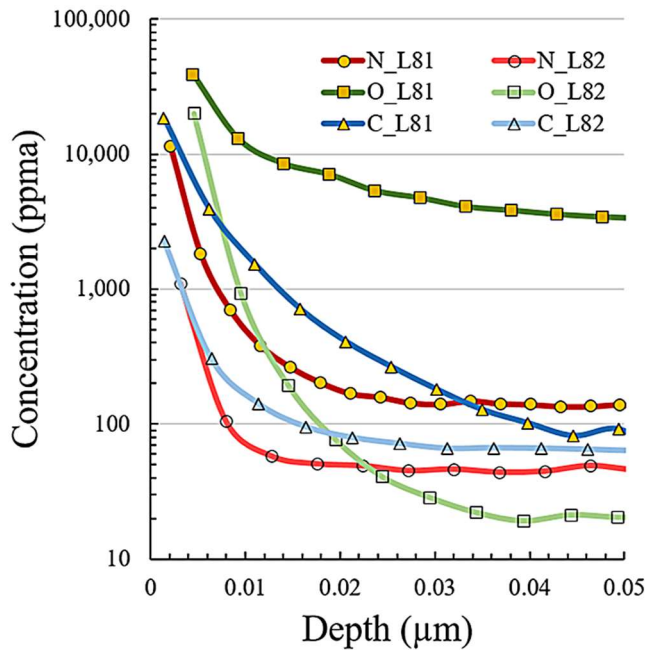


Figure 4.9 SIMS analysis of low temperature doped sample (L81) and undoped sample (L82) in the near surface (first 50 nm).

4.3.3 As-Received Cavity Materials

In this experiment, bulk niobium coupons received from three different suppliers and meant for cavity manufacture were analyzed by SIMS for nitrogen and oxygen content to establish a baseline level for cavity raw material niobium for the first time. At the time of testing, different supplier material and production lots were showing variation in performance tests after N-doping. One possibility is that differing amounts of impurities, most likely nitrogen and oxygen, are present pre-process. Material was used from three suppliers; Wah Chang/ATI, Tokyo Denkai, and Ningxia. Samples were marked W, T and N respectively, with numbers representing different lots of material.

Because of the number of samples, baseline analysis was split over several instrument loads spanning multiple days. With each load a raster reduction test was used to verify the nitrogen and oxygen signal was being detected within the sample and not background generated. Raster reductions for each load of samples appeared similar; Figure 4.4 shows an example raster reduction from this work. The raster reduction shows detected nitrogen originating from the sample, while part of the detected oxygen comes from instrument background. This indicates that while the quantification of nitrogen in samples is correct, actual oxygen levels are at or below the values reported here.

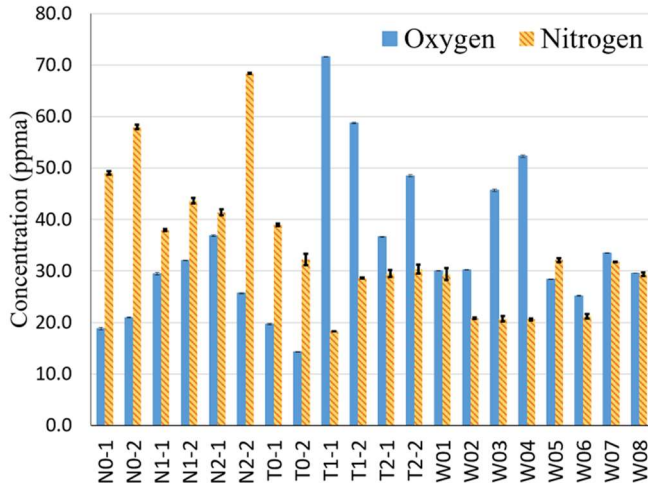


Figure 4.10 Oxygen and Nitrogen quantification with error for “as-received” samples.

The analysis results can be found in Figure 4.10 along with the calculated error for each. As previously mentioned, crystal orientation can affect quantification. Here, errors calculated between analysis regions on each sample are relatively small and representative bars are barely visible in Figure 4.10. This indicates that while grain size is on the same order of magnitude as the analyzed area ($\sim 63 \mu\text{m}$ diameter), the crystal orientation from one analysis area to another does not cause significant variation in measurement. There is variation in nitrogen/oxygen concentration between manufacturer and lot. While error from the average crystal orientation differences between samples cannot be ruled out, total measured concentrations are small compared with doped samples. Results for nitrogen and oxygen in samples prepared to LCLS-II specs were found to be 1-2 ppth(a) and 300-500 ppm(a), respectively. Oxygen concentration across all as-received samples was found to be $34.4 \pm 14.5 \text{ ppm(a)}$, with a maximum of 71.6 ppm(a) . As-received nitrogen concentration was found to be $34.1 \pm 13.0 \text{ ppm(a)}$ with a maximum value of 68.4 ppm(a) . In all cases, the amount of nitrogen in as-received samples was found to be more than an order of magnitude lower than doped samples, indicating as-received values are not high enough to affect performance after doping.

4.3.4 N-Doping Orientation Dependency

Previously, while analyzing bi-crystalline samples, a difference was observed from one side of the grain boundary to the other, giving rise to the question of whether grain orientation has an effect on the doping process. [59] SIMS was performed on each side of a central grain boundary within a few hundred microns of the boundary itself. A graphical representation of analysis placement can be seen in Figure 4.11 along with optical images of the analysis craters.

Figure 4.11 also shows the depth profile data from the four well defined craters. The craters on the left of each set of three are the result of alignment of the primary beam. A clear difference can be seen in the profile from one side of the grain boundary to the other. As crystal orientation is the only differentiating characteristic between the analysis points, it must be tied to the differences seen in the data, either through instrumental effects, such as differences in Y_{tot} , or differences in the sample, such as doped nitrogen concentration.

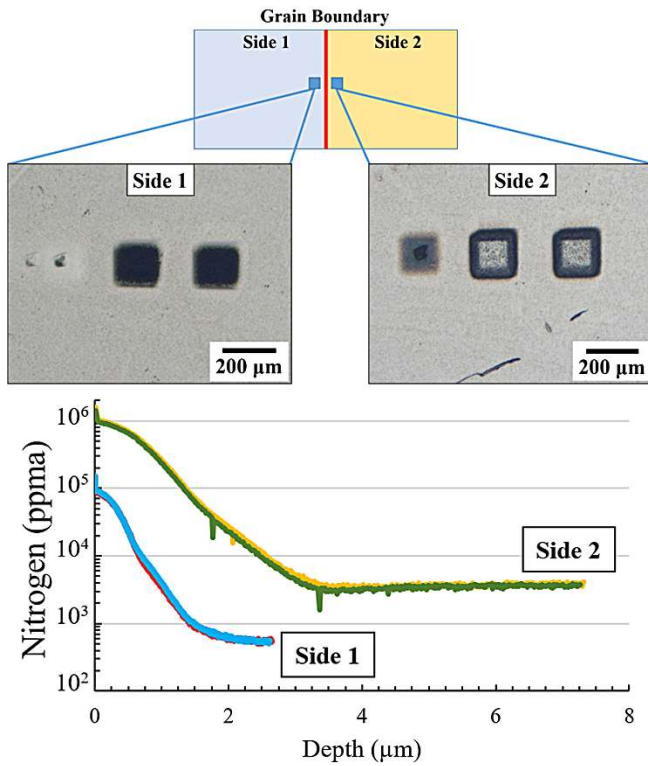


Figure 4.11 Illustration of crater placement, optical images of craters, and depth profile data from SIMS analysis of N-doped (900°C, 10 mins, ~25 mTorr N) bicrystal sample.

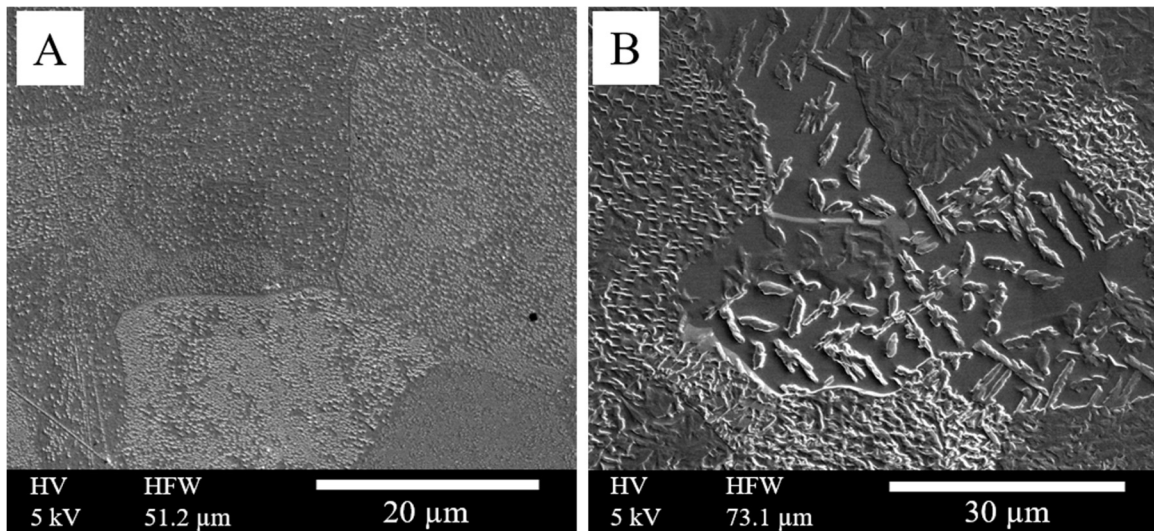


Figure 4.12 Image showing surface of 700 °C N-doped sample (A) and lightly sputtered (focused gallium ion beam, FEI Helios 600) area of 900 °C N-doped sample (B). Both show clear differences in nitride formation from grain to grain.

Crystal orientation is known to affect sputter rate during SIMS analysis. The relative ion yield may also be affected causing differences in quantification. [52] In addition, niobium is a body centered cubic structure, which should not exhibit diffusion rate differences based on orientation. This suggests that the differences seen in nitrogen concentration in the bicrystalline sample may be instrumental related rather than due to the orientation having some effect on N-doping. However, the niobium nitride formed on the surface during

doping plays a vital role in the uptake of nitrogen into the bulk niobium [16], and the orientation dependence for the formation of this nitride can be clearly seen. (Figure 4.12 A and B)

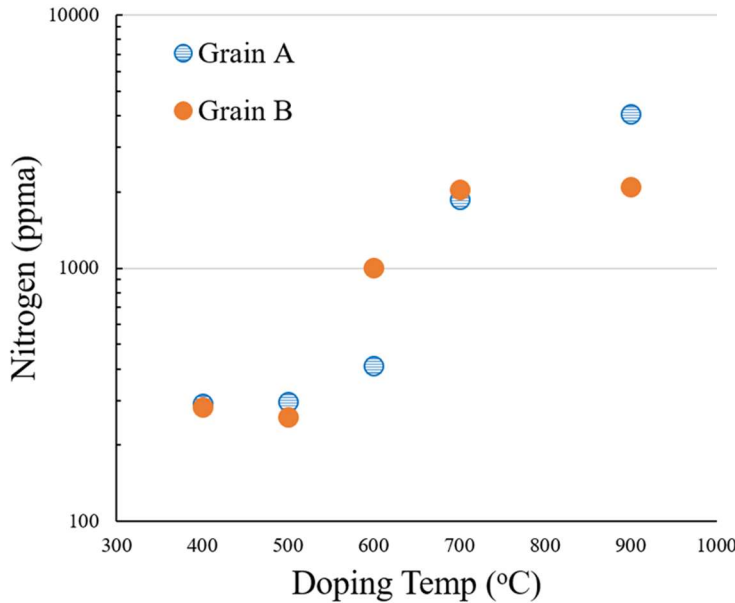


Figure 4.13 SIMS results from bi-crystalline samples doped at different temperatures. Grain A and B represent two sides of a grain boundary.

In order to further investigate, bi-crystalline samples prepared as part of the high temperature doping study were analyzed. Figure 4.13 shows SIMS results from the doped bi-crystalline samples. X-axis shows doping temperature while Y-axis shows measured nitrogen concentration in the bulk. After SIMS analysis, electron backscatter diffraction (EBSD) was used to determine the orientation of each analysis crater. Larger differences were seen in orientation in samples that showed larger differences in N concentration. Figure 4.14 shows inverse pole figures for both grains overlaid for the 700°C and 900°C samples. In contrast to the 700°C sample, the 900°C doped sample shows two distinct orientations between grain A and B. Of note is the 400°C sample, which shows a larger variation in orientation than the 500°C or 700°C samples, but shows less difference in measured N concentration.

RSF values calculated from bi-crystalline and single crystal implant standards have been seen to vary from 10-50% between orientations. However, since implant standards were not available for each possible crystal orientation, an average RSF value was used to quantify the data here. The average RSF was calculated based on data from multiple bi-crystal implant standards and collected using the same instrument conditions (10 kV/-5 kV/100 nA).

While there are significant sources of error to be corrected, evidence seems to point to an orientation dependence for N-doping. Future work could include the meticulous task of creating N-doped and implant standards from the same large grains in order to eliminate uncertainty.

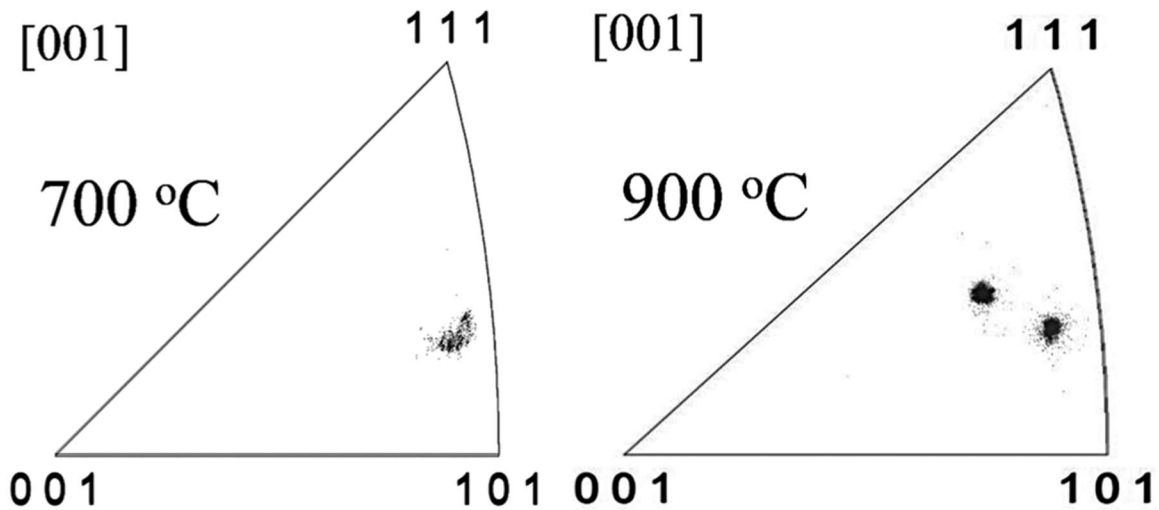


Figure 4.14 Inverse pole figures showing overlays of data collected from grains A and B for the 700 °C and 900°C bi-crystalline samples.

4.3.5 Nb₃Sn Contamination

The discussion above concerns transitioning a demonstrated successful technology (doping) from the research stage to reliably successful deployment: from the state of the art to the state of the practice. Coating with Nb₃Sn has demonstrated attractive potential for more than forty years but has still to demonstrate complete success. The chief shortcoming continues to be unacceptable decline of cavity quality factor with increasing gradient. There has yet to emerge any consensus about the cause.

The ability of SIMS to detect very low concentrations of impurities led us to search for some possible contaminant present in nearly all experiments. Here we consider titanium. A possible source could be the Nb/Ti flanges widely used for their superior mechanical strength. Cornell coated cavities, which tend to have little Q_0 slope compared to those coated elsewhere, use unalloyed Nb flanges. In this study, several witness coupons were coated at Jefferson Lab. Figure 4.15 shows SIMS depth profiles from single crystal and polycrystalline witness coupons coated with Nb₃Sn under cavity coating conditions. In this case, only the absence or presence of titanium is of concern, and the concentration is not quantified, but represented in counts. The depth scale is quantified as the location of the titanium is of interest.

In the case of the single crystal coupon, titanium is seen throughout the thickness of the Nb₃Sn layer, but then quickly falls to the detection limit. When the same experiment is conducted using a polycrystalline witness sample, the titanium signal stays a full decade above the detection limit past the Nb₃Sn layer. Raster reduction method and mass spectra were used to confirm the presence or absence of titanium in the bulk niobium under the Nb₃Sn coating. The difference is possibly due to migration of titanium into the bulk niobium via grain boundaries not available in the single crystal depth profile.

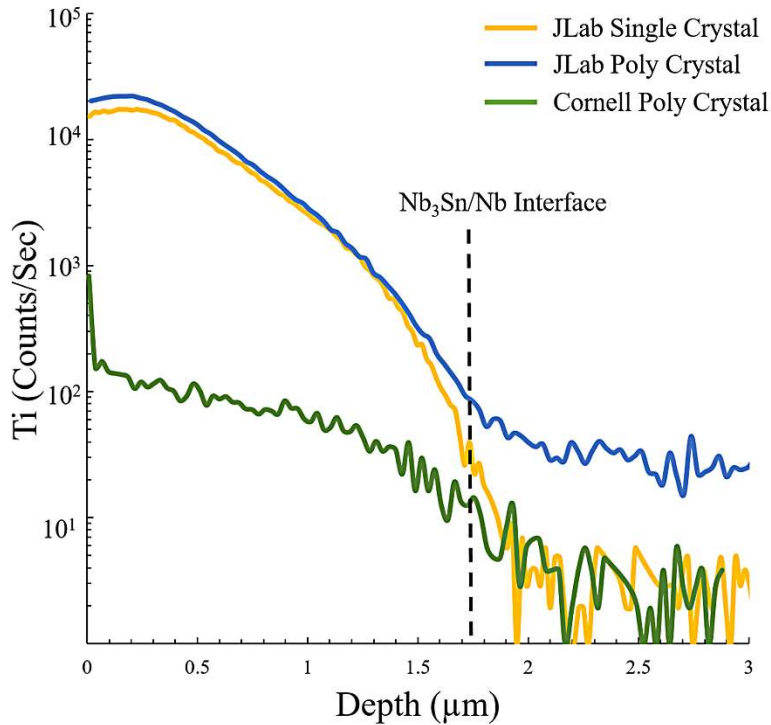


Figure 4.15 SIMS depth profile of Ti in Nb₃Sn coated coupons.

After verifying some test cavities coated at Jefferson Lab contained a “significant” amount of titanium, a Jefferson Lab manufactured cavity was transported and coated at the Cornell facility. Witness coupons were coated along with the cavity. Figure 4.15 also shows the SIMS depth profile of the Cornell witness sample. While the titanium signal has not been quantified, it has been normalized based on the matrix signal, and by comparing the titanium signal difference between the Cornell and Jefferson Lab witness samples, it is clear the Jefferson Lab coated samples contain a considerably greater amount of titanium. Currently cavity performance testing is underway to resolve whether these differences are causative of cavity performance effects.

4.4 Conclusion

There are several materials-based technologies being developed that promise to push SRF performance forward, resulting in higher performing and more efficient particle accelerators. In order to push such technologies forward in a timely and efficient manner, accurate and robust materials characterization techniques are needed, linking a material’s structure to processing and performance. SIMS has proven vital in the goal of linking processing, structure, and performance. Examples presented here include work that confirms that, at the currently used doping times, nitrogen impurity level cannot be raised usefully without formation of a significant niobium nitride surface layer. Low temperature doping is shown to raise carbon, oxygen, and nitrogen levels within the RF penetration depth, suggesting N may not solely be responsible for the performance enhancement of low temperature doped cavities. Analysis of SRF cavity raw materials from three different suppliers reveals nitrogen concentrations in as-received samples to be more than an order of magnitude lower than doped samples, indicating nitrogen levels in raw materials are not

high enough to affect the doping process or cavity performance afterwards. Evidence from SIMS analyses of single crystal regions demonstrates evidence that N-doping is dependent on the bulk niobium crystal orientation. SIMS was also used for contamination analysis for Nb₃Sn coatings, indicating differences in titanium concentration between coupons coated at Jefferson Lab and Cornell.

4.5 Acknowledgement

Co-Authored by Jefferson Science Associates, LLC under U.S. DOE Contract No. DE-AC05-06OR23177. We are grateful for support from the Office of High Energy Physics, U.S. Department of Energy under grant DE-SC0014475 to the College of William & Mary.

The Institute for Critical Technology and Applied Science (ICTAS), and Nanoscale Characterization and Fabrication Laboratory (NCFL) at Virginia Tech. Stanford Linac Coherent Light Source II (LCLS_II) for supplying the Ningxia and Tokyo Denkai production material samples.

Appendix A

A.1 Orientation Effects on Doping Supplemental

During the conventional SIMS work discussed previous there has been evidence that the doping process is orientation dependent. This has been discussed (4.3.4) and can be seen in Figure 4.11. In order to further investigate, a combination of EBSD and small spot size SIMS was utilized. With the Cameca 7F, analysis spots of ~15 μm were used and found to preserve enough sensitivity for nitrogen detection. As described in section 4.2.1, this was accomplished by rastering a 5nA Cs⁺ beam with a size of ~5 μm over a 10 x 10 μm^2 area. Niobium coupons used for the high temperature doping experiment (found in section 4.3.1) have grain sizes in the range of 50-100 microns. This combination allows for single grain analyses of doped samples.

As a first step, FIB was used to place fiducial grids on the surfaces of N-doped coupons. Figure A. 1A shows an optical image of a grid, which is marked with a roman numeral for identification. The total grid size was 250 x 250 microns with a grid spacing of ~42 μm . Figure A. 1B shows an SEM image of the same grid. EBSD was then used to map the gridded area (Figure A. 1C) to determine orientation within specific grid boxes. Small spot size SIMS was then used to analyze different areas/orientations using the grid as a guide. Figure A. 1D shows SIMS data collected from eight different areas representing different orientations. Nitrogen concentration at depth within the profile seems very similar between analysis points. Analysis indicates a uniform concentration of nitrogen in the bulk material after doping. This is not surprising as previously discussed bulk niobium is a cubic structure and should show uniform diffusion in all directions, therefore once the doped nitrogen makes it past the nitride layer it is free to homogenize within the bulk material. While the experiment shows homogeneity of nitrogen concentration and indicates bulk concentration of a specific area is non-dependent on the orientation of the specific grain above, it does not test the effect of a cavity's average orientation on the bulk nitrogen concentration post doping. The experiment does seem to indicate, at least at these analysis conditions, instrumental factors are not solely responsible for differences shown and discussed in

section 4.3.4. A third experiment, in which single crystal coupons are doped with corresponding implant standards could be undertaken to further clarify.

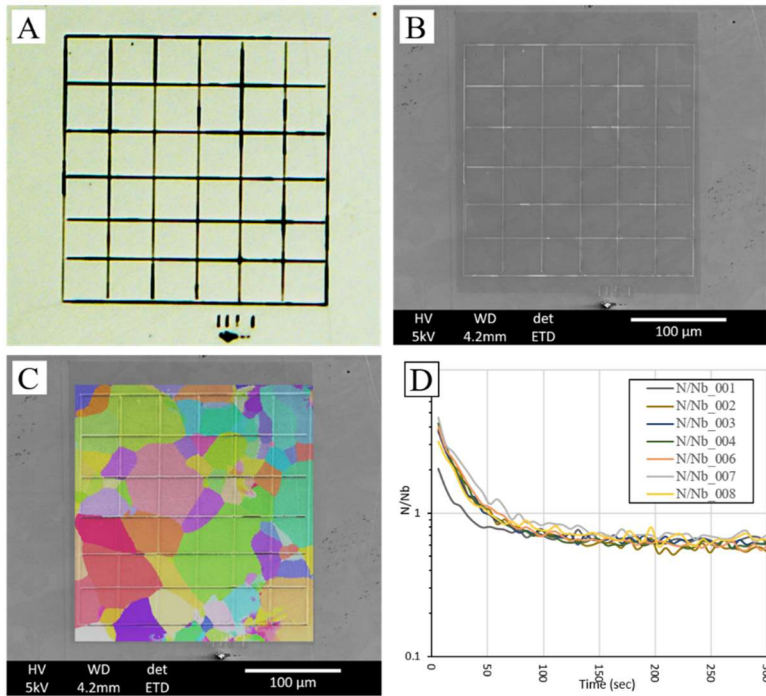


Figure A. 1 Figure showing steps for grain/orientation specific SIMS analysis. (A) Optical image of 250 x 250 micron grid placed on sample surface using FIB. (B) SEM image of the same grid. (C) EBSD map of grain orientation laid over the grid pattern. (D) SIMS analysis of eight different grains/orientations within the mapped area.

Chapter 5

5 XPS for SRF Cavity Materials: Determining Material Composition as a Function of Depth

In order to continue the advancement of SRF materials technologies it is critical to have accurate and repeatable characterization techniques for measuring a material's composition as a function of depth. Here we explore the use of XPS as a tool for characterizing composition of SRF materials as a function of depth by sputter depth profiling. While XPS is found not suitable for low concentration nitrogen analysis, examples are shown demonstrating the technique's use in characterizing coated samples such as vapor deposited Nb₃Sn. In addition, the technique of angle polishing sample preparation is demonstrated to extend reachable depths for profiles to hundreds of microns.

5.1 Introduction

5.1.1 Motivation

The world's most powerful microscopes (particle accelerators) operate at the edge of science, pushing the frontier of knowledge. In order to keep pushing the frontier further, higher and higher energy particle accelerators are needed. The motivation for higher energy accelerators is two-fold. Ultimate resolution, as with the light and electron microscope, is controlled by the wavelength of the source. Higher momentum (p), as seen in De Broglie's equation $\lambda = \frac{h}{p}$, brings shorter wavelengths (λ) and the ability to resolve finer details within a particles structure. In addition, over time higher and higher mass particles have been discovered. As shown by Einstein's $E = mc^2$ ever higher energies are needed to create and study these massive particles.

Currently, from a materials point of view, there are two technologies leading the pack for next generation accelerators; doped niobium, which lowers surface resistance by using small amounts of impurity to add scattering centers and tune the mean free path, and Nb₃Sn, an A15 intermetallic compound used to coat the interior surface of SRF cavities giving superior theoretical performance over solid niobium cavities. These two material technologies are game changing for SRF accelerators, however, full understanding of these materials has yet to be realized. For both materials it is important to understand the concentrations and speciation of the components as a function of depth. The depth of interest can vary from the top tens of nanometers, for some doped materials, to several microns for Nb₃Sn coatings. With both materials the top ~200 nm is of significance, as the RF penetration depth for niobium is ~40 nm and Nb₃Sn is ~170 nm. This surface layer controls the cavity's performance more than any other single factor.

One way to measure elemental concentration as a function of depth is with an ion beam technique such as secondary ion mass spectrometry (SIMS), where concentrations of components are measured as an ion beam is used to sputter into the sample, resulting in concentration versus depth information for the species of interest. When dealing with quantification of low concentration species as a function of depth, dynamic SIMS, is

without equal. A discussion of SIMS for SRF cavity material analysis can be found in the previous chapter and reference. [60] SIMS analyses can be quite complicated and instrumentation is more expensive and less common than other techniques. It would be beneficial to have a more available and less complicated technique for concentration measurements as a function of depth that still provides acceptable detection limits. A good candidate is X-ray Photoelectron Spectroscopy (XPS), the most available and widely used surface analysis technique.

XPS uses x-rays to excite the sample surface. This excitation causes core level electrons to eject from the surface with a characteristic energy (kinetic energy) directly related to the binding energy. These ejected characteristic electrons are then analyzed and typically presented as a graph of counts per second versus electron binding energy. The intensity for a specific photoelectron peak can be determined by integration and concentration of the originating element can be determined with the application of an experimentally determined relative sensitivity factor. In some cases, bonding information can also be determined, allowing, among other things, oxide species and thicknesses to be determined.

XPS is a much less complicated technique in terms of operation, data analysis, and quantification than SIMS and while the quantification limits for XPS are generally considered to be ~ 1000 ppm, this is not a hard rule and lower detection limits can often be achieved. For these reasons, including wide availability, a study was started to determine the viability of using XPS for characterization of N-doping and Nb₃Sn coatings.

5.2 Experimental

5.2.1 X-ray Photoelectron Spectroscopy

The XPS measurements were carried out in an ULVAC-PHI “Quantera SXM” instrument equipped with a monochromated aluminum anode. Surface analyses were collected at 50W/15 kV using a 200 μm spot size, 45° take off angle. Survey scans were done using a pass energy of 280 eV while high resolution scans used a pass energy of 26.00 eV. Surface charge compensation was achieved using a low energy electron flood gun.

For depth profiles, sputtering was accomplished via an argon ion source at 5kV over a 2 x 2 mm area. Depth profile data was collected at 50W/15kV with a spot size of 200 μm , 45° take off angle and 140 eV pass energy. Data were collected at $t = 0$ and then at time intervals which varied based on sputter rate and data density needed for the analysis.

5.2.2 Samples

Unless otherwise stated, samples were 10 mm square coupons cut by electrical discharge machining from trimmings of the 3 mm thick niobium sheet used to make SRF cavities (“RRR grade”). Typical grain size for polycrystalline material is in the 50 μm to 100 μm range in the un-annealed state. All were subjected to buffered chemical polishing (BCP) using a solution of 49% HF, 70% HNO₃ and 85% H₃PO₄ in the ratio of 1:1:1 by volume with minimum removal of 50 μm . These samples further received metallographic polishing, also known as nanopolishing (NP) [55], which typically removes > 100 μm and produces surface roughness on the order of a few nanometers. [61] Results from 700°C and 900°C N-doped coupons are reported. The coupons were doped for 20 min and 10 min respectively at ~ 25 mTorr nitrogen pressure. Further details can be found in reference [62].

Nb₃Sn results reported are from a sample coated by vapor deposition at 1000°C for 12 hr. Further details of the Nb₃Sn coating can be found in reference [63].

5.3 Results and Discussion

Elements with small photoelectron cross sections, such as nitrogen, present a challenge to detect at lower concentration. Smaller photoelectron cross section elements show diminished peak intensities, resulting in lower signal to noise ratios as compared to elements of large cross section. This can affect both precision and accuracy of quantification. While most elements with larger photoelectron cross sections may exhibit only a few tenths of a percent error, elements with low photoelectron cross sections can exhibit large errors of a percent or more. At lower concentrations this can result in proportionally large amounts of error. Concentrations of nitrogen in doping samples have been found to vary from several hundred to a few thousand ppm, near the detection limit of XPS. [60] Figure 5.1 shows a survey scan of the surface of the polycrystalline niobium coupon nitrogen doped at 900 °C with quantitation. Survey scans are relatively quick scans over a large range of binding energies and are used to “survey” the surface and quantify elements found there. Oxygen, niobium, and nitrogen can clearly be seen on the coupon surface, consistent with a surface of niobium nitride and niobium oxide, indicating at least at surface nitride concentrations XPS is sensitive enough for quantification.

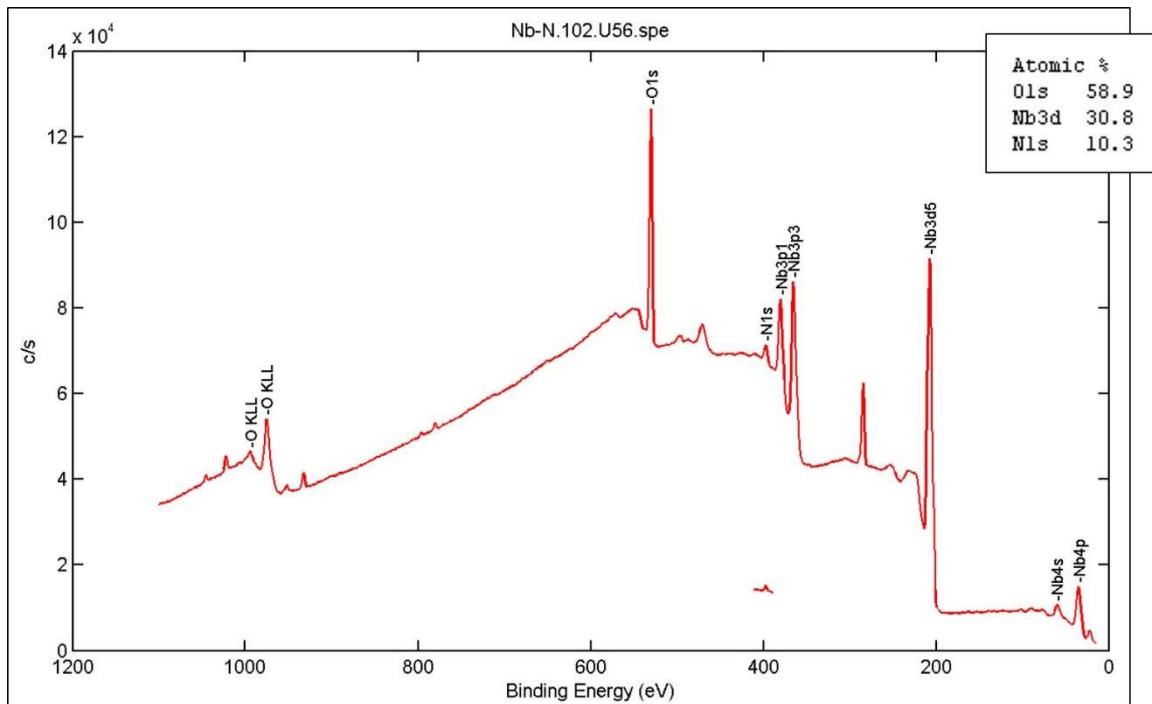


Figure 5.1 XPS survey scan of 900 °C polycrystalline N-doped niobium coupon.

5.3.1 Sampling Depth

Initial survey data (Figure 5.1) shows it is possible to detect and quantify nitrogen in N-doped niobium, at least in the nitride containing surface region where nitrogen concentration is relatively high. In order to have a complete understanding of XPS data collected moving forward it is important to understand from where in the sample the data

originates. As X-rays bombard the sample electrons are excited and escape their orbitals with a kinetic energy determined by the electron's binding energy. While X-rays penetrate far into a sample only electrons produced shallower than some limiting depth or escape depth can be detected and quantified. Electrons below this escape depth lose energy due to inelastic processes and constitute the background shown in the survey. Escape depth and therefore analysis depth can be estimated by calculating an electrons attenuation length (λ). Attenuation length for electrons will vary with kinetic energy and the material through which it passes (based on the inelastic mean free path). In order to determine analysis depth for the species of interest, λ values were calculated based on work by Seah and Dench (1979) [64], using equation:

$$\lambda = \frac{538a}{E^2} + 0.41a(aE)^{0.5}$$

Equation 5.1

Where a^3 is the volume of the element or molecule in nm^3 , E , in eV, is the kinetic energy relative to the XPS emission line considered. Care must be taken in choosing the form and coefficients (here λ is the attenuation length in nm) but is many times calculated as monolayers. [65, 66, 67] Attenuation length for niobium was calculated to be 1.97 nm for Nb3d in bulk niobium, similar values were found in previous works. [66, 68, 69, 70]

Table 5.1 Variables and calculated attenuation length (λ) values. Values for λ were calculated using Equation 5.1.

Niobium Bulk Material				
Species	Peak	a (nm)	E (eV)	λ (nm)
Nb	Nb3d		1284.7	1.97
Nb2O5	Nb3d		1279.5	1.97
Nb2O5	O1s	0.26	956.2	1.70
NbN	Nb3d		1284.0	1.97
NbN	N1s		1089.5	1.82
NbO	Nb3d		1283.5	1.97
Nb₂O₅ Bulk Material				
Species	Peak	a (nm)	E (eV)	λ (nm)
Nb	Nb3d		1284.7	6.11
Nb2O5	Nb3d		1279.5	6.10
Nb2O5	O1s	0.46	956.2	5.27
NbN	Nb3d		1284.0	6.11
NbN	N1s		1089.5	5.62
NbO	Nb3d		1283.5	6.10

While Equation 5.1 is a good estimate of λ , it does not take into account factors such as elastic scattering as with more complicated methods. As a check of the accuracy of Equation 5.1 the NIST Electron Effective-Attenuation-Length Database was used to determine λ for Nb3d in bulk niobium and found to be 1.92 nm, in good agreement with results from Equation 5.1. [71] Due to ease of use and general accuracy, Equation 5.1 was used to calculate λ for all species of interest. Values for λ were calculated for Nb₂O₅ and niobium as the bulk material to help understand how depth resolution and signal

generation can vary within the near surface region. A depth of λ will emit 65% of the scattered electrons, while a depth of 3λ takes into account 95% of the electrons generated. In summary, λ for Nb3d emission lines were calculated as 1.97 ($\pm 0.2\%$) nm for bulk niobium and 6.1 ($\pm 0.6\%$) nm for Nb₂O₅. Complete results with variables used can be found in Table 5.1. Results in Table 5.1 illustrate the dominance the bulk material has on sampling depth. Typical thickness of Nb₂O₅ has been found to be ~ 4 nm. [66] When considering 3λ for Nb₂O₅ is ~ 18.3 nm, this amount of oxide only has a small impact on overall sampling depth and can be ignored. With differing species of interest and niobium oxide making such small contributions to attenuation length it is reasonable to consider sampling depth to be that of bulk niobium, ~ 6 nm (3λ) for all species of interest.

5.3.2 Depth Profiling of Nitrogen Doped Niobium

As shown in Table 5.1, typical sampling depths for niobium, nitrogen, and oxygen analysis in bulk niobium are within the top ~ 6 nm of the surface. However, in order to characterize entire RF penetration depths, doping gradients, or layered materials, such as Nb₃Sn, deeper analysis is needed. The XPS used here is equipped with an argon sputter gun, which can be used to create depth profiles by alternately sputtering and analyzing the same area of the sample. Figure 5.2 shows a depth profile produced for a N-doped sample processed at 900 °C. Oxygen signal can be seen to fall to baseline within the first five cycles of sputtering, which corresponds to the first ~ 100 nm. Over the first 1-1.25 μm the nitrogen level stays fairly constant, then falls quickly to a low level, indicating the removal of the NbN layer. The niobium signal can be seen to inversely mimic the nitrogen signal eventually rising to ~ 100 at%.

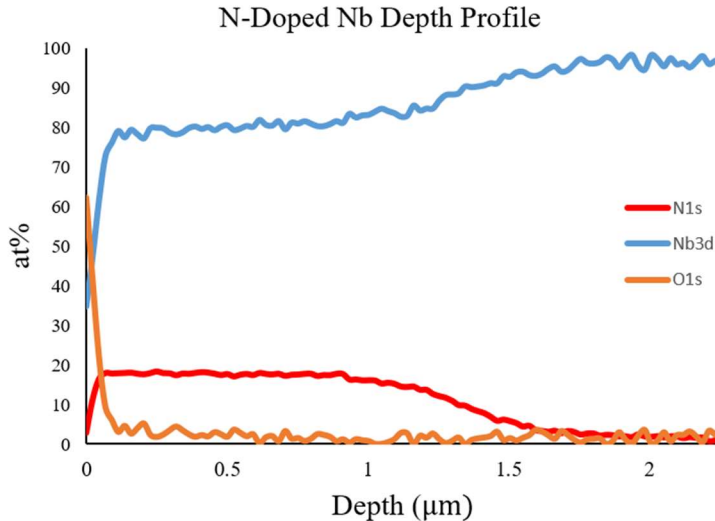


Figure 5.2 XPS depth profile of 900 °C doped sample. Depth profile is based on high resolution scans performed alternating with argon sputtering of the sample.

Figure 5.3 shows the high energy resolution scans used to build the depth profile (Figure 5.2), where each line represents a different depth in the sample. Figure 5.3A is dominated by the O1s signal from Nb₂O₅ at 530.4 eV. The very slight shoulder (530.77 eV) seen on the high energy side of several scans may be attributed to other niobium or NbN oxides seen just under the surface. All N1s scans (Figure 5.3B) except the initial surface scan show a single peak located at 397.2 eV. The initial surface exhibited a small shoulder at

396.0 eV attributable to an NbN oxide, most likely $\text{NbN}_{1-x}\text{O}_x$ ($X < 0.5$). [72] Figure 5.3C shows the evolution of the Nb3d through the depth profile from Nb_2O_5 (207.1 eV) and NbO (203.1 eV) at the surface and near surface to bulk Nb (201.9 eV) at the deepest. Shifting binding energies between the NbO and Nb peak are most likely due to NbO_x where x varies with unstable stoichiometry due to the sputtering process.

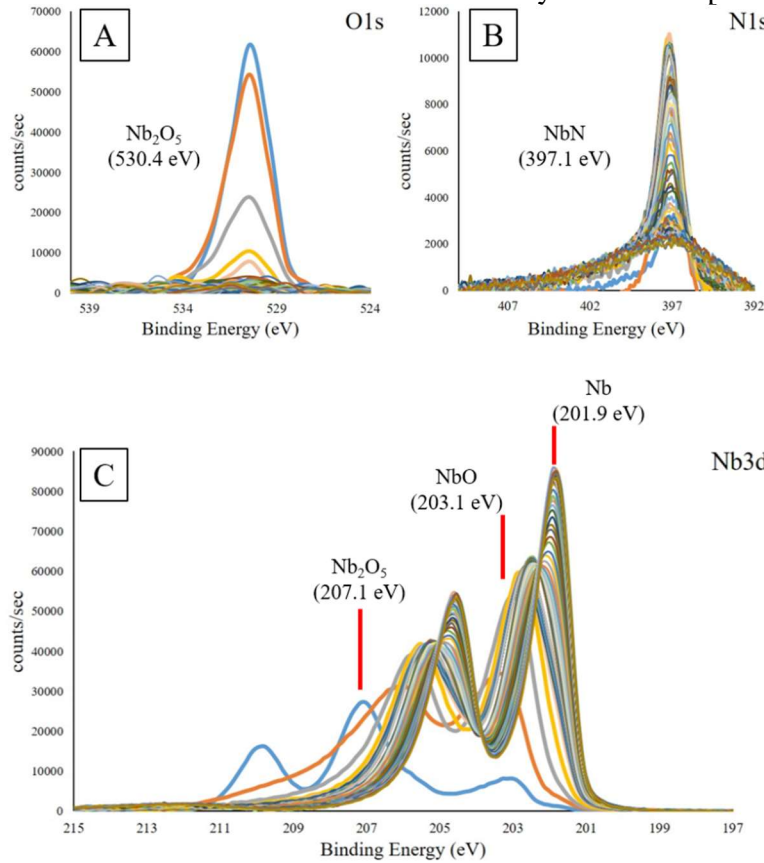


Figure 5.3 High resolution scans of (A) oxygen, (B) nitrogen, and (C) niobium from depth profile of a 900°C doped polycrystalline sample (Figure 5.2).

The nitrogen concentration calculated reaches a steady state concentration of 1.2 at% at approximately 2 μm . SIMS measurements at the same depth put the actual concentration at 0.53 at%. The baseline nitrogen level of the sample was calculated by SIMS to be 0.24 at%. There are likely several factors affecting the accuracy of the XPS quantification of nitrogen shown here. As previously mentioned nitrogen has a relatively small photoelectron cross section, making signal intensities low per amount relative to other elements. In addition, the N1s peak falls within the loss region of Nb3p, making difficult the separation of intrinsic photoelectrons from extrinsic scattered photoelectrons which make up the background. Changes in background (endpoint) selection can have a large effect on quantification results for smaller peak sizes. Figure 5.4 shows two high resolution scans covering the Nb3p and N1s binding energies, one from a niobium coupon which has been N-doped and one which has not. Figure 5.4 and Figure 5.3B demonstrate the N1s peak position at the same approximate binding energy as the Nb3p loss peak resulting in a muddled baseline subtraction. This results in the falsely high quantification of nitrogen at baseline of 1.2 at%, which represents the detection limit of the instrument at the time of analysis. XPS may provide a suitable technique for experiments involving the near surface

nitride region, with an achievable detection limit of ~1 at% for nitrogen. However, XPS does not provide a viable option for the quantification of bulk nitrogen levels in N-doped niobium.

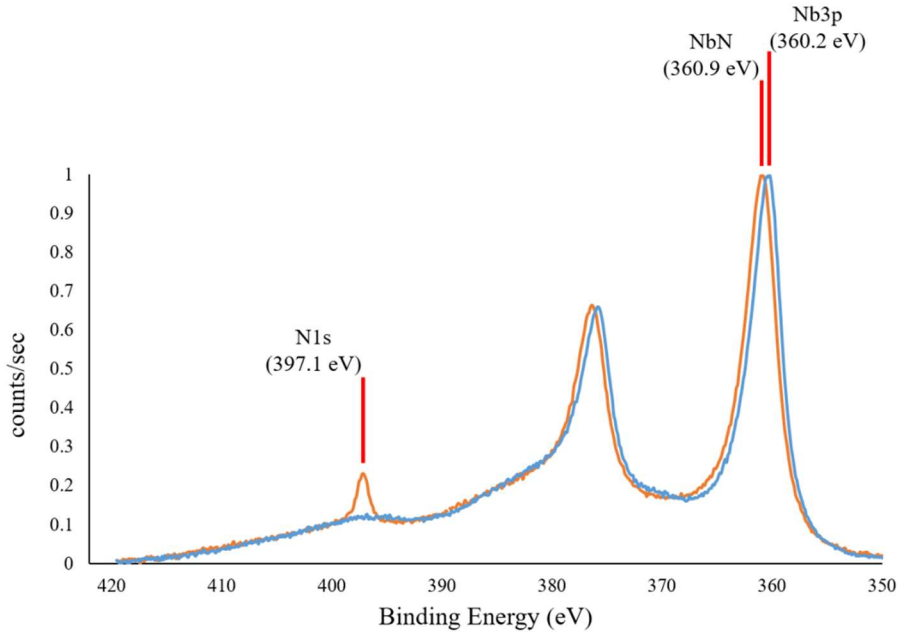


Figure 5.4 Two high energy resolution scans covering the Nb3p and N1s binding energies, one from a niobium coupon which has been N-doped (shows N1s) and one which has not been doped.

5.3.3 Angle Polishing

Concurrently with the above experiments “angle polishing” was evaluated as a viable alternative to traditional depth profiling for both XPS and SIMS analysis. The ultimate depth of a depth profile is limited in both cases. Most XPS instruments use a diffuse low energy ion sputter gun (argon in our case). This leads to a poorly defined crater, making direct depth quantification difficult, and very long profile collection times, even for rather shallow (<1 μm) profiles. While SIMS can achieve much faster sputter rates and well-defined craters, the technique is still limited to depths of ~20 μm or less in most cases and by acquisition time (several hours for deeper craters). In the case of an angle polished sample the cross-section depth can be “magnified” many times depending on the angle of polish. This allows analysis of many hundreds of microns in depth by analyzing different locations on the polished surface.

A 6 x 6 mm sample, N-doped at 700 °C and ~25 mTorr N for 20 mins, was used for method evaluation. Figure 5.5 shows a graphic representation of the sample polishing. The sample was manually polished at a controlled angle of 3 degrees, later measured to be 3.065° by profilometry. This angle along with the measured length of the polished section can be used to calculate a total depth of polish, 208 μm in this case. With analysis position information and crater/sampling depths, exact depths of analysis can be calculated relative to the original surface.

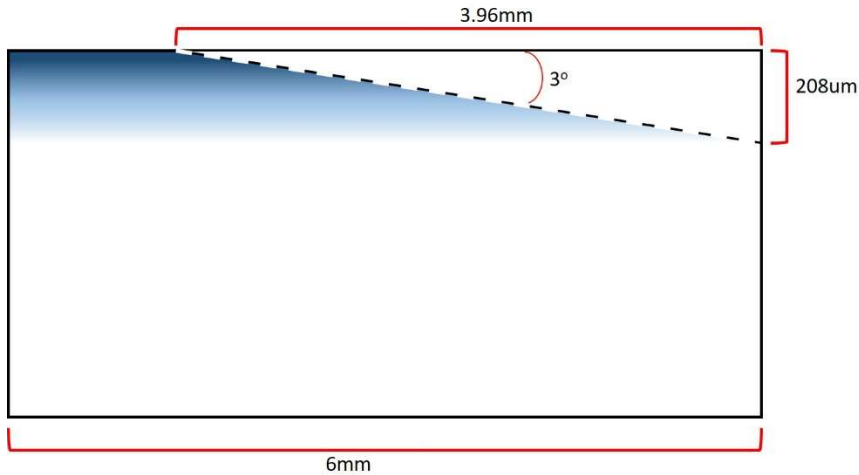


Figure 5.5 Graphic representing angle polished sample; Blue represents N-dope profile, Solid black line shows original surface of the sample, dashed black line shows newly created polished surface used for analysis at varying depths.

The angle polished sample was initially analyzed by SIMS. Multiple craters were placed along the polished and original surface. The craters were 150x150 µm in size, which at a polish angel of 3° gives a range of depth of ~8 µm for each crater. Figure 5.6 shows the angle polished sample with positioning of SIMS craters to give analyses at different depths. While the surface appears rough in the optical image the measured roughness of the polished surface was found to be ~23 nm over several hundred microns by profilometry. An implant standard was used to quantify the nitrogen concentration, while the size, depth, and position of each crater was used to calculate the depth of each data point. Results can be found in Figure 5.7.

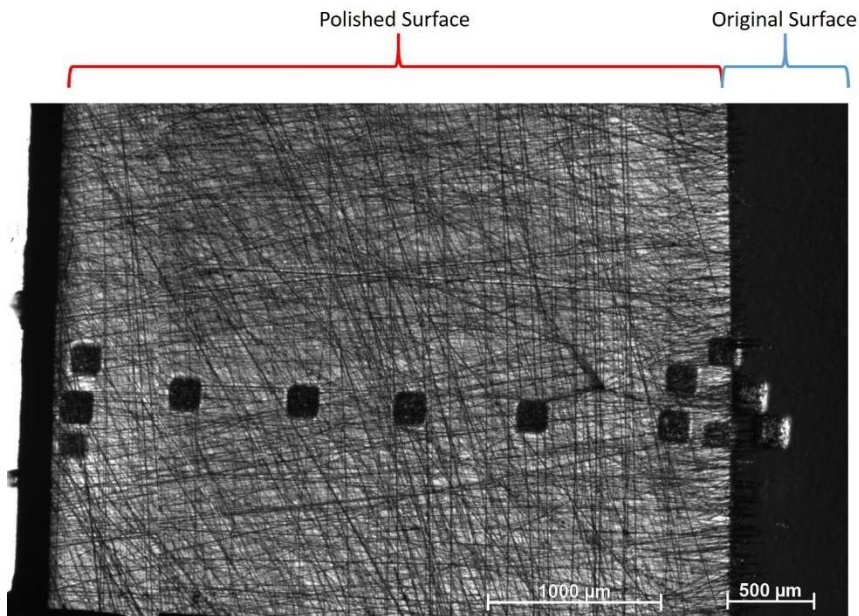


Figure 5.6 Angle polished sample with 150x150 µm analysis craters spaced along the polished surface. Giving analysis at different depths.

SIMS results for the 700 °C N-doped sample have been previously reported, nitrogen concentration at 1 μm depth was found to be ~1000 ppma, which is in good agreement with results from Figure 5.7. [60] Nitrogen concentration of the bulk material is shown to be ~300 ppma, approximately an order of magnitude higher than previously analyzed SRF cavity raw material. [60] This indicates relatively fast nitrogen diffusion through the bulk niobium at higher doping temperatures. Data was similarly collected by XPS but as shown earlier detection limits are not low enough. The angle polish technique could be used in conjunction with XPS for higher concentration samples.

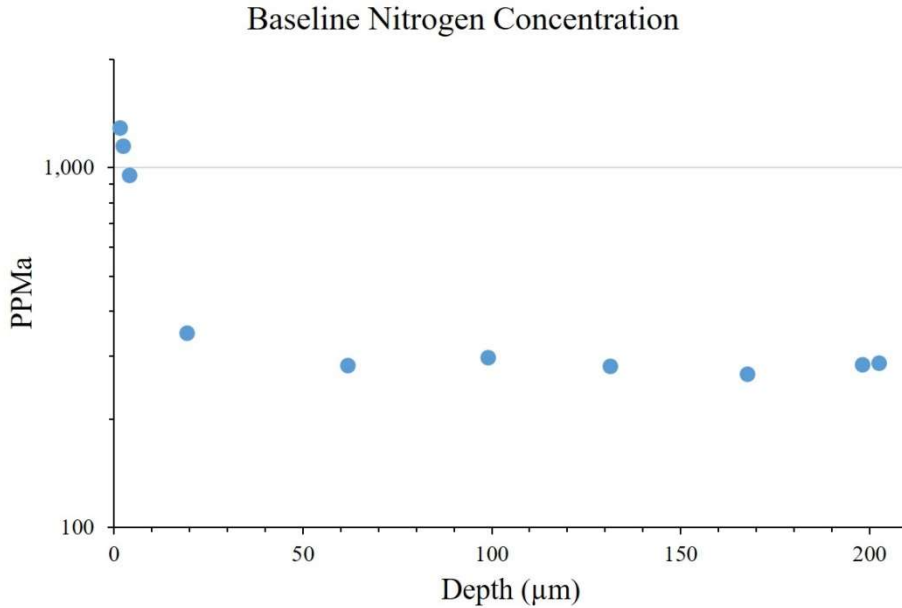


Figure 5.7 Concentration vs Depth plot for SIMS analysis of angle polished sample (700 °C N-doped).

5.3.4 Depth Profiling of Nb₃Sn

While XPS may not be a viable replacement for SIMS for depth analysis of N-doped materials due to the low concentrations of nitrogen present, it may serve as a convenient technique for characterization of materials such as vapor deposited Nb₃Sn, where species of interest are in the bulk domain rather than at trace levels. Figure 5.8 shows an example depth profile from a niobium coupon coated with Nb₃Sn (1000°C for 12 hr). The depth profile was sputtered using 5 kV argon over a 2x2 mm area. The sputter rate was estimated at ~50 nm/min based on empirical data from sputtering alternating layers of niobium and tin of known thickness. An initial data point was collected at the surface and then after every 30 sec of sputtering until a baseline concentration of tin was reached. The oxygen signal is seen to fall to baseline after the first sputter cycle, consistent with a surface of mostly niobium and tin oxides only a few nm's in thickness. Tin concentration remains constant until ~2 μm. After which tin concentration falls to baseline and niobium increases to 100%, indicating the thickness of the Nb₃Sn layer. The Nb₃Sn/Nb interface appears as a gradual slope due to the polycrystalline nature of the coating. This is from a combination of reduced depth resolution due to preferential sputtering and the inconsistent nature of Nb₃Sn grain growth.

In multi-component materials, such as Nb_3Sn , sputter yields can vary for different elements. This preferential sputtering can cause roughening which affects depth resolution and also changes the elemental make-up of the surface, making quantification of the bulk material difficult. While alternate techniques such as electron backscatter diffraction (EBSD) verified the presence of microns thick Nb_3Sn layer, Figure 5.8 does not show stoichiometric amounts of niobium and tin expected for Nb_3Sn . Quantified niobium and tin concentrations were averaged within the Nb_3Sn layer ($0.5 \geq 1.5$ microns) and found to be 83.4 and 16.6 at% with a standard deviation of 0.8 at%. The difference from the expected stoichiometric amount of 75.0 and 25.0 at% is credited to preferential sputtering of tin.

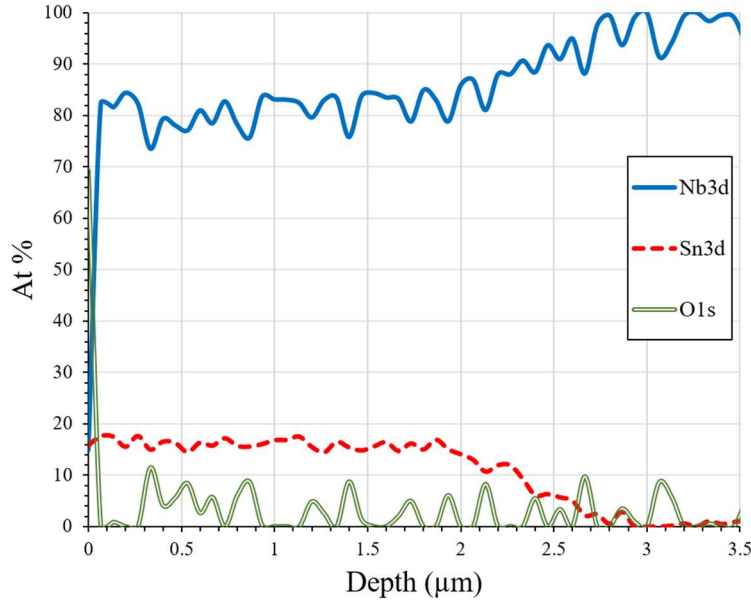


Figure 5.8 : Depth profile of a niobium coupon coated with Nb_3Sn . Analyzed by XPS with argon sputtering used for material removal.

5.3.5 Dependence of Preferential Sputtering on Ion Beam Condition

Depending upon the goals of a particular experiment it may be necessary to vary the sputter rate and damage layer produced when sputtering. Damage depth and sputtering rate are controlled, in large part, by the ion choice (argon in this case), incidence angle, and ion accelerating voltage. For the system here commonly used accelerating voltages range from 1-5 kV sputtered over an area of 2×2 mm, while ion choice and incident angle are held constant. Changes in ion beam accelerating voltage can potentially affect preferential sputtering, making comparison of relative concentrations difficult. For instance, it is convenient to profile Nb_3Sn coated samples at 1kV over the first ~ 100 nm to characterize the RF penetration depth well. Then perform the rest of or a separate depth profile at 5kV to produce a much higher sputter rate in order to analyze a several microns thick layer in an acceptable amount of time. In order to confidently compare collected data it is necessary to demonstrate no appreciable difference in preferential sputtering between 1kV and 5kV conditions. Figure 5.9 shows a depth profile of a Nb_3Sn coated coupon ($1000^\circ C$ for 12 hr) sputtered at 1 kV and at 5 kV. No meaningful difference can be seen. Quantified niobium and tin concentrations were averaged within the Nb_3Sn layer ($20 \geq 100$ nm). The 1kV

sample was found to be 82.8 at% Nb and 17.2 at% Sn with a standard deviation of 0.5 at% and the 5kV sample 82.4 at% Nb and 17.6 at% Sn with a standard deviation of 0.6 at%.

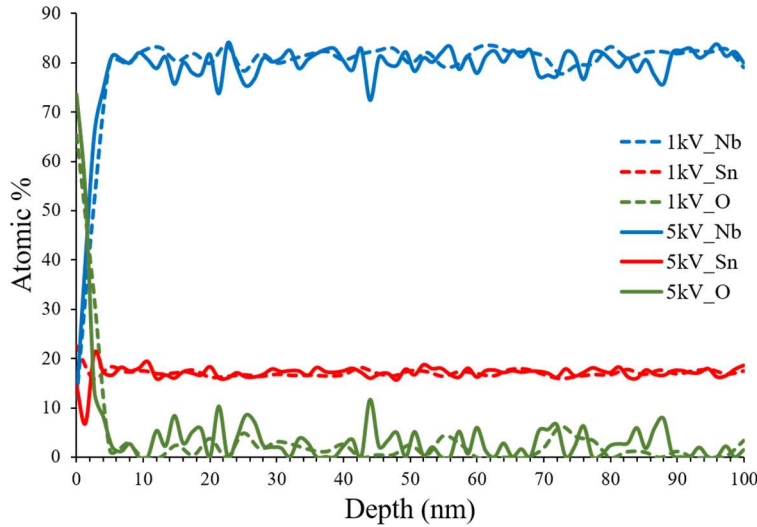


Figure 5.9 Depth profiles of a Nb₃Sn coated sample sputtered at 1 kV and 5 kV, which demonstrates no difference in preferential sputtering between the two sputtering conditions.

5.3.6 Error in Nb₃Sn Depth Profiling Measurements

To help further understanding of the data collected and possible error, spectra were collected under many instrument conditions and quantified in various ways. Among the instrument and collection parameters varied were pass energy, step size, spot size and beam power. Quantification was done using various combinations of Nb3d, Nb3p3, Sn3d, and Sn3d5 peaks. Also, quantification was done with and without curve smoothing and with various background subtraction. Over all collected spectra under various conditions, standard deviation was found to be +/- 0.95 at%. Spot size and beam power are tied together and conditions smaller than 50 μm / 12.4 W were found to have significantly higher error, ≥1.4 at%. It is unclear if is due to higher than normal signal to noise, although peaks did appear well defined, or a non-homogenous sample surface. Only data from beam conditions larger than 50 μm / 12.4 W were used to calculate the error reported above.

5.4 Conclusion

As part of an overall goal of expanding materials characterization for SRF cavity materials, XPS is explored as a depth profiling technique for determining concentration as a function of depth. The XPS technique was found capable of detecting and quantifying nitrogen for concentrations above approximately 1 at%. This detection limit is not suitable for the low concentration nitrogen analysis needed to accurately describe nitrogen doped niobium, leaving SIMS as the technique of choice. XPS sputter profiling does however provide acceptable analysis for non-trace characterization. Example depth profiles are shown from Nb₃Sn coated niobium, providing a relatively straight forward analysis for concentration as a function of depth. In addition, the sample preparation technique of “angle polishing” was shown as a viable sample preparation technique, which extends reachable profile depths to hundreds of microns. Results from angle polished SIMS analysis showed an increase of bulk nitrogen concentration for 700°C N-doped niobium to be an order of

magnitude higher than cavity raw material, indicating high rates of diffusion and homogeneity of nitrogen in the bulk material when doped at elevated temperatures. The angle polishing technique can be used for both XPS and SIMS sample preparation and is only limited in depth by the ability to polish at a given angle accurately.

5.5 Acknowledgements

- Co-Authored by Jefferson Science Associates, LLC under U.S. DOE Contract No. DE-AC05-06OR23177
- We are grateful for support from the Office of High Energy Physics, U.S. Department of Energy under grant DE-SC0014475 to the College of William & Mary.
- The Institute for Critical Technology and Applied Science (ICTAS), and Nanoscale Characterization and Fabrication Laboratory (NCFL) at Virginia Tech

Appendix B

B.1 XPS for Surface Characterization of Nb₃Sn

XPS survey scans are an overview technique which are collected at relatively low energy resolution and used to quickly identify and quantify the elemental make-up of the surface. Survey scans were used to analyze surfaces of both polycrystalline and single crystalline regions of niobium coated with Nb₃Sn. In this case for the polycrystal and bicrystal coupons it revealed a Nb/Sn atomic ratio of 0.75 and 0.63 respectively, a ratio much richer in Sn than the expected value of 3 for Nb₃Sn. This is not surprising given that tin vapor was present in the furnace during cool-down. Survey scans found only oxygen and adventitious carbon in addition. Chlorine, which is of interest due to use in the nucleation process, was not found on the surface. Figure B. 1 shows a survey scan of a single crystal region of niobium coated with Nb₃Sn.

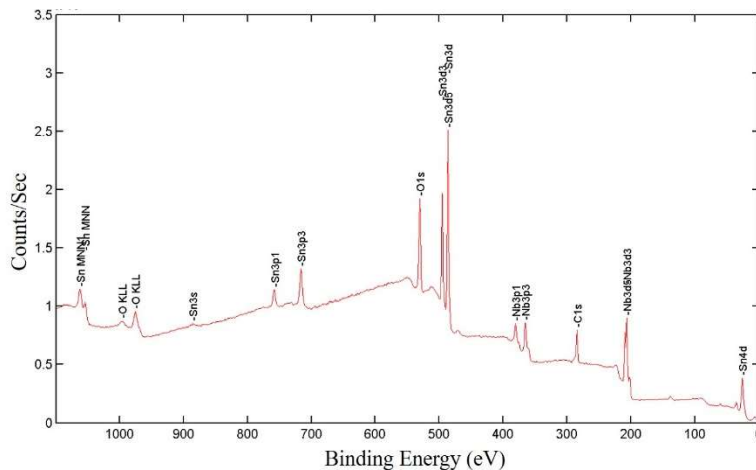


Figure B. 1 XPS survey scan of single crystal region of niobium coated with Nb₃Sn.

While survey scans are particularly useful for elemental identification of an “unknown” surface, it is an incomplete picture. A singularly powerful feature of XPS is its ability to determine chemical state for the topmost surface of a material. This is done through high resolution scans (referring to energy resolution), in which shifts in binding energy due to

local bonding will appear as multiple peaks for a single element. These peaks can be identified, curve fit and quantified. High resolution scans were collected on the Nb₃Sn coated polycrystalline region and curve fit. Figure B. 2 shows the curve fit high resolution scans for the polycrystalline sample.

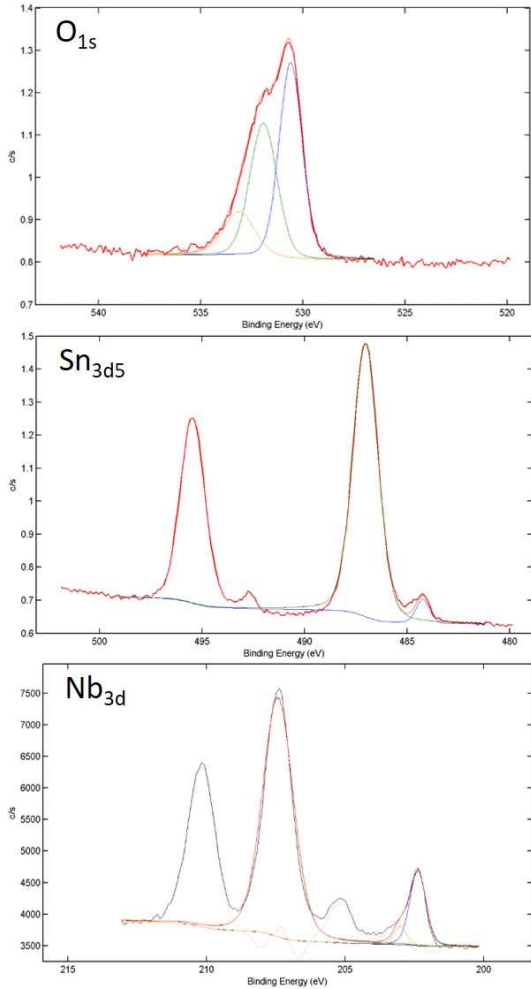


Figure B. 2 High resolution scans of O, Sn, and Nb for Nb₃Sn coated polycrystalline coupon.

In order to curve fit and quantify, we make two assumptions; first that the bulk niobium is fully coated with Nb₃Sn and secondly that all carbon and non-oxide oxygen detected is surface contamination. We then can combine what we learned from the survey scans and high-resolution scans to get a complete picture of the Nb₃Sn polycrystalline surface. Table B. 1 shows the calculated make-up of the Nb₃Sn surface in weight percent and mole fraction. The vast majority of the top-most surface is tin and niobium oxide. As shown in section 5.3.1, the XPS analysis depth for Nb₂O₅ is ~18 nm. With only a small amount of Nb₃Sn visible it seems to indicate an oxide layer with thickness of approximately the same. A small part of the Sn is unaccounted for in the stoichiometry of the three main components. This could be due to a small amount of error inherent to the analysis or an alternate form of Sn present, perhaps SnO or elemental Sn.

Table B. 1 Composition values expressed in weight % and mole fraction calculated for coated polycrystalline niobium.

Molecule	Weight %	Mole Fraction
SnO ₂	58.7	72.1
Nb ₂ O ₅	35.3	24.5
Nb ₃ Sn	5.5	2.6
Sn-unknown	0.5	0.8

B.2 XPS of Anodized Nb₃Sn

Anodization in ammonia solution is a process being researched in order to improve the SRF surface topography after coating. It may be combined with HF rinsing as oxy-polishing in which the HF removes oxide formed during anodization. The present experiments used equal parts of 50% ammonium hydroxide solution and de-ionized water. DC voltages of 10, 20, 30, 40 or 50 volts were applied for sufficient time for current to fall to 10 mA.

XPS is used here to depth profile and investigate thickness of anodization as an effect of varying the applied voltage. Figure B. 3 shows samples used for testing. Anodizing voltage increases from left to right in the image. There were five anodized samples with the leftmost sample being an untreated blank. Color change can be seen in all of the anodized samples with the faintest being the high voltage of 50V.



Figure B. 3 Anodized samples from left to right, Blank, 10V, 20V, 30V, 40V, and 50V.

As mentioned previously, crater measurement for XPS depth calibration can be difficult. In order to determine a more precise sputter rate one sample was cross sectioned and measured using the FIB. The 50V anodized sample was cross sectioned, polished, and measured. Figure B. 4 shows SEM images of the FIB cut cross section along with measurements of the anodized layer. The Pt layer was deposited in the FIB to preserve the oxide thickness during sputtering. The oxide thickness was measured to be 116 (+/- 8) nm.

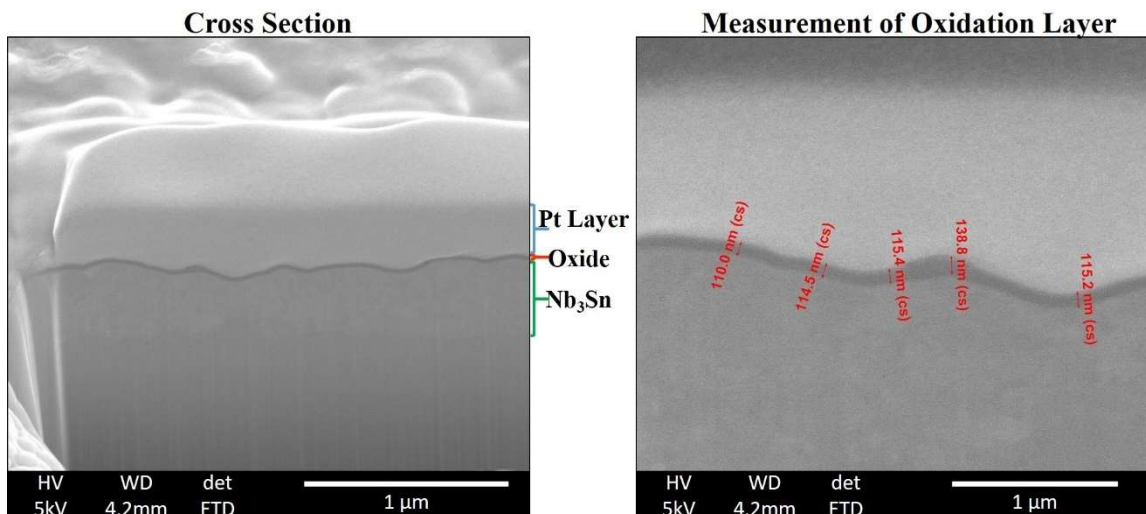


Figure B. 4 FIB cross section with measurements of 50V anodized layer.

Measurement from the cross section was used to calculate a sputter rate and place the XPS depth profiles on a depth scale. The depth profile from the 50V sample can be seen in Figure B. 5. The depth profiles from the complete series of anodized samples can be seen in Figure B. 6. Using the profile data from the oxygen signal, a horizontal intercept was calculated from the FIB data and used to calculate the thickness of oxide on each anodized sample. This was done by placing a vertical line through the 50V sample at 116.4 nm and a horizontal intercept was then extended through the series data. At each intercept a vertical line was used to determine the oxidized layer thickness. The horizontal (solid red line) and vertical (dashed lines) intercept lines along with calculated thicknesses for the anodized series are also shown in Figure B. 6.

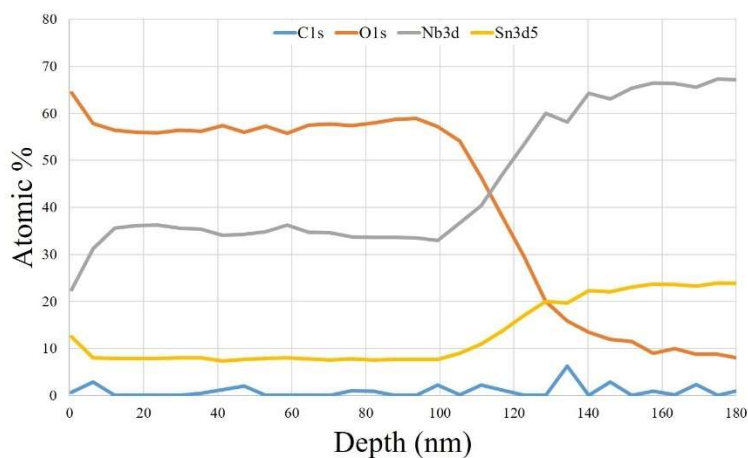


Figure B. 5 XPS depth profile of sample U49 anodized at 50V.

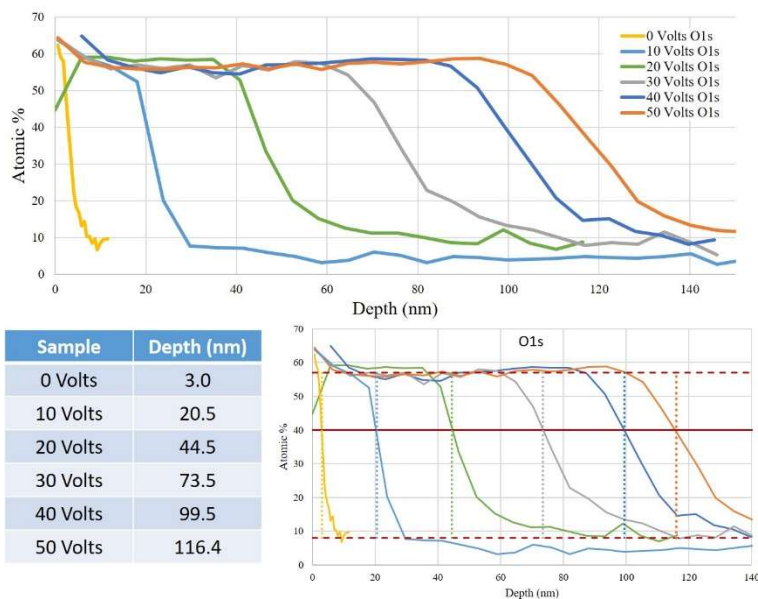


Figure B. 6 Depth profile of oxygen concentration for each of the anodized samples. A FIB cross section of the 50V was used to determine oxide thickness (depth) for each of the samples.

B.3 XPS for Nucleation Study

A series of experiments have been conducted, stopping the Nb_3Sn coating process at different stages during the nucleation and coating steps. One of the initial steps in the Nb_3Sn process is the formation of a seed layer by vaporizing SnCl_2 into the chamber. This seed layer promotes a uniform Nb_3Sn layer to form. XPS was used in this experiment to survey the surface for the presence of any chlorine deposited during the nucleation process. Figure B. 7 shows an example of an XPS survey scan and where chlorine peaks should appear if present. No chlorine was observed on the surface of the nucleation samples, indicating the SnCl_2 cleanly dissociates leaving only tin on the surface to form nucleation sites for the growth of Nb_3Sn . Chlorine was not seen in any of the steps of coating analyzed.

For shorter time higher temperature mid-process samples (e.g. 1 min/1200 °C) a Nb/Sn ratio of 1.5 was found. For longer time lower temperature samples (e.g. 60 min/500 °C) a Nb/Sn ratio of 2.71 was found. This seems to suggest with longer time comes a surface not only more completely covered by tin but closer to a 3/1 ratio indicating a surface fully coated by Nb_3Sn . It also seems to indicate the slow cooling of the full coating process may be responsible for the extensive oxide coverage found in Appendix 5A. High resolution XPS similar to the analyses in appendix 5A could be used to further explore the nucleation and coating process, but was unnecessary for the question at the moment concerned with the presence of chlorine.

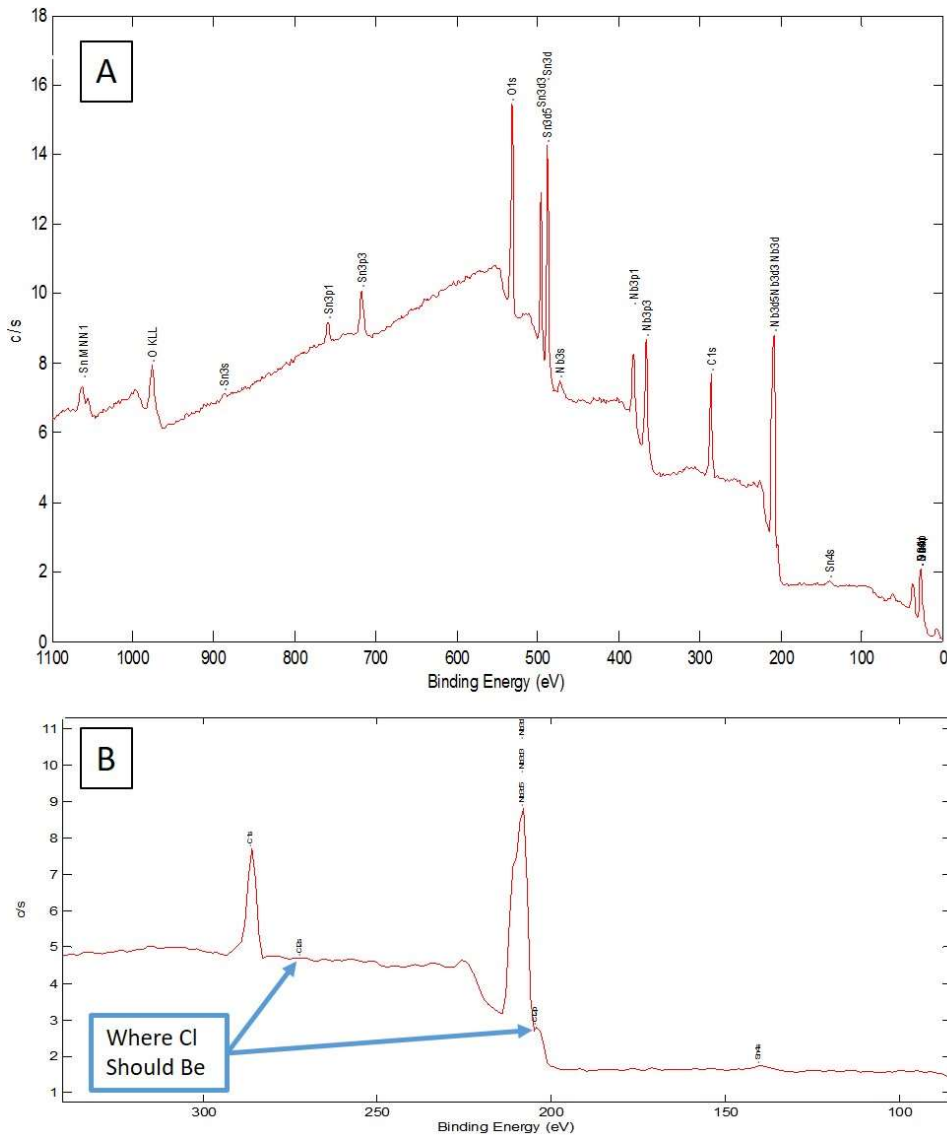


Figure B. 7 XPS survey scan (A) of niobium surface stopped early in the Nb₃Sn coating process. Figure B. 7B shows where Cl peaks would appear if Cl was present.

B.4 EDS Cross-Section Analysis as an Alternative to XPS Depth Profile

As previously mentioned (5.3.4) the polycrystalline nature of the Nb₃Sn coating produces error during depth profile measurements. An uneven interface and preferential sputtering due to crystal orientation lead to a decrease in depth resolution. In addition, preferential sputtering of tin causes error in quantification. In order to verify quantification and minimize error due to sputtering, EDS was used to analyze the cross-section of niobium coated with Nb₃Sn. While cross-sections were still prepared by ion sputtering, the damage produced and effect seen in data are expected to be much less. TRIM calculations estimate the XPS sputter (Ar, 5 kV, 45°) ion distribution and damage depth to be limited to ~10 nm, while the FIB final surface polish (Ga, 2 kV, ~89°) is ~3 nm. XPS sampling depth is ~10 nm while EDS sample depth is ~1 μm. This means sputtering artifacts will have a large impact on XPS analysis and virtually no impact on EDS.

The niobium coupon analyzed was coated for a total of 78 hrs, resulting in a thick layer (~13 μm) appropriate for analysis with EDS's lateral resolution of ~1 μm . The Nb_3Sn cross-section was prepared using FIB. FIB preparation is discussed in further detail in section 6.2.2.7. FIB cross-sections and EDS line-scans were performed via an FEI NanoLab 600 dual beam, which is equipped with an integrated Octane Elite EDS with 25 mm^2 detector. Data processing was performed using EDAX analysis and NIH ImageJ software.

Figure B. 8A shows the cross-section used here. The section consists of a platinum protective layer, Nb_3Sn coating, and bulk niobium. The cross-section represents ~100 μm of coating. Coating thickness was found to be 13.4 (± 1.4) μm with a min of 10.9 μm and max of 15.9 μm . Point analyses for Nb_3Sn and the niobium bulk are represented by P1 and P2 in Figure B. 8A. Spectra for both show 10-20 at% oxygen and small amounts (~1 at%) of titanium, iron, and nickel. Assuming the oxygen detected is surface oxide and the titanium, iron, and nickel are trace contaminants, they are removed from the quantification. For the Nb_3Sn coating this results in a concentration of 76.7 at% niobium and 23.3 at% tin or a ratio of 3.3 Nb/Sn. Figure B. 9 shows the EDS spectrum from point "P1" shown in Figure B. 8A.

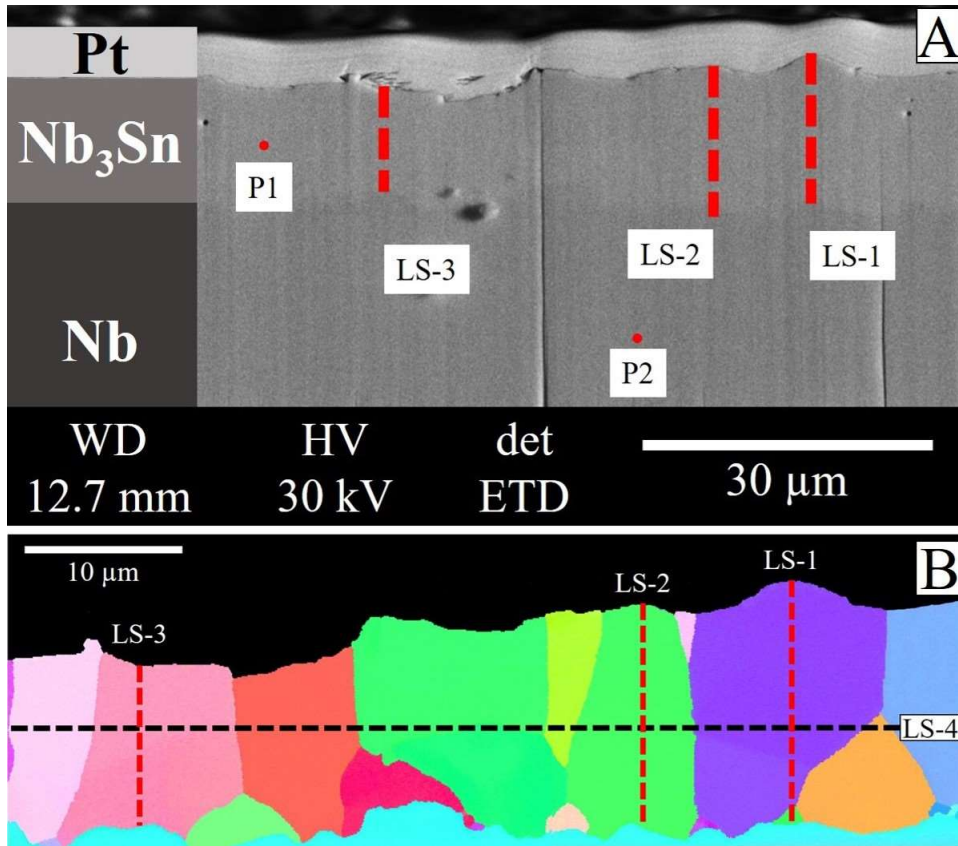


Figure B. 8 (A) Image showing FIB cross section of 78 hr Nb_3Sn coating. The dashed lines LS-1, LS-2, and LS-3 represent the approximate locations of line-scans. Points P1 and P2 show the approximate location and spot size for the point analyses of Nb_3Sn and bulk niobium. (B) EBSD map of corresponding Nb_3Sn layer. EDS line scans are marked with dashed lines.

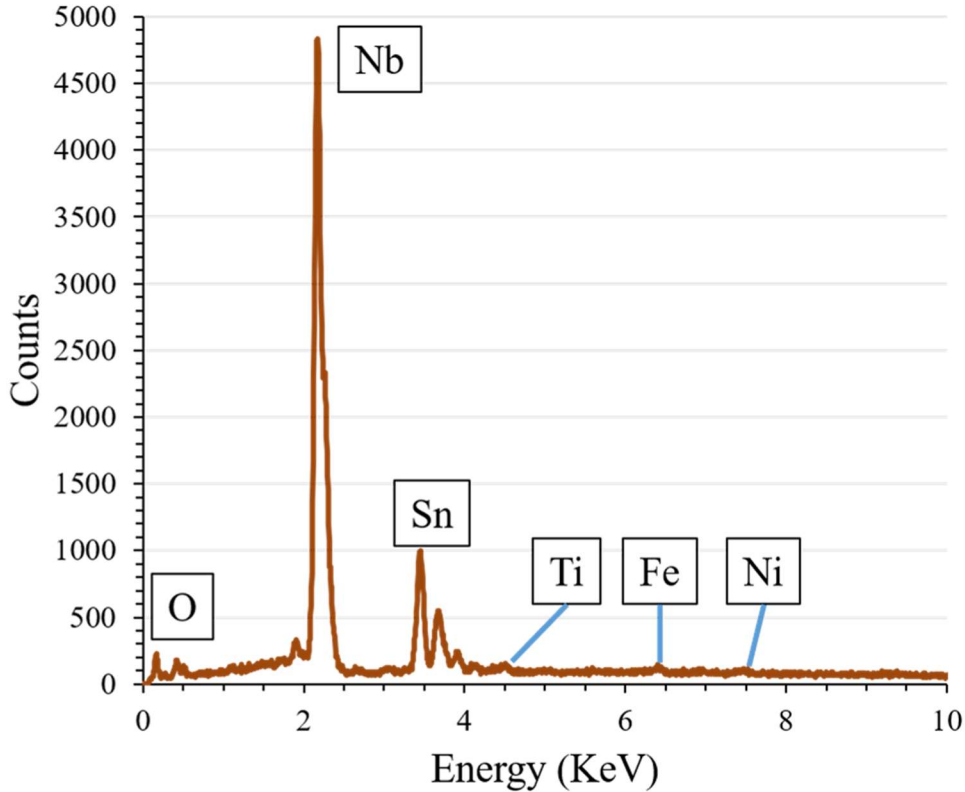


Figure B. 9 EDS spectrum from Nb₃Sn coating grown for 78 hrs. Analysis placement is shown in Figure B. 8A as “P1”.

EDS line scans were performed in order to investigate tin concentration change as a function of layer depth. The vertical line scans were centered in large grains. The placement can be seen in Figure B. 8A and B marked with red dashed lines and labelled LS-1, LS-2, and LS-3. The quantified values of niobium and tin from the three vertical line scans can be seen in Figure B. 10. Three different grain orientations were analyzed and show matching concentrations of niobium and tin. Interestingly a gradual decrease in tin concentration is seen as the scan progresses towards the interface. For example, in the LS-3 scan, tin concentration drops from 17.6 (± 0.6) at% near the surface to 14.6 (± 0.7) at% at a depth of $\sim 10.5 \mu\text{m}$. This tin gradient and the fact there is not detected tin in the bulk niobium is in agreement with the growth mechanism and tin availability at the interface being the limiting factor in growth rate.

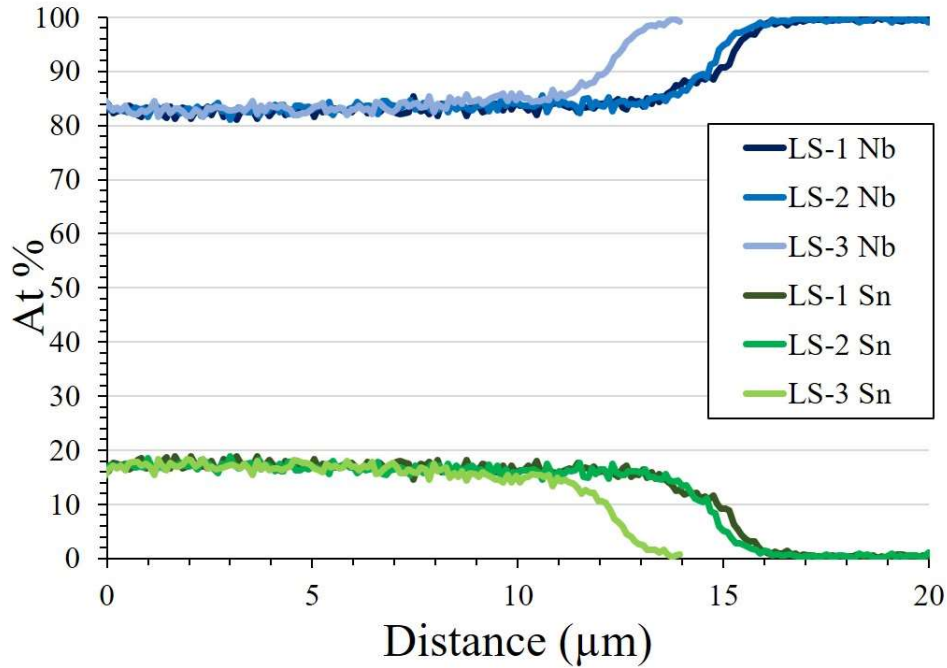


Figure B. 10 Vertical line scans of Nb₃Sn coating. A slight decrease in tin concentration can be seen from the top to bottom of the Nb₃Sn layer. Positioning of line scans can be seen in Figure B. 8.

In order to further differentiate any effect orientation may have on tin concentration a line scan was performed parallel to the surface, centered in the Nb₃Sn coating. Placement of the analysis is shown by a black dashed line (LS-4) in Figure B. 8B. Quantified niobium and tin results can be seen in Figure B. 11. Values for niobium and tin were found to be 82.9 and 17.1 at% with a standard deviation of ~1% across the 75 μm scan region. No obvious variation was seen.

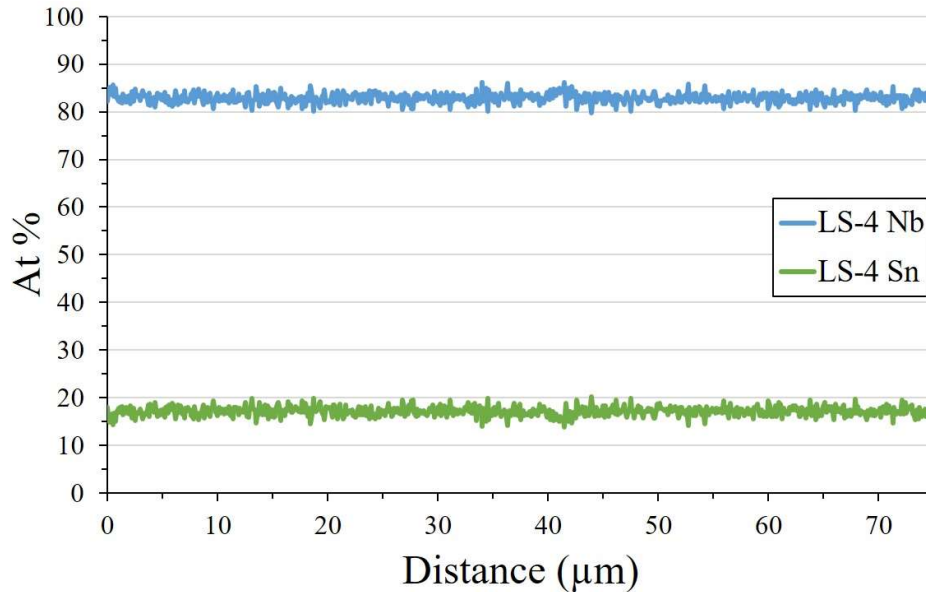


Figure B. 11 EDS line scan placed parallel to the surface, through the center of the Nb₃Sn coating. For placement of analysis see black dashed line in Figure B. 8B.

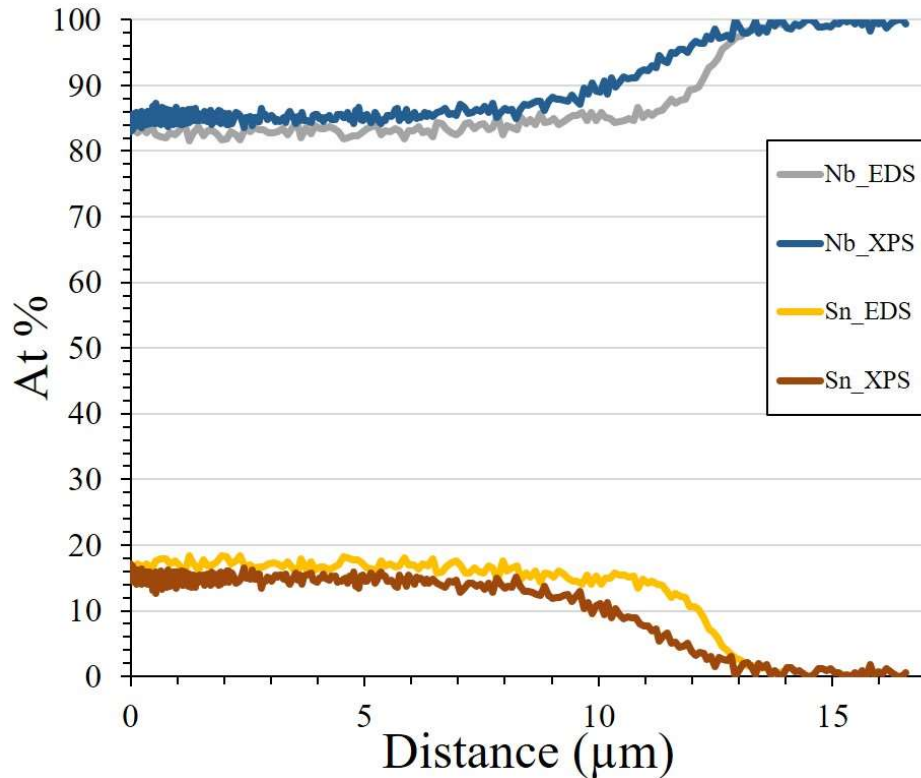


Figure B. 12 Plot of EDS line scan LS-3 and XPS depth profile from the same niobium coupon coated with Nb_3Sn for 78 hrs.

In Figure B. 12 a direct comparison is made between EDS line scan and XPS depth profile data. EDS data shows a much sharper transition at the interface normally indicative of higher depth resolution. The more gradual slope seen in the XPS depth profile is due to preferential sputtering and an uneven interface as previously mentioned. XPS has a much larger spot size ($200\ \mu\text{m}$ vs $1\ \mu\text{m}$ in this case) meaning the data reflects an average of a much larger area as it passes through the interface. Nb/Sn ratio's for Nb_3Sn have been reported from 2.7 to 4.3 or 19-27 at% Sn. [73] The discrepancy in quantified niobium to tin ratio from the expected stoichiometric value seen in the XPS depth profile (5.0 Nb/Sn) can be explained by the preferential sputtering of tin. However, this does not explain the discrepancy in the EDS line scan data (4.9 Nb/Sn), especially taking into consideration EDS point analysis data reported above shows a ratio of 3.3 Nb/Sn.

In summary, in appropriate cases EDS analysis of Nb_3Sn coating cross-sections proves to be a viable and possibly preferred technique to XPS depth profiles. XPS has the advantage of being able to resolve much thinner coatings and the statistical advantage of a much larger analysis area. For thicker coatings the slow sputtering of XPS becomes less favourable and the time required for FIB prepared cross sections for EDS analysis logistically practical. The combination of SEM, EDS, and EBSD (commonly found on the same instrument) also provides information unavailable by any other single technique.

Chapter 6

6 Electron Backscatter Diffraction of Nb₃Sn Coated Niobium: Revealing Structure as a Function of Depth

Over the last two decades, advances in Electron Backscatter Diffraction (EBSD) have moved the technique from a research tool to an essential characterization technique in many fields of material research. EBSD is the best suited technique for determining structure as a function of depth. This characterization is critically important, but has been previously absent from Nb₃Sn efforts. While EBSD is the technique of choice, obtaining quality data can be difficult. Sample preparation in particular is non-trivial. Here we summarize the general principles of EBSD, discuss specific sample preparation techniques for Nb₃Sn coated SRF cavity material, and give examples of how EBSD is being used to understand fundamental growth mechanisms for Nb₃Sn coatings.

6.1 Introduction

6.1.1 Motivation for Work with SRF Materials

High energy particle accelerators are an invaluable tool in the effort to expand the frontier of science and in order to expand further, more powerful accelerators must be constructed. Currently, the base technology for these high energy research accelerators utilizes solid niobium superconducting radio frequency (SRF) resonating cavities. The construction and operational cost of the cryogenics plants required can make new more powerful accelerators prohibitively expensive. In order to push accelerators further the cost of cryogenics must be reduced. From a materials perspective, one of the leading next generation technologies is the development of a well understood and robust Nb₃Sn coating process. Nb₃Sn coated cavities have several advantages over solid niobium cavities, including a higher critical temperature and a theoretically higher accelerating gradient. This would allow for warmer (4.2 K vs 2 K) accelerator operation and physically smaller accelerators, both of which positively affect build and operational costs.

It has been more than 40 years since accelerator science researchers started exploring Nb₃Sn as an alternative to solid niobium cavities. [36] However, there still is not full understanding of the coating and growth process, how this affects material structure, or translates to cavity performance. Secondary ion mass spectrometry (SIMS) has proved the technique of choice for analysis of composition as a function of depth for SRF cavity materials. [74] However, in addition to elemental composition, it is necessary to reveal the materials structure over meaningful depths. In the case of current coatings this can range from near surface to 5 μm or more in depth. For this size scale, EBSD is suited better than any other instrumentation available. Here, we will provide an overview of the technique, sample preparation methods specific for SRF cavity materials and example data from Nb₃Sn coating experiments and investigations.

6.1.2 Electron Backscatter Diffraction

EBSD is a fairly young technique, with the first fully automated commercial systems becoming available in the mid 1990's. [75] The technique quickly progressed and showed exponential growth in literature as instruments became available in the early 2000's. [76] Today it is often the technique of choice for microstructural analysis of crystalline materials. Grain size and shape, misorientation between and within grains, phase content, defects, and texture results such as inverse pole figures can be obtained from a single analysis. In addition, if installed as an integrated Energy Dispersive Spectroscopy (EDS) and EBSD system as the instrument employed here, data can be combined with elemental information. Commonly a Focused Ion Beam (FIB) is also added to the same platform.

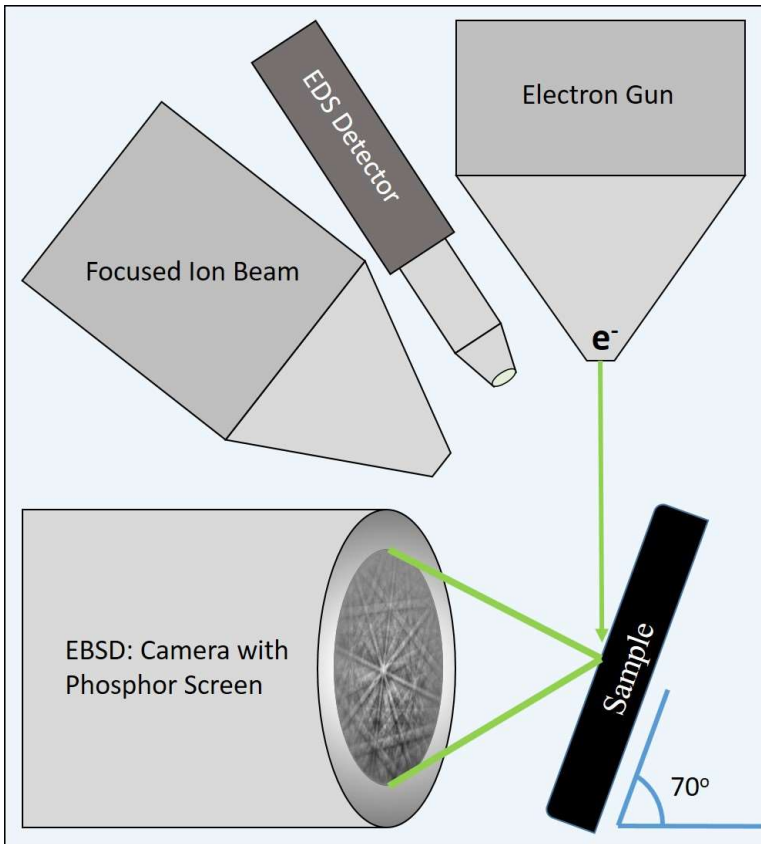


Figure 6.1 Configuration of dual beam microscope equipped with EDS, EBSD, and FIB.

EBSD instrumentation is an addition to a scanning electron microscope (SEM). The main hardware component of the EBSD system is a phosphor screen and charge-coupled device (CCD) configured as illustrated in Figure 6.1. The sample is mounted tilted towards the phosphor screen at an angle that creates an e^- incidence angle of $\sim 20^\circ$. This geometry is suitable to observe diffraction patterns and maximizes the number of backscattered electrons able to escape the sample surface.

Bragg's law describes the process, shown schematically in Figure 6.2. Electrons scatter in all directions from within the interaction volume. Figure 6.2 shows the path of one scattered electron is $2d \sin \theta$ longer than the other, making them out of phase. These path differences lead to constructive and destructive interference. [77] A fraction of the electrons satisfy Bragg's equation by scattering at an appropriate angle (θ). This is the condition for

constructive interference, creating high intensity cones of electrons, Kossel cones, to form. Where the Kossel cones intersect the phosphor screen, Kikuchi lines and a lattice specific diffraction pattern (Kikuchi pattern) are formed. Figure 6.3 shows a Kikuchi pattern collected from niobium bulk material.

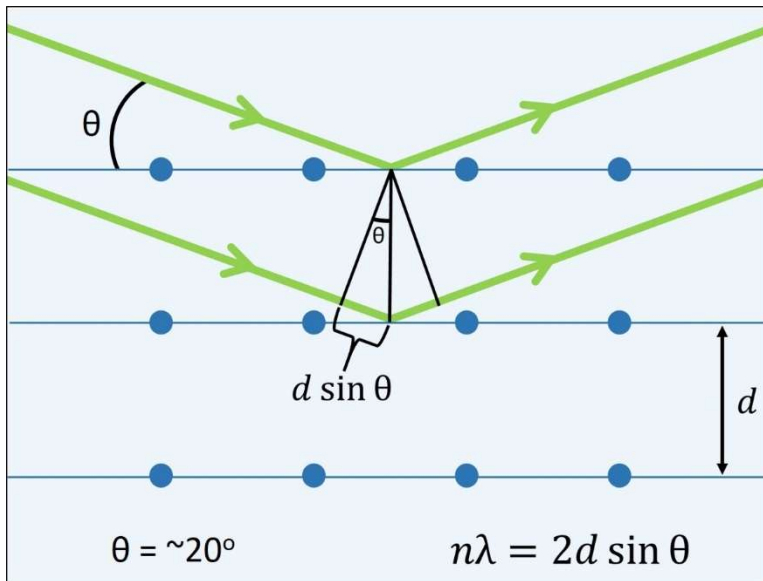


Figure 6.2 Schematic showing diffraction from crystal planes and indicating geometry involved in Bragg's equation.

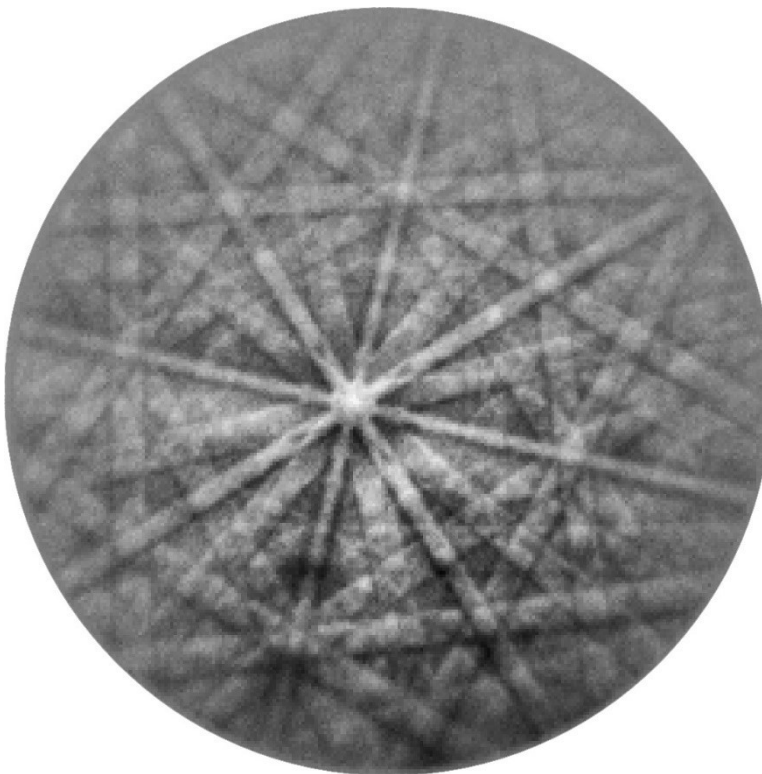


Figure 6.3 Kikuchi pattern collected from bulk niobium after vibratory polishing.

The diffraction pattern formed is a 2D trace of the materials lattice structure, with the width of the Kikuchi bands corresponding to the lattice spacing. The patterns can therefore be used to determine the material's phase and orientation, or "indexed". The rate of indexing patterns has impressively increased to above 1,000 frames per second for commonly available instrumentation or higher for state-of-the-art instrumentation. [78, 79, 80] This has moved map collection from hours/map to maps/hour, making for a logistically favorable characterization technique.

6.2 Experimental

6.2.1 Materials

Unless otherwise stated, samples were 10 mm square coupons cut by electrical discharge machining from trimmings of the 3 mm thick niobium sheet used to make SRF cavities ("RRR grade"). Typical grain size for polycrystalline material is in the 50 μm to 100 μm range in the un-annealed state. All were subjected to buffered chemical polishing (BCP) using a solution of 49% HF, 70% HNO₃ and 85% H₃PO₄ in the ratio of 1:1:1 by volume with minimum removal of 50 μm . These samples further received metallographic polishing, also known as nanopolishing (NP) [55], which typically removes > 100 μm and produces surface roughness on the order of a few nanometers. [61] Nb₃Sn coatings were prepared using the vapor deposition process. Several examples include coatings grown on niobium which was anodized prior to the coating. For in-depth discussion of the Nb₃Sn vapor deposition setup, process, and anodization refer to reference [63].

6.2.2 Electron Backscatter Diffraction

EBS D was performed via FEI NanoLab 600 dual beam, which is equipped with an integrated EDS/EBS D collection system, including an EDAX TSL EBS D camera and Octane Elite EDS with 25 mm² detector. Data processing was performed using EDAX OIM Analysis and NIH ImageJ software.

6.2.2.1 Analysis Conditions

There is no universal "best" EBS D condition and parameters for analysis are dependent upon material type and the goals of the analysis. [81] Typical EBS D conditions range in beam voltages from 10-30 kV and beam currents of 1-50 nA at ~20° incidence angle. [82, 77] Optimal conditions for pattern indexing of Nb₃Sn with a 2 kV surface polish (see section 6.2.2.7) were found to be 30 kV and 5.5 nA with an incidence angle of ~14°. This lower incidence angle increases interaction volume while decreasing depth, which reduces lateral resolution, but helps to increase the signal to noise ratio. Depending on the quality of the surface it may be necessary to raise the electron beam current in order to increase the signal to noise ratio and help with indexing quality. Beam currents up to 21 nA (the maximum current for the particular instrument) were used successfully with acceptable lateral resolution.

6.2.2.2 Data Density

When collecting orientation maps that will be used for quantitative analysis, such as grain size, it is important to consider beam raster step size. While smaller step size (higher resolution) images in theory produce more accurate results, this is not always the case or

logistically possible when analyzing real world samples. As step size gets smaller the number of data points and subsequently the time required for analysis goes up exponentially. Longer collection times can cause error from both physical drift and drift caused by charging. Longer collection times also lead to more contamination in the form of carbon buildup on the sample surface, causing weaker signal and indexing issues. [83] Choosing the largest acceptable step size which will clearly describe the sample is recommended. For relatively simple quantification, such as average grain size, 8-10 steps (~100 points) per grain are recommended [84, 81, 76]. More intricate characterization, such as interface, defect, or precipitate characterization will necessitate lower step sizes. When performing investigatory work on samples of unknown feature size, smaller step sizes are necessary to insure features of importance are not left unresolved. Typical step sizes for analysis here range from approximately 0.02 μm to 1.0 μm , depending on the size of the map and detail needed.

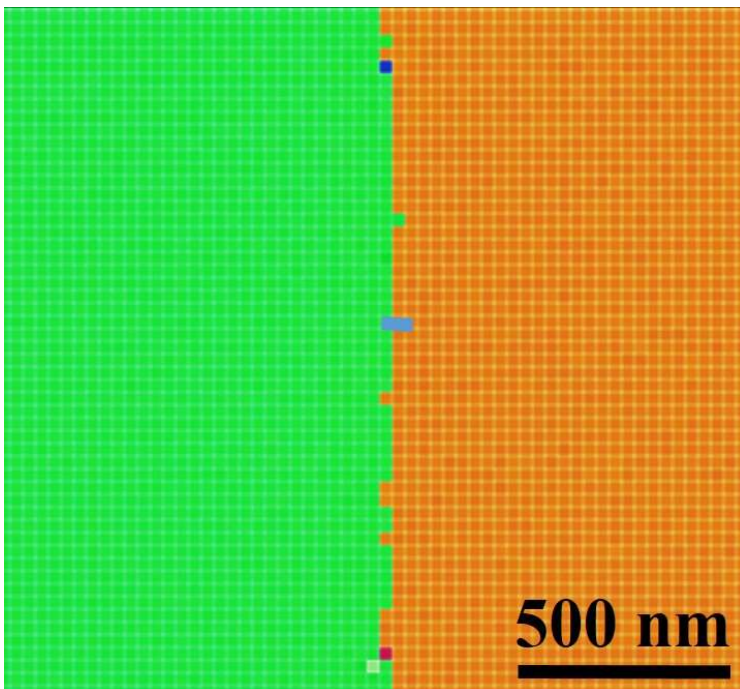


Figure 6.4 Magnified grain boundary from bulk niobium in Figure 6.5B, each pixel represents a 30 nm step.

6.2.2.3 Lateral Resolution

Lateral resolution can vary greatly, depending on microscope type (field emission sourced microscopes result in smaller values than a tungsten source), primary beam energy (higher energies result in higher values), material (higher density materials result in lower values), and collection parameters (step size). Ultimate lateral resolution is commonly reported to range from 5-200 nm. [82, 77, 85, 76] Effective resolution is dependent upon the software system's ability to deconvolute overlapping patterns of neighboring volumes [85]. The effective resolution can be calculated using the fraction of indexed to non-indexed points (see Ref. [84] for details). Here, because EDS was used in conjunction to aid indexing and only two phases were present, indexing is close to 100%, resulting in calculated resolutions of ~ 0 nm. In this case the effective resolution can be estimated from the smoothness of the grain boundaries. [86] Figure 6.4 shows a magnified grain boundary from Figure 6.5B,

where the mapping step size, i.e. pixel size, is 30 nm. Based on this, the effective resolution for Figure 6.5B is estimated at 60 nm.

6.2.2.4 Data Cleaning

Kikuchi patterns collected are not necessarily of high enough quality/contrast to be indexed well. This results in either non-indexed or incorrectly indexed points. Non-indexed points will appear as black pixels in a map. A large number of non-indexed points can be seen in both Figure 6.5A and Figure 6.12B. Incorrectly indexed points rarely form in cubic metals (incorrect indexing is more common in low-symmetry materials) and appear as isolated, highly misoriented pixels. [84] Several incorrectly indexed points can be seen along the grain boundary in Figure 6.4. If a sufficient number of data points are not indexed or mis-indexed cleaning steps can be performed to remove erroneous points. There are many algorithms (nearest neighbor, average orientation, minimum/maximum grain size, misorientation, etc) included with most analysis software in order to facilitate easy cleaning of data. Care must be taken in using data cleaning and it should be used lightly as to not misrepresent the data collected. Samples such as Nb₃Sn coatings are good candidates for a “light” cleaning as sample preparation can be quite difficult and time consuming. For example, a common problem with Nb₃Sn coating preparation is contamination with niobium which has been redeposited from the bulk material. This can be very difficult or logistically not feasible to completely eliminate. In this study, cleaning was applied using either grain size limits, a single phase per grain filter, grain dilation, or combination of the three. The goal is to clean without distorting the results by only replacing a small percentage of the total data collected. Cleaning steps were limited to replacing ~10% or less of the displayed data in order to preserve the integrity of the analysis.

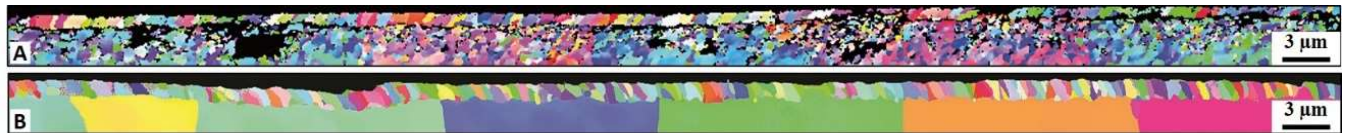


Figure 6.5 Two examples of EBSD cross sections (approximately 85 μm in length). Figure 6.5A shows a nonpolished sample, while Figure 6.5B shows a cross section prepared by diffuse ion beam.

6.2.2.5 Sample Preparation

Similar to lateral resolution, information depth varies widely with accelerating voltage, material density, etc. Information depth in silicon has been shown to be less than 40 nm, dropping to ~10 nm for the heavier element Ni at 20 kV. [86] With comparable accelerating voltages information depths of 10 nm or less can be expected for niobium and Nb₃Sn. When working with such shallow depths of information, the selection and implementation of sample preparation method are of high consequence. Sample preparation consumes the vast majority of the time required for method development and work required in the performance of EBSD. Because of the shallow information depth of the technique the surface must be free from contamination and residual deformation. Any significant amount of amorphous surface layer, such as deformation from mechanical preparation, surface oxides from exposure to atmosphere, or surface contamination as a result of beam interaction can degrade or prevent observation of diffraction patterns. It has been reported as little as 3 nm of amorphous material will cause pattern degradation. [83]

Metal specimens prepared with normal metallographic techniques require further polishing to reduce the deformation layer. [75] Typically, vibratory polish with a colloidal silica suspension in the size range of 0.02 μm is sufficient for a final polish. Nb_3Sn coated niobium cross sections prove particularly difficult due to the soft nature of niobium, hardness difference between niobium and Nb_3Sn , and edge retention needed at both the $\text{Nb}_3\text{Sn}/\text{Nb}$ interface and Nb_3Sn surface. It was found prohibitively difficult and impractical to achieve EBSD results by mechanical only polishing. Cross section samples were sent for professional metallographic polishing using a proprietary technique referred to as “nanopolishing” (NP). [55] NP samples have been used for coating experiments and SIMS analysis previous with great success and found well suited for characterization experiments. [11, 87, 59] EBSD results from a NP cross section are shown in Figure 6.5A. While the NP polished sample provided the first published EBSD results for Nb_3Sn coated SRF cavity niobium, there are issues which needed to be resolved. [88] The first issue is that the bulk niobium is known to be relatively large grain ($\sim 10\text{-}100\ \mu\text{m}$) material. However, Figure 6.5A shows each niobium grain made up of many ($<1\ \mu\text{m}$) micro-grains. In addition, large patches of data failed to index and are missing in both the niobium and Nb_3Sn phases of the map. Maybe most importantly there is no indexed data found at the $\text{Nb}_3\text{Sn}/\text{Nb}$ interface. These problems are attributed to damage and topography caused by the NP technique.

Sample preparation issues were resolved by combining an initial mechanical polish with a final polish via ion beam. During ion polishing, ions (Ar and Ga for this work) are accelerated towards the sample with sufficient energy to remove material from the surface. Care must be taken when choosing polishing parameters. High impact energies and angles can lead to thick damage layers, while high currents can lead to sample heating. Properly implemented ion beam techniques were found to perform well, giving high quality surfaces excellent for EBSD analysis. Both diffuse ion beam and focused ion beam (FIB) techniques were utilized with great success.

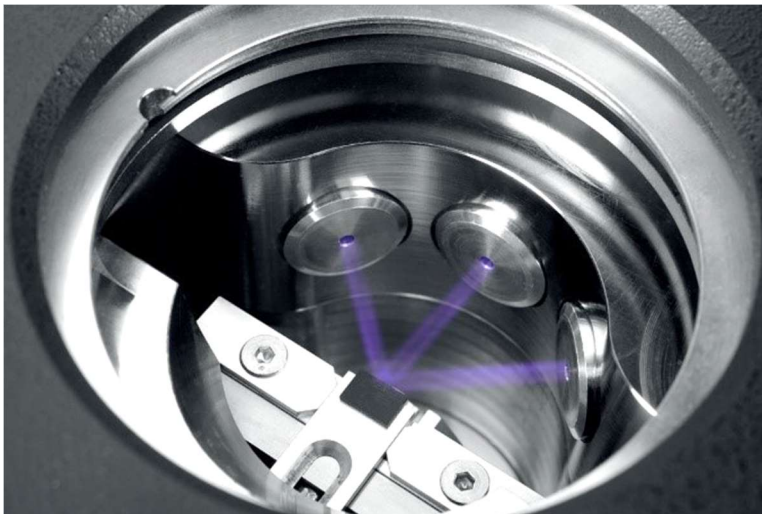


Figure 6.6 Leica TIC 3x sample chamber with triple argon ion beams. Sample location is at beam convergence point.

6.2.2.6 Diffuse Ion Beam Polishing

Diffuse ion beam polishing was accomplished via a Leica EM TIC 3x milling system. The TIC 3x makes use of three loosely focused argon ion guns in order to polish a relatively large area. The TIC 3x sample chamber with three argon ion beams can be seen in Figure 6.6.

Since the ion beams are diffuse in nature, care must be taken mounting and masking the sample in a way to protect the surface and uniformly sputter material away over the area of interest. Normally masking the surface is a straightforward process involving the placement of the sample surface up to a tungsten carbide mask placed perpendicular to the beam path. Anything above the mask will be removed, leaving an ion polished cross-section. This standard mounting can be seen in Figure 6.7A. In the case of Nb_3Sn , the natural roughness of the surface was found to prevent the mask from making a proper fit (Figure 6.7B), resulting in turbulent argon flow, failing to protect the surface, and leaving a large amount of topography through the Nb_3Sn layer. Several mounting geometries and embedding techniques were tested and the following technique was found to produce the highest quality results. Two small pieces of the sample were glued surface to surface using M-Bond 610 adhesive. A small clamping vise was used in order to insure square bonding with a minimal amount of glue between samples, thus creating a sandwich with the area of interest in the middle. The sample was then mounted with the surface junction parallel to the beam direction. The sample face closest to the beam was mechanically polished before mounting in order to ensure a tight square fit to the tungsten carbide mask. (Figure 6.7C)

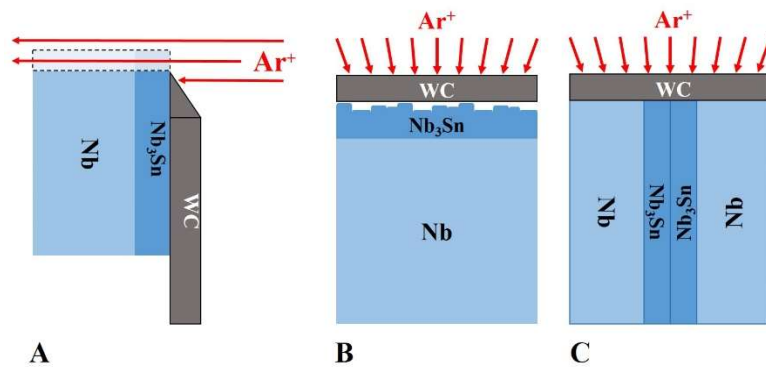


Figure 6.7 Sample mounting for Leica TIC 3x. A.) Cross-section view showing tungsten carbide (WC) mask with standard mounting. B.) Top down view of standard mounting, showing gaps due to rough Nb_3Sn surface. C.) Top down view of sandwich method for mounting.

With ion beam techniques the main determinants of damage depth are accelerating voltage and incidence angle. Best results were found with incidence angles $<10^\circ$ and by working stepwise from 10 kV down to ≤ 3 kV. Stepping down the accelerating voltage has the same effect as moving from lower to higher grit sandpaper, successively removing less material and causing less damage with each step. Eventually only a few nm's of damage remain; less than ~ 3 nm under the above conditions. [54] Using these conditions and the sandwich mounting technique, two (left and right side) samples are created, with EBSD quality areas of several hundred microns in length. Figure 6.5B shows an example of an ion beam polished cross section. The ion beam polished sample shows none of the issues the NP

sample did. Large single orientation grains can be seen in the bulk niobium, while the Nb_3Sn layer and interface region are well indexed.

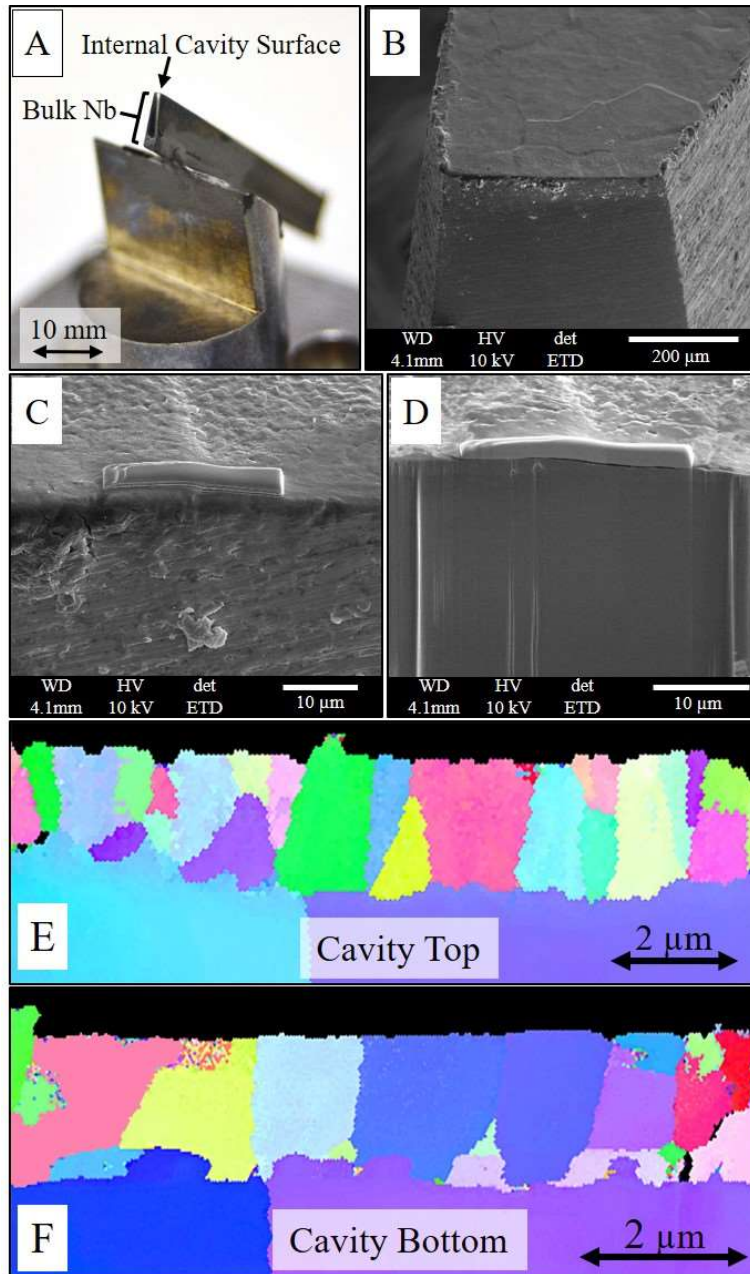


Figure 6.8 (A) Cavity cut-out specimen mounted to SEM stub ready for FIB cross-sectioning and polish (B-D). Example orientation maps from FIB preparation of cavity cut-out specimens (E-F).

6.2.2.7 Focused Ion Beam Polishing

While diffuse ion polishing via the TIC 3x creates EBSD quality surfaces, sample size and shape are limited and special care has to be taken in sample mounting for even regularly shaped coupons. Sample mounting becomes quite difficult with anything outside of the simplest geometries. For samples with unique geometries or where preparation of specific

areas, such as defects, is required, Focused Ion Beam (FIB) becomes the preferred preparation method.

FIB was accomplished with a FEI NanoLab 600 dual beam instrument. The NanoLab makes use of a FIB with Ga source capable of 1-30 kV, with a maximum of 21 nA of current. The general layout can be seen in Figure 6.1. It is quite convenient to have the EBSD system mounted to the dual beam instrument, allowing for final polish and cleaning steps in situ as needed.

While FIB preparation of cross sections yields smaller cross sections and is more complicated in nature than preparation by the TIC 3x, the quality of analysis surface is unsurpassed. Cavity cutouts (segments cut from a wall of an SRF Cavity) are a geometrically complicated example, with compound curved surfaces that can be convex or concave. In addition, cavity cutouts are often small in size. Figure 6.8A shows an example of a small cavity cutout with less than 1 mm of cavity surface available for analysis. The specimen is mounted and electrically grounded appropriately to a 45° SEM specimen mount. The 45° mounting simplifies moving between ion milling and EBSD analysis positions in the FEI system.

For FIB preparation, a cross section should be initially mechanically polished. Starting with a well-polished cross section makes FIB polishing much more efficient and practical, as FIB removes relatively small amounts of material at low rates. When possible, sample faces were polished at a slight negative angle (~3°), leaving less bulk niobium to be removed by FIB. In order to preserve the surface of the Nb₃Sn and create an intact cross section, a protective layer of platinum is deposited on the sample surface over the cross section's area of interest. Figure 6.8B and Figure 6.8C show SEM images of the cavity specimen, before and after a Pt layer is placed on an area of interest, in this case a niobium grain boundary. Once the Nb₃Sn surface is protected, a similar approach is taken as with TIC polishing, stepping down through accelerating voltages and beam currents, removing smaller and smaller amounts of material, while subsequently causing less damage, until left with a smooth EBSD quality cross section. (Figure 6.8D) Initial material removal steps are performed at the highest removal rate of 30 kV / 21 nA. With a low incidence angle (~1°) and 30 kV accelerating voltage, a damage layer approximately 10 nm in depth is formed. [54] The sample is then rotated and final polishing is performed perpendicular to the cross-sectioned surface. First at 5 kV, followed by 2 kV, at ~90° incidence leaving a damage layer of 3-5 nm. Optimal patterns have only been collected after a 2 kV final polish

6.3 Results and Discussion

Provided here are qualitative and quantitative examples and brief discussion of how the EBSD technique helps gain a fundamental understanding of the Nb₃Sn coating process. The examples are meant to be illustrative of how EBSD may be applied to real world sample sets. For in-depth discussion of coating mechanism, structure and composition please see U. Pudasaini et al.

6.3.1 Coating Dependence on Cavity Geometry

The homogenous coating of SRF cavities presents a challenge due to the inherently complicated shape. In order to optimize the coating process data is needed not just from

witness samples, but from processed cavities. Figure 6.8E and Figure 6.8F show example orientation maps from FIB prepared cavity cutouts obtained from different locations in a coated cavity. Analyses such as these can be used to directly determine geometry specific coating issues for large complex SRF cavity shapes. [89] In this case, while the average grain area was not found to be statistically different between “Top” and “Bottom”, $1.4(\pm 0.4) \mu\text{m}$ and $1.6(\pm 0.6) \mu\text{m}$ respectively, a more bimodal distribution in grain size was seen in the “Top” sample.

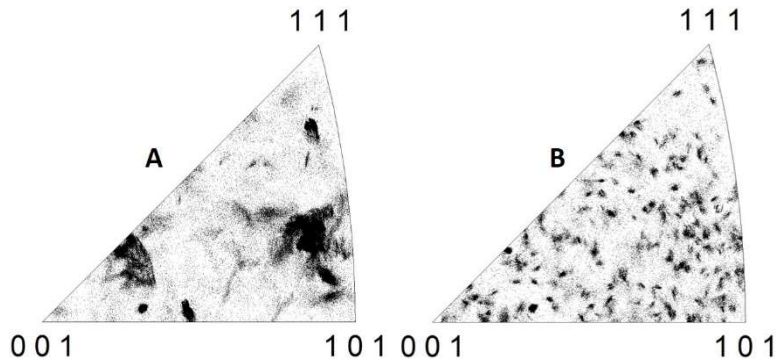


Figure 6.9 IPF of niobium bulk material (A) and the Nb_3Sn coating (B) derived from data in Figure 6.5B.

6.3.2 Orientation Dependence of Nb_3Sn

One of the open-ended questions at the time of this work was whether Nb_3Sn coatings showed substrate orientation-based preferences. Large cross sections like that shown in Figure 6.5B provide a direct answer through inverse pole figures. An inverse pole figure is a simplified way of exposing preferred crystal orientation or texture based on the stereographic projection. Figure 6.9 shows two inverse pole figures (IPF) from Figure 6.5B, Figure 6.9A of the niobium bulk material and Figure 6.9B of the Nb_3Sn coating. There are approximately six distinct orientations shown in the IPF for the niobium bulk material, consistent with what is seen in Figure 6.5B. Figure 6.9B shows many orientations and no preferred crystal orientation for the Nb_3Sn coating over the same region. IPF data has been collected over many cross sections of both polycrystalline and single crystalline niobium, which had been coated with Nb_3Sn . In no case was a correlation seen between bulk material and coating crystal orientation.

Orientation data can also be used to calculate the misorientation or rotation angle between grains. Figure 6.10A shows an example map of grain boundary misorientation for an Nb_3Sn coated niobium coupon. The color of the lines located along grain boundaries represents the rotation angle between grains. Due to the symmetry in a cubic lattice no two grains can differ by more than $\sim 62.8^\circ$. The legend found in Figure 6.10B lists binned rotation angles and their corresponding line color up to 63° . Rotation angles were measured across the Nb/ Nb_3Sn interface for ~ 250 grains from six specimens coated using various times and temperatures. Results are shown via histogram in Figure 6.10C. Nb_3Sn coatings appear to show no specific crystalline orientation via IPF based on bulk niobium crystalline orientation. However, misorientation data shows a preferential rotation angle of $\sim 50^\circ$ for Nb_3Sn grains formed at the interface.

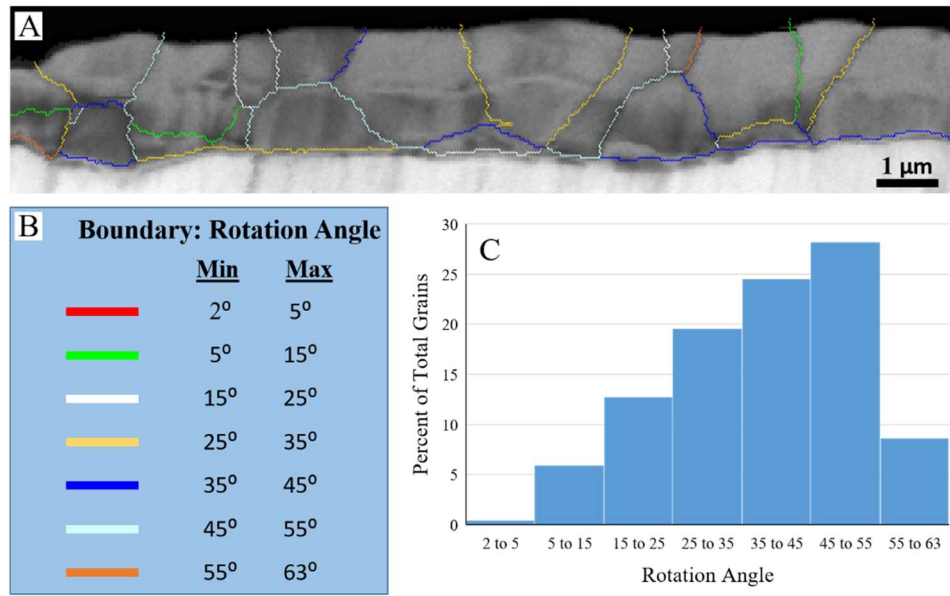


Figure 6.10 (A) Map showing Nb₃Sn coating on niobium with grain boundary misorientation information overlaid. (B) Legend for grain boundary rotation angles. (C) Data collected from ~250 grains located at the Nb/Nb₃Sn interface from multiple samples.

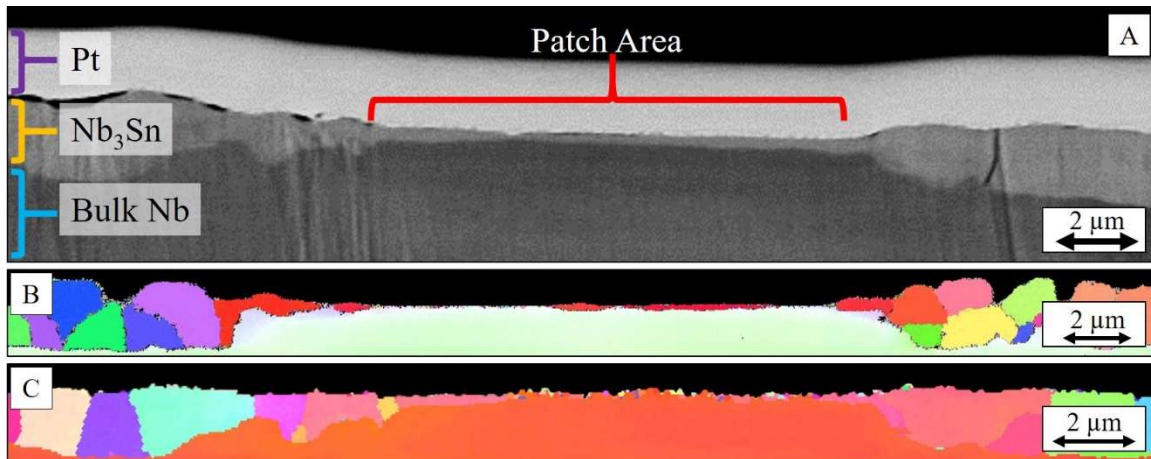


Figure 6.11 (A) SEM image of FIB cross sectioned patch defect. (B-C) Orientation maps of patch defects prepared by FIB.

6.3.3 Patch Defects

Patches are defects which form during the Nb₃Sn coating process to varying degree across many bulk material, cavity, and coating conditions. [90, 91] EDS surface analysis was reported by others which shows varying Nb/Sn ratio within the patch region with changing accelerating voltage. [92] This variation is indicative of a surface layer with thickness less than the escape depth of characteristic X-rays detected in EDS. The expected escape depth for Nb/Sn at the low end of the reported accelerating voltages is still several hundred nanometers, making it difficult to judge the actual patch thickness.

Here, cross sections from several patch defects from a single coupon were prepared by FIB and imaged by SEM, allowing for direct quantification of the thickness. Patch thickness was found to be 194(±59) nm as compared to overall Nb₃Sn thickness of 1.6(±0.1) μm for

the coupon. The reduced thickness within the patch region is of concern due to its relative closeness to the RF penetration depth (~170 nm). An SEM image of a FIB prepared patch cross section can be found in Figure 6.11A.

Example EBSD results from FIB prepared patch cross sections can be found in Figure 6.11B and Figure 6.11C. The patch cross sections clearly show a coating that forms at the niobium surface and progresses downward consuming niobium as tin is made available at the Nb₃Sn/Nb interface. A combination of relatively high beam current, low incidence angle, and possibly damage from polishing leads to the thinnest parts of the patch being unresolved in the EBSD maps shown. However, in all patches observed by SEM the Nb₃Sn layer appeared to be thin, but continuous across the entire patch area.

Surface EBSD analysis of patch afflicted Nb₃Sn was also performed, but is made difficult by the prominent topography of the surface. Figure 6.12 shows an SEM image with corresponding EBSD map. The combination of surface topography and low incidence angle (~20°) of the electron beam required for analysis forms many “shadowed” (black areas in Figure 6.12B) regions where no signal is produced. This produces a noisy surface map; however, the large patch areas are relatively smooth and index well. In agreement with the previously shown cross section EBSD, this map shows the patches are large single grains of Nb₃Sn. Both, cross section and surface analysis indicate that lack of grain boundaries is the limiting factor in coating growth rate for patch areas.

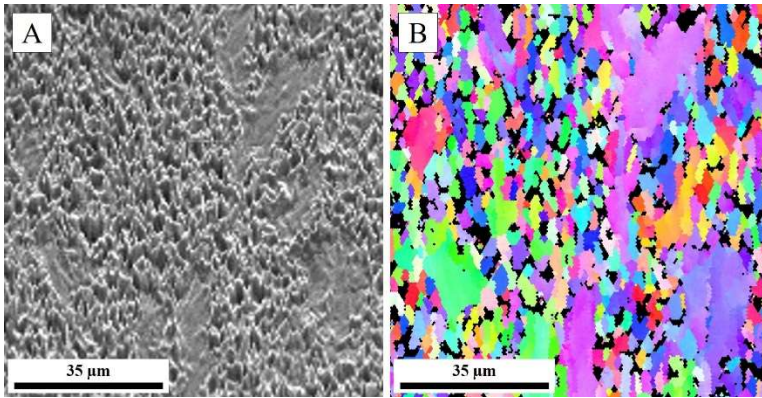


Figure 6.12 SEM image (A) and corresponding orientation map (B) of Nb₃Sn surface area containing patches. Patches index as single crystal Nb₃Sn.

6.3.4 Surface Anodization Effect on Coating

Recent coating experiments with anodized substrates have indicated a positive effect for the coating uniformity and reduction of patch defects. [93, 94] Other studies involving anodization and the nucleation process have shown mixed results. [63, 95] Here we use EBSD and analysis by NIH ImageJ software to help gain insight into the structural differences between Nb₃Sn grown on anodized niobium surfaces versus that grown on NP niobium surfaces.

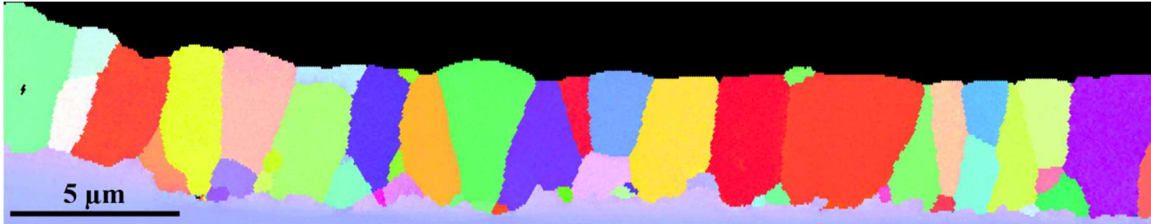


Figure 6.13 EBSD orientation map collected from a sample that was anodized prior to Nb₃Sn coating. (1100 °C / 12 hr)

Four coated samples were analyzed, two which had been anodized prior to coating and two which had not. Multiple maps were collected from each sample representing 100 – 200 μm of coating from each sample, which equates to ~100 grains of Nb₃Sn per sample. Figure 6.13 shows an example map collected from a sample anodized prior to Nb₃Sn coating. Comparing samples by average grain size proves difficult due to the large spread in size leading to large standard deviations. Coatings grown for 12 hr at 1100 °C were found to have an average grain size of 3.31 μm² (±3.7) for pre-anodized and 4.45 μm² (±4.8) for non-anodized. Viewing grain size as a histogram shows a clearer picture of differences (Figure 6.14), with the two samples showing a slightly different grain size distribution.

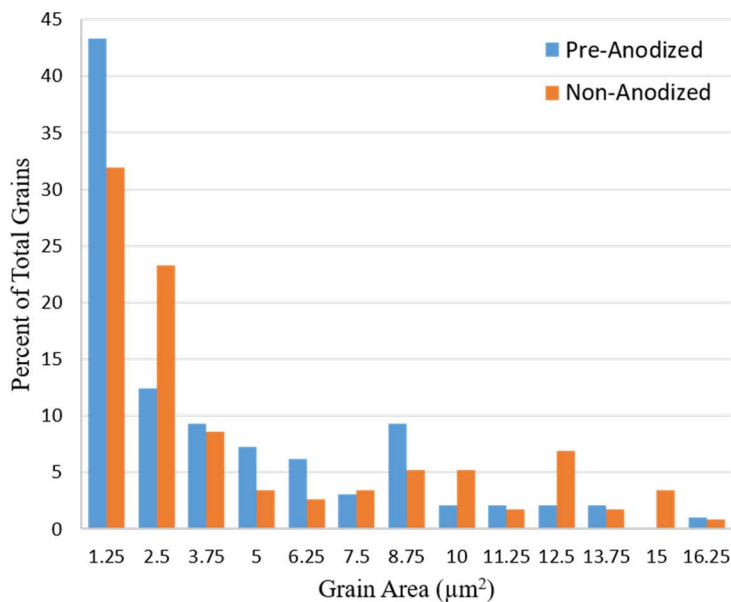


Figure 6.14 Histogram comparing grain size of Nb₃Sn coated samples with and without pre-anodization.

The aspect ratio of each grain was calculated by dividing the major axis by the minor axis of each grain giving a quantified value which represents the elongation of a grain. A perfectly square grain would have an aspect ratio of 1 and as the ratio increases so does the elongation of the grain. Again, a histogram is used to visualize the difference in aspect ratio between pre-anodized and non-anodized samples. (Figure 6.15) The distribution in grain aspect ratios appear very similar, with a preferred aspect ratio of ~1.5. The pre-anodized sample does show a smaller percentage of grains at the upper end (2.8 – 4.0) and a slightly higher center of distribution at 1.6 versus 1.4 for the non-anodized sample.

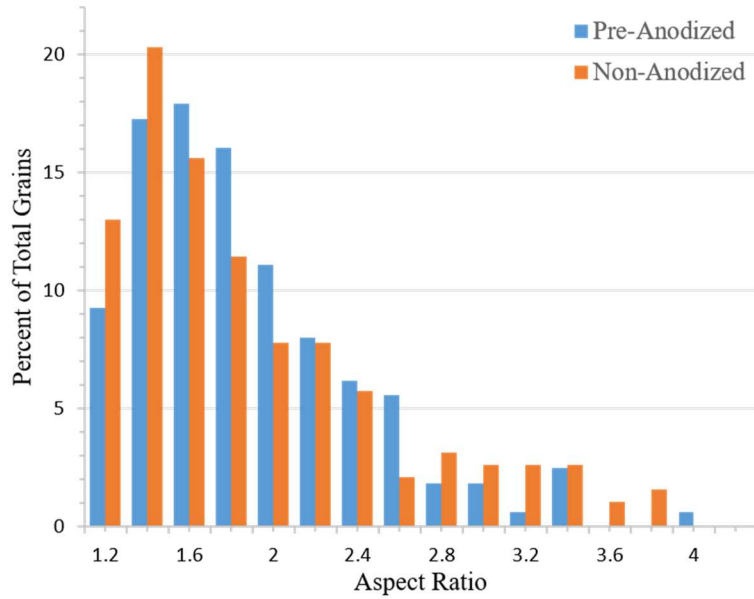


Figure 6.15 Histogram comparing the range of aspect ratio in Nb₃Sn coatings with and without pre-anodization.

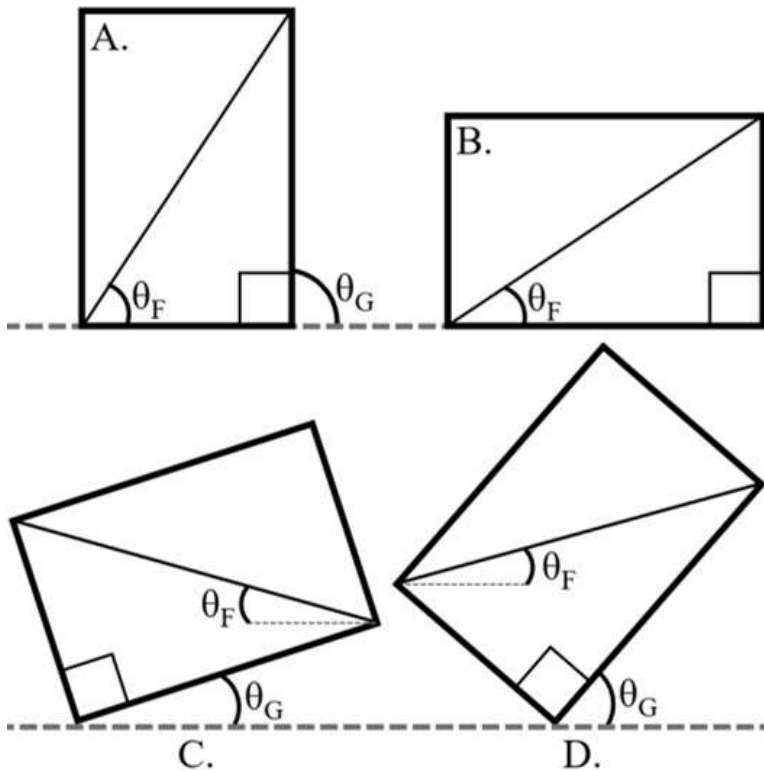


Figure 6.16 Graphic showing relationship of Feret angle to physical geometry of Nb₃Sn grain. Where θ_F is the Feret angle and θ_G is the orientation angle of the grain with respect to the x-axis.

Feret diameter is the longest distance between any two points along a particle's boundary, also described as the largest caliper measurement of the particle. The Feret angle is the angle between the Feret diameter and a line parallel to the x-axis of the image, which in our case is approximately parallel with the Nb/Nb₃Sn interface. It is possible to get some

statistical idea of the physical orientation of the grain within the coating using the Feret angle. If we assume a roughly rectangular shaped grain structure the Feret diameter is measured from corner to corner. A perfectly square grain with an aspect ratio of 1 would have a Feret angle of 45° when oriented square to the interface. For Nb_3Sn 's preferred aspect ratio of ~ 1.5 a Feret angle of $\sim 56^\circ$ would equate to a vertically oriented grain (Figure 6.16A) while an angle of $\sim 34^\circ$ would equate to a horizontally oriented grain (Figure 6.16B).

Angle distribution, shown in Figure 6.17, appears bimodal. With an aspect ratio of ~ 1.5 the peak seen at $\sim 60^\circ$ corresponds to vertically oriented grains. The second peak, seen at $\sim 15^\circ$, corresponds with grains which are physically oriented at either a 19° or 49° tilt to the horizontal axis (Figure 6.16C and D). Qualitatively, when viewing maps (Figure 6.13), large grains seem to be vertically oriented while smaller grains contribute to the large peak representing grains with 19° or 49° tilt. When plotted with respect to grain size (Figure 6.18) the bimodal nature of the Feret angle can be seen in smaller grain sizes with larger grains showing Feret angles distributed almost entirely around $\sim 60^\circ$. There are several outliers in the non-anodized data set attributable to “muffin-top” grains, where the maximum diameter of the grain is parallel to the niobium substrate, but is still a vertical grain. While these outliers are explained by the presence of large “muffin-top” grains vs large flat grains it is still of note that these do not appear in the pre-anodized samples.

In general, for uniform coating growth and reduction of patch defects, having smaller vertically oriented grains would be beneficial. The data here indicates pre-anodized samples have both. The pre-anodized samples show a larger number of the smallest grains of which a higher percentage appear to be oriented in a vertical direction. This illustrates a possible mechanism for the reduction of patch defects seen in pre-anodized samples.

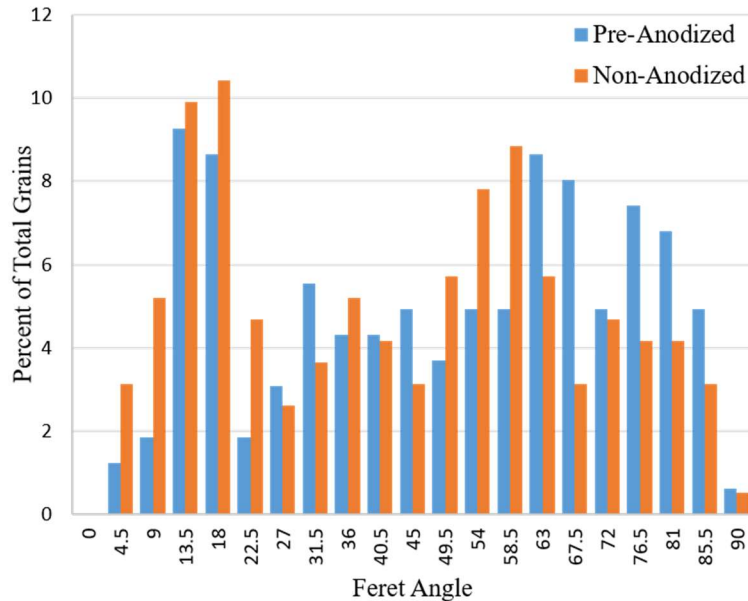


Figure 6.17 Histogram showing the distribution of the Feret angle for coatings grown with and without pre-anodization.

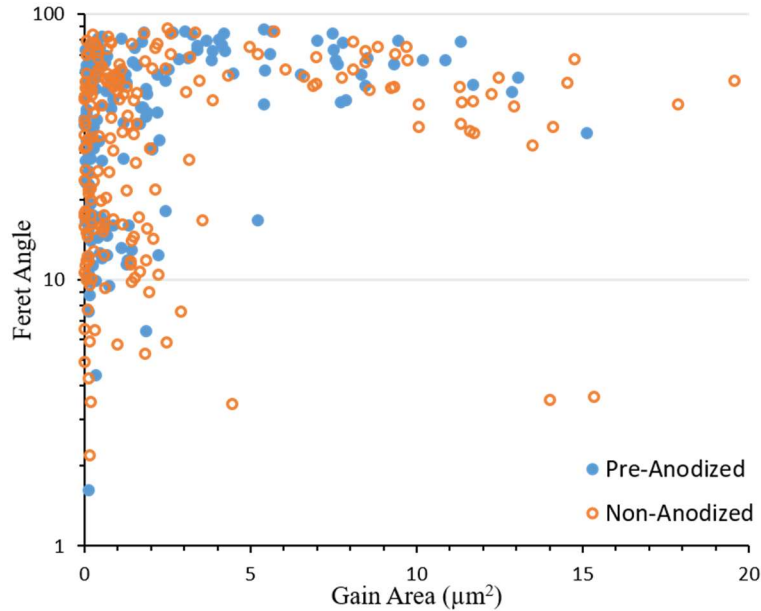


Figure 6.18 Plot showing Feret angle as a function of grain size for coatings grown with and without pre-anodization.

6.3.5 The Initial Overcoat Experiment

In order to gain insight into the formation and growth of Nb_3Sn films, previously coated coupons were subjected to additional coating and characterized. These coupons were referred to as “overcoat” samples. The overcoat samples were prepared by FIB and characterized by EBSD in cross section. Figure 6.19A shows an example orientation map from as-coated niobium while Figure 6.19B shows a sample which has been coated a second time. The overcoat sample shows the formation of new grains at the $\text{Nb}_3\text{Sn}/\text{Nb}$ interface. This indicates a formation mechanism which includes additional tin diffusion to the interface which initiates additional grain growth, as opposed to the formation of a new surface layer. In addition, grain formation appears to occur more times than not at the intersection of an original Nb_3Sn grain boundary and the niobium interface, indicating grain boundary diffusion as the primary mode for tin movement to the interface. Further evidence of this can be seen in the “cupping” at the base of many Nb_3Sn grains (Figure 6.19A), showing grain growth faster around the edges of the grain. With grain boundary diffusion as the primary mode of transport of tin to the growth interface, it follows that growth rate is inversely proportional to grain size. This is also supported and clearly seen in the patch defect work (Section 6.3.3).

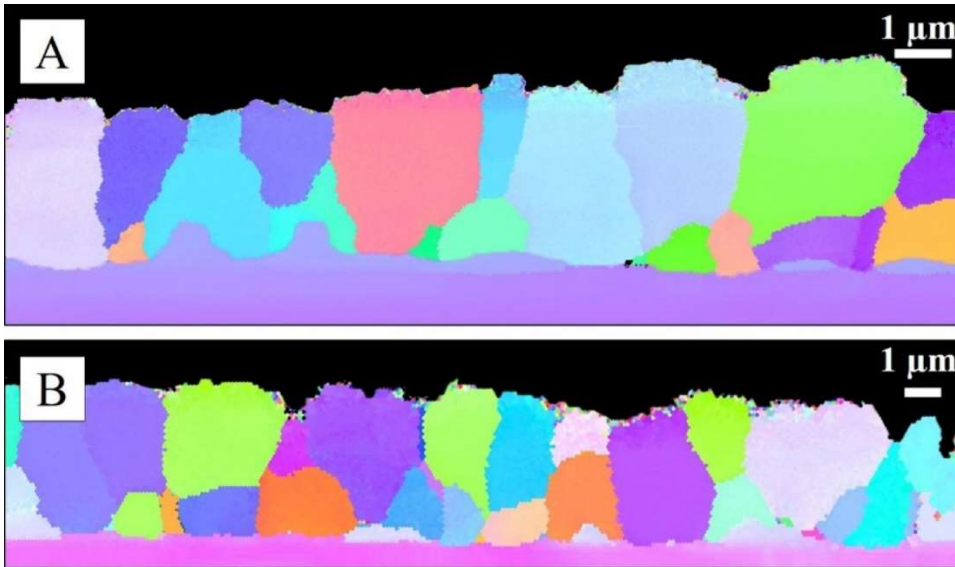


Figure 6.19 Orientation mapping of niobium coated with Nb₃Sn. Map (A) was coated in a single step while map (B) was coated then re-coated. Samples were prepared by FIB.

6.3.6 Continuation of the Overcoat Experiment

Results from section 6.3.5 initially seemed clear; overcoating causes more small grains to form at the interface. With time the larger volumes of EBSD data collected qualitatively appear to show small grains at the interface universally present and seemingly independent of coating condition. This suggests a mechanism of coating formation which requires small interfacial grains to be formed and then absorbed by larger grains which make up the bulk of the coating. Laid out below is a quantitative approach to explore this further. Data collected from six coated samples was analyzed. Nb₃Sn coating was performed in steps and total coating time varied with each sample. Table 6.1 shows the six coatings.

Table 6.1 Coating steps for six overcoat samples tested. "1" represents one hour of coating, "1+1" represents one hour of coating plus an additional hour, etc.

Sample	1	2	3	4	5	6
Coating Steps in Hours	1	1+1	1+1+1	1+1+1+3	1+1+1+3+12	1+1+1+3+12+60

Cross sections of each sample were prepared by FIB as described in section 6.2.2.7. Orientation maps from sample 2, 4, and 6 are shown in Figure 6.20A, B, and C respectively. Each map is limited to 15 μm in length in order to exhibit the large differences in relative grain size between coatings. In each of the three orientation maps, grains of ~1 μm are present. As the coating times increase the size of the grains forming the bulk of the coating also increases. Using NIH ImageJ software, size distribution for each sample was determined. The grain size distribution for sample one is shown in Figure 6.21A. The total coating time for the sample equals one hour and small grains account for 100% of the coating with a maximum grain size measured of 6.4 μm². After an additional hour of coating (two hours total) a bimodal distribution in grain size can start to be seen. (Figure 6.21B). Sample 2 had a maximum measured grain size of

$10.5 \mu\text{m}^2$. This bimodal distribution widens as the total coating time increases eventually ending in the extreme case of Sample 6. (Figure 6.21C). The largest measured grain area for Sample 6 was $183.0 \mu\text{m}^2$. Large grains, $>15 \mu\text{m}^2$, make up a total of 98% of the coating area. Interestingly the number of grains is split approximately evenly between small (48%) and large (52%). Data collected from the six samples seems to confirm the growth mechanism for Nb_3Sn requires small intermediate grains to form at the boundary layer, which then absorb and become part of the bulk coating as growth progresses. Again, for in-depth discussion of coating, mechanism, structure and composition please see U. Pudasaini et al.

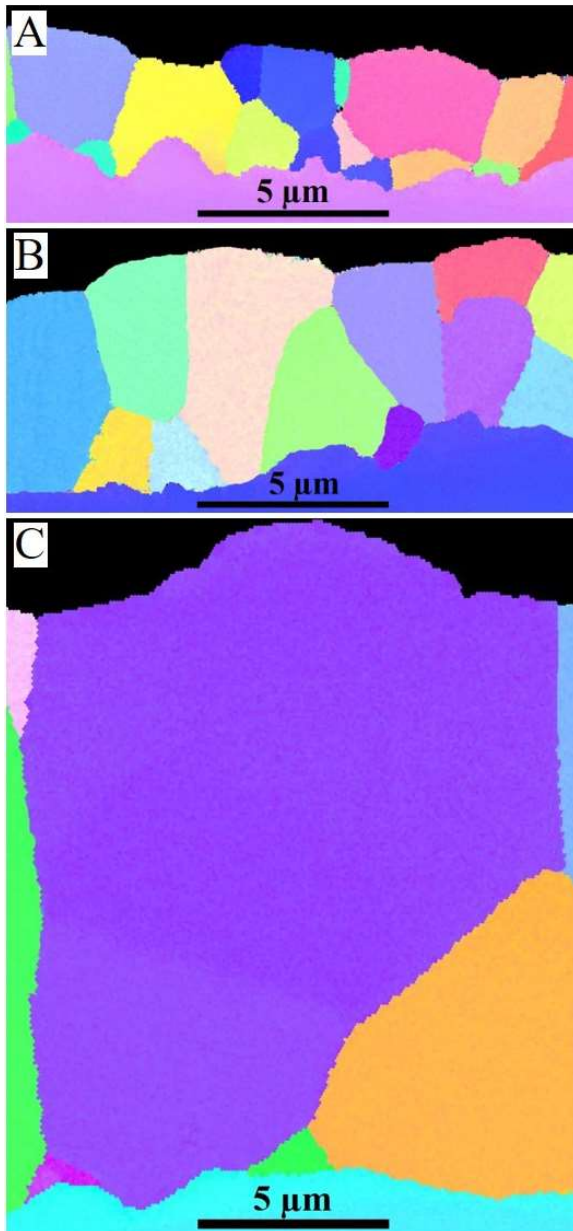


Figure 6.20 Orientation maps A, B, and C, collected from samples 2, 4, and 6 as found in Table 6.1. Each map shows a $15 \mu\text{m}$ length of Nb_3Sn coating.

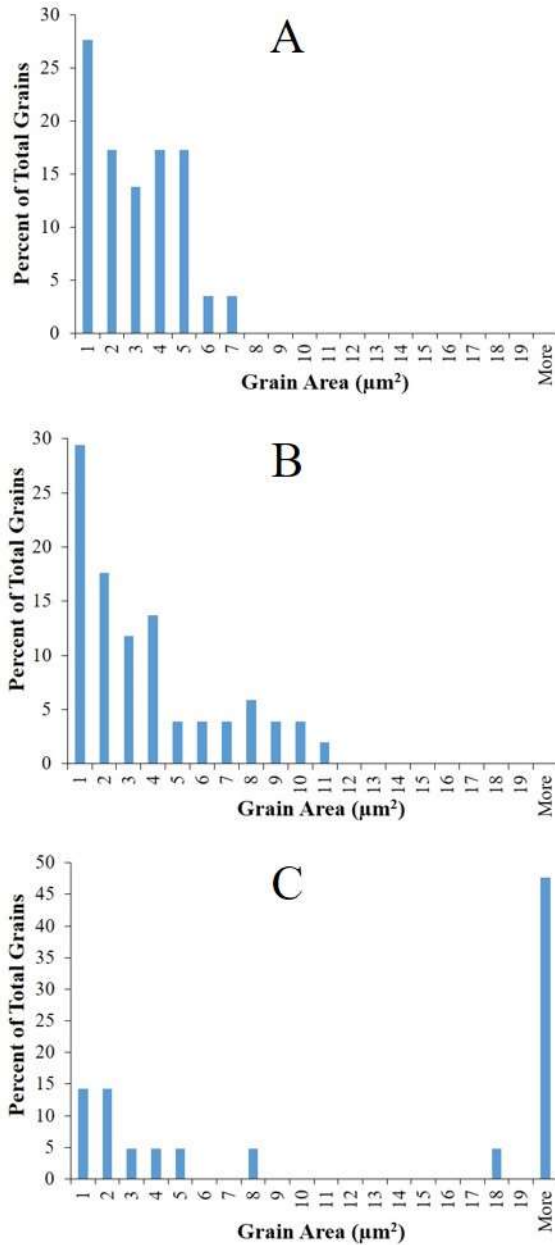


Figure 6.21 Histograms A, B, and C are grain size distributions for samples 1, 2, and 6 as found in Table 6.1.

6.4 Conclusion

This work has shown EBSD is the method of choice to visualize and quantify structure as a function of depth for Nb₃Sn coated SRF cavity material. Some of the results have been disseminated. [88, 96] Ion beam sample preparation methods were found to perform best for EBSD quality surface finishes. Diffuse ion beam polishing, accomplished here via the Leica TIC 3x, was successful to create large analysis areas with 100's of microns of usable area. Thus far, EBSD analysis over many hundreds of microns of coating on both polycrystalline and single crystal samples has shown no preferred crystal orientation based

on the bulk niobium substrate. Complimentary to diffuse ion polishing, FIB preparation works well in the case of small or geometrically complicated samples. To this point, example analyses were shown from cavity cutout samples which exhibit EBSD's ability to determine structure for complicated geometries, making it possible to directly compare differing areas of coated cavities or target specific defect types.

Work with patch defects indicates Nb₃Sn forms at the Nb₃Sn/Nb interface, progressing "downward" and consuming bulk niobium as tin is made available at the interface through grain boundary diffusion. This implies patches arise from the formation of large single crystal grains early in the coating process. Due to a lack of grain boundaries, the interface is starved of Sn inhibiting further growth of Nb₃Sn in the patch area.

Following the idea of a growth process which is dependent on grain boundaries for growth, aspect ratio, physical grain orientation, and grain size will play a large part in coating rate and uniformity. EBSD and image analysis software were used to quantify these parameters in pre-anodized and non-anodized Nb₃Sn coatings. While further investigation is outside the scope of this work, the differences indicated, namely smaller and more vertically oriented grains, may help elucidate pre-anodizing's ability to reduce patch defects.

6.5 Acknowledgment

- Co-Authored by Jefferson Science Associates, LLC under U.S. DOE Contract No. DE-AC05-06OR23177
- We are grateful for support from the Office of High Energy Physics, U.S. Department of Energy under grant DE-SC0014475 to the College of William & Mary.
- The Institute for Critical Technology and Applied Science (ICTAS), and Nanoscale Characterization and Fabrication Laboratory (NCFL) at Virginia Tech

Chapter 7

7 Summary and Recommendations

The advancement of SRF materials depends on the advancement of the fundamental understanding of several new materials technologies, in particular, doping techniques and coatings such as Nb₃Sn. Historically, the majority of cavity processing and materials research has been accomplished in an empirical way: repeatedly building, processing, and testing cavities to obtain the best results. This approach is not optimal. Cavity manufacture and processing affect cavity material structure on a scale congruent with the RF interaction depth. It is the material in this RF region that is mainly responsible for the overall cavity performance, i.e. processing determines structure and structure determines performance. The work here moves SRF research in the direction of not only empirically processing and testing cavities, but understanding how this processing affects the material structure. Having a fundamental understanding of the changes in structure not only helps understand how to control a cavity's material structure, but also helps determine what structural targets are important to maximize cavity performance. This streamlines SRF research, leading to more informed research decisions. In order to gain this insight it was necessary to employ advanced material characterization techniques. However, these techniques are not always straight-forward, requiring material specific technique and method development. The work here was devoted to the development of SRF material specific methods and how they might be used to fundamentally inform SRF research. In particular the use of SIMS, EBSD, and XPS has proved quite fruitful. Summarized below are a few specific examples of each of these three techniques:

- SIMS was shown to be the ultimate technique for characterizing dopants and contaminants in doped SRF materials (Chapter 4). It was used to perform doping studies for both low and high temperature doped materials. It was also used to determine baseline nitrogen and oxygen levels in raw preprocessed cavity material.
- For the first time EBSD was used to analyze vapor deposited Nb₃Sn on cavities and cavity witness coupons (Chapter 6). This allowed direct analysis of meaningful areas of coating for both dynamic experiments and coating defects not possible before. Data was shown from various cavity locations, coating experiments such as overcoat and pre-anodization, and defect work such as the common "patch defect".
- XPS is a readily available technique, which is cheaper and technically easier to utilize than SIMS while providing analogous information. Here, XPS was shown not suitable for detection of low concentration nitrogen which is necessary for the characterization of doped samples. However, XPS does provide an alternative to SIMS for depth profiling of non-trace elements, as exemplified in work with Nb₃Sn and surface anodization. (Section 5.3.4 and Appendix 5.B) The technique is also ideally suited for describing a material's surface in detail. Such analysis is represented in the description of Nb₃Sn surface found in Appendix 5.A.
- Meticulous sample preparation and management is necessary for repeatable and dependable characterization. Sample preparation methods are discussed in depth

for each of the techniques utilized. Examples included sample surface finish and loading scheme for SIMS analysis (Chapter 4), ion beam surface polishing for EBSD (Chapter 6), and the method of angle polishing for extending the range of depth profiles for both SIMS and XPS (Section 5.3.3).

In closing, going forward there is a vast potential of applications for the characterization techniques explored here and a wealth of fundamental materials knowledge to be elucidated. SIMS methods described here are currently being used to support a research effort coordinated with multiple national labs involving many dozens of witness samples, with the goal of expanding the community's collective knowledge of how low temperature doping affects SRF material structure within the first several hundred nanometers of the surface. This research is central to the SRF community as a whole. Future work for SIMS may include further exploration of how crystal orientation affects the doping process. Preliminary investigations here have shown a clear experimental path forward. It is unclear what is the importance of an orientation effect for low temperature doped cavities, however with currently used doping recipes average cavity orientation may play a large role in overall amount of bulk nitrogen after doping.

The development of an EBSD method for Nb₃Sn coated niobium has proven to be a valuable asset and opened new possibilities for Nb₃Sn experiments. For experiments such as overcoating and pre-anodization, or defect analysis such as the characterization of patch defects, EBSD has provided direct measurement and orientation imaging impossible by any other technique. For example, EBSD has shown orientation data at the Nb₃Sn/Nb interface on a scale (many millimeters of collected data) impractical by other methods such as TEM. Currently there are multiple experiment programs moving forward using methods based on this work, including coating dependence on time and temperature, overcoating, pre-anodization, and nucleation step samples.

As previously mentioned, processing determines structure and structure determines performance. For a complete description of SRF cavity performance it is necessary to have a fundamental understanding of the materials structure. To accomplish this, robust and repeatable materials characterization methods and practices are needed. The work described here pushes towards that goal.

Bibliography

- [1] S. Giordano, H. Hahn, H. Halama and C. Varmazis, "Influence of Solute Oxygen and Nitrogen on Superconducting Niobium Cavities," *Journal of Applied Physics*, vol. 44, no. 9, p. 4185, 1973.
- [2] C. Koch, J. Scarbrough and D. Kroeger, "Effects of Interstitial Oxygen on the Superconductivity of Niobium," *Physical Review B*, vol. 9, no. 3, p. 888, 1974.
- [3] M. Alam and T. Debroy, "Nitrogen Solubility in Solid Niobium," *Metallurgical Transactions B*, vol. 19B, p. 613, 1988.
- [4] Z. Hu, Y. Li, M. Ji and J. Wu, "The Interaction of Oxygen with Niobium studied by XPS and UPS," *Solid State Communications*, vol. 71, no. 10, pp. 849-852, 1989.
- [5] P. Maheshwari, F. Stevie, G. Myneni, G. Ciovati, J. Rigsbee and D. Griffis, "Analysis of Interstitial Elements in Niobium with Secondary Ion Mass Spectrometry (SIMS)," *AIP Conference Proceedings*, vol. 1352, pp. 151-160, 2011.
- [6] A. Grassellino, A. Romanenko, D. Sergatskov, O. Melnychuk, Y. Trenikhina, A. Crawford, A. Rowe, M. Wong, T. Khabiboulline and F. Barkov, "Nitrogen and Argon Doping of Niobium for Superconducting Radio Frequency Cavities: A pathway to highly efficient accelerating structures," *Superconductor Science and Technology*, vol. 26, 2013.
- [7] M. Pham, K. Mbaye, L. Wartski and J. Halbritter, "RF Characterization of Thermally Diffused Superconducting Niobium Nitride," *Journal of Applied Physics*, vol. 63, no. 9, p. 4586, 1988.
- [8] C. Benvenuti, L. Chiggiato, L. Parrini and R. Russo, "Reactive Diffusion Produced Niobium Nitride Films for Superconducting Cavity Applications," *Nuclear Instruments and Methods in Physics Research Section A: Accelerators, Spectrometers, Detectors and Associated Equipment*, vol. 336, no. 1/2, p. 16, 1993.
- [9] P. Dhakal, G. Ciovati, P. Kneisel and G. Myneni, "Enhancement in Quality Factor of SRF Niobium Cavities by Material Diffusion," *IEEE Transactions on Applied Superconductivity*, vol. 25, no. 3, 2015.
- [10] P. Maheshwari, F. Stevie, G. Myneni, G. Ciovati, J. Rigsbee, P. Dhakal and P. Griffis, "SIMS Analysis of High-Performance Accelerator Niobium," *Surface and Interface Analysis*, vol. 46, pp. 288-290, 2014.
- [11] F. Stevie, "SRF Niobium Characterization Using SIMS and FIB-TEM," in *AIP Conference Proceedings*, 2015.
- [12] A. Crawford, R. Eichhorn, F. Furuta, G. Ge, D. Gonella, A. Grassellino, M. Liepe, A. Palczewski and C. Reece, "The Joint High Q R&D Program for LCLS-II," in *Proceedings of IPAC 2014*, Dresden, 2014.

- [13] D. Gonnella, M. Ge, F. Furuta and M. Liepe, "Nitrogen Treated Cavity Testing at Cornell," in *Proceedings of LINAC 2014*, Geneva, 2014.
- [14] A. Palczewski, R. Geng and C. Reece, "Analysis of New High-Q SRF Cavity Tests by Nitrogen Gas Doping at Jefferson Lab," in *Proceedings of LINAC 2014*, Geneva, 2014.
- [15] T. Massalski, H. Okamoto, P. Subramanian and L. Kacprzak, *Binary Phase Diagrams*, 2nd Edition, Par, Ohio: ASM International, 1990.
- [16] J. T. Clenny and C. J. Rosa, "Nitridation Kinetics of Niobium in the Temperature Range of 873 to 1273 K," *Metallurgical Transactions A*, vol. 11A, no. September 1980, p. 1575, 1980.
- [17] A. D. Palczewski, "Investigation of Nitrogen Absorption Rate and Nitride Growth on SRF Cavity Grade RRR Niobium as a Function of Furnace Temperature," in *LINAC 2016*, East Lansing MI, 2016.
- [18] A. Taylor and N. Doyle, "The Solid and Solubility of Nitrogen in Nb and Nb-Rich Nb-Hf, Nb-Mo and Nb-W Alloys," *Journal of the Less-Common Metals*, vol. 1967, no. 13, pp. 399-412, 1967.
- [19] M. Hilbig and A. Prudnikava, "Calculation of Diffusion Profiles of Nitrogen in Niobium to Investigate the Surface Concentration After Nitrogen Treatment Experiments," *Summer Student Project at DESY*, 2014.
- [20] D. Gonnella, J. Kaufman, P. Koufalidis and M. Liepe, "RF Losses From Trapped Flux in SRF Cavities," in *Proceedings of IPAC 2016*, Busan, 2016.
- [21] H. Padamsee, J. Kobloch and T. Hays, *RF Superconductivity for Accelerators*, Germany: Wiley-VCH, 2008.
- [22] Y. Trenikhina, A. Grassellino, F. Barkov and A. Romanenko, "Chemical Structure of Niobium Samples Vacuum Treated in Nitrogen in Parallel With Very High Q Cavities," *Proceedings of SRF2013, Paris, France*, vol. TUP065, no. 06 Materials Studies, p. 583, 2013.
- [23] D. Gonella and M. Liepe, "New Insights Into Heat Treatment of SRF Cavities in a Low-Pressure Nitrogen Atmosphere," in *Proceedings of IPAC 2014*, Dresden, 2014.
- [24] W. DeSorbo, "Effects of Dissolved Gases on Some Superconducting Properties of Niobium," *Phys. Rev.*, vol. 132, no. 107, October 1963.
- [25] A. Romanenko and A. Grassellino, "Dependence of the Microwave Surface Resistance of Superconducting Niobium on the Magnitude of the RF Field," *Appl. Phys. Lett.*, Vols. 102, 252603, 2013.
- [26] C. Reece, A. Palczewski and B. Xiao, "An Analysis of the Temperature and Field Dependence of the RF Surface Resistance of Nitrogen-Doped Niobium SRF

- Cavities with Respect to Existing Theoretical Models," in *Proceedings of IPAC 2015*, Richmond, 2015.
- [27] D. Gonnella, J. Kaufman and M. Liepe, "Impact of Nitrogen Doping of Niobium Superconducting Cavities on the Sensivity of Surface Resistance to Trapped Magnetic Flux," *Journal of Applied Physics*, vol. 119, 2016.
- [28] D. Gonnella and M. Liepe, "Flux Trapping in Nitrogen-Doped and 120C Baked Cavities," in *Proceedings of IPAC 2014*, Dresden, Germany, 2014.
- [29] M. Liepe, B. Clasby, R. Eichorn, F. Furuta, G. Ge, D. Gonnella, T. Gruber and D. Hall, "Niobium Impurity-Doping Studies at Cornell and CM Cool-Down Dynamic Effect on Q," in *Proceedings of SRF 2015*, Whistler, 2015.
- [30] D. Gonnella, M. Liepe and J. Kaufman, "Sensitivity of Niobium Superconducting RF Cavities to Magnetic Field," in *Proceedings of SRF 2015*, Whistler, 2015.
- [31] M. Martinello, M. Checchin, A. Grassellino, O. Melnychuk, S. Posen, A. Romanenko, D. Sergatskov and J. Zasadzinski, "Tailoring Surface Impurity Content to Maximize Q-Factors of Superconducting Resonators," in *Proceedings of IPAC 2016*, Busan, 2016.
- [32] D. Gonnella, F. Furuta, M. Ge, J. Kaufman, M. Liepe and J. Maniscalco, "Update on Nitrogen Doping; Quench Studies and Sample Analysis," in *Proceedings of IPAC 2015*, Richmond, Va, USA, 2015.
- [33] A. Grassellino, A. Romanenko, S. Posen, Y. Trenikhina, O. Melnychuk, D. Sergatskov, M. Merio, M. Checchin and M. Martinello, "N Doping: Progress in Development and Understanding," in *Proceedings for SRF 2015*, Whistler, 2015.
- [34] A. Grassellino, A. Romanenko, Y. Trenikhina, M. Checchin, M. Martinello and S. Posen, "Unprecedented Quality Factors at Accelerating Gradients up to 45 MV/m in Nb Superconducting Resonators via Low Temperature Nitrogen Infusion," *Superconductor Science and Technology*, vol. 30, no. 9, 2017.
- [35] M. Kelley, G. Ereemeev, U. Pudasaini, C. Reece and J. Tuggle, "Intermetallic Coatings for Energy-Efficient Particle Accelerators," in *Materials Research Society*, Boston, 2016.
- [36] B. Hillenbrand, H. Martens, H. Pfister, K. Schnitzke and Y. Uzel, "Superconducting Nb₃Sn Cavities with High Microwave Qualities," *Transactions on Magnetism*, Vols. MAG-13, no. No. 1, pp. 491-495, 1977.
- [37] M. Peiniger and H. Piel, "A Superconducting Nb₃Sn Coated Multicell Accelerating Cavity," *Transaction on Nuclear Science*, Vols. NS-32, no. No. 5, pp. 3610-3612, 1985.
- [38] S. Posen and M. Liepe, "Advances in development of Nb₃Sn superconducting radio-frequency cavities," *Phys. Rev. Special Topics - Acc. and Beams*, vol. 17, no. 112001, 2014.

- [39] S. Posen and D. Hall, "Nb₃Sn superconducting radiofrequency cavities: fabrication, results, properties, and prospects," *Supercond. Sci. Technol.*, vol. 30, no. 033004, 2017.
- [40] G. Ereemeev, W. Clemens, K. Macha, H. Park and R. Williams, "Commissioning of Nb₃Sn Cavity Vapor Diffusion Deposition System at JLab," in *Proceedings of IPAC 2015*, Richmond, Va, 2015.
- [41] P. Koufalidis, J. Maniscalco and M. Liepe, "Low Temperature Doping of Niobium: Whats Really Going On?," in *Proceedings of SRF2017*, Lanzhou, China, 2017.
- [42] P. Dhakal, G. Ciovati, G. Myneni, K. Gray, N. Groll, P. Maheshwari, D. McRae, R. Pike, T. Proslie, F. Stevie, R. Walsh, Q. Yang and J. Zasadzinski, "Effect of High Temperature Heat Treatments on the Quality Factor of a Large-Grain Superconducting Radio-Frequency Niobium Cavity," *Physical Review Special Topics-Accelerators and Beams*, vol. 16, no. 042001, 2013.
- [43] G. Ciovati, P. Dhakal and G. Myneni, "Superconducting Radio-Frequency Cavities Made from Medium and Low-Purity Niobium Ingots," *Superconductor Science and Technology*, vol. 29, no. 6, 2016.
- [44] A. Burrill, D. Gonnella, M. Ross, K. Davis, A. Palczewski, L. Zhao, A. Grassellino and O. Melnychuk, "Vertical Test Results for the LCLS-II 1.3 GHz First Article Cavities," in *Proceedings of IPAC*, Copenhagen, 2017.
- [45] D. Gonnella, S. Aderhold, A. Burrill, E. Daly, K. Davis, A. Grassellino, C. Grimm, A. Palczewski and S. Posen, "RF Performance of Nitrogen-Doped Production SRF Cavities for LCLS-II," in *Proceedings of IPAC*, Copenhagen, 2017.
- [46] D. Hall, J. Kaufman, M. L. R. Porter and J. Sears, "First Results From New Single-Cell Nb₃Sn Cavities Coated at Cornell University," in *Proceedings of IPAC 2017*, Copenhagen, 2017.
- [47] P. Boccard, P. Kneisal, G. Muller, J. Pouryamout and H. Piel, "Results from some temperature mapping experiments on Nb₃Sn RF Cavities," in *Workshop on RF Superconductivity*, Padova, 1997.
- [48] K. Wittmaack, "Influence of the Impact Angle on the Depth Resolution and the Sensitivity in SIMS Depth ling Using a Cesium Ion Beam," *Journal of Vacuum Science and Technology A: Vacuum, Surface, and Films* 3, p. 1350, 1985.
- [49] S. Lozano-Perez, M. Schroder, T. Yamada, T. Terachi, C. English and C. Grovenor, "Using NanoSIMS to map trace elements in stainless steels from nuclear reactors," *Applied Surface Science*, vol. 255, no. 4, pp. 1541-1543, 2008.
- [50] E. Seebauer and D. Barlaz, "SIMS for analysis of nanostructures," *Current Opinion in Chemical Engineering*, vol. 12, pp. 8-13, 2016.

- [51] S. Hofmann, "Ultimate Depth Resolution and Profile Reconstruction in Sputter Profiling with AES and SIMS," *Surface and Interface Analysis*, no. 30, pp. 228-233, 2000.
- [52] F. Stevie, *Secondary Ion Mass Spectrometry*, New York, NY: Momentum Press, 2016.
- [53] R. Wilson, F. Stevie and C. Magee, *Secondary Ion Mass Spectrometry*, New York: Wiley, 1989.
- [54] SRIM, *Stopping Range of Ions In Matter [Software]*, www.SRIM.org, ver: SRIM 2013.00.
- [55] *Wah Chang proprietary polishing process.*
- [56] P. Maheshwari, *Surface Characterization of Impurities in Superconducting Niobium for Radio Frequency (RF) Cavities used in Particle Accelerators*, Raleigh, North Carolina: Dissertaton, NCSU, 2012.
- [57] M. Wenskat, A. Prudnikava, D. Reschke and J. Schaffran, "Nitrogen Infusion R&D on Single Cell Cavities at DESY," in *Proceedings of SRF 2017*, Lanzhou, 2017.
- [58] T. Konomi, T. Dohmae, Y. Hori, E. Kako, T. Kubo, G. Park, H. Sakai and K. Umemori, "Trial of Nitrogen Infusion and Nitrogen Doping by Using J-Parc Furnace," in *Proceedings of SRF 2017*, Lanzhou, 2017.
- [59] J. Tuggle, U. Pudasaini, A. Palczewski, C. Reece, F. Stevie and M. Kelley, "Fundamental SIMS Analyses for Nitrogen Enriched Niobium," in *SRF Conference Proceedings*, Lanzhou, 2017.
- [60] J. Tuggle, U. Pudasaini, A. Palczewski, C. Reece, F. Stevie and M. Kelley, "Secondary Ion Mass Spectrometry for Superconducting Radiofrequency Cavity Materials," *Journal of Vacuum Science & Technology B*, vol. 36, no. 5, p. 052907, 2018.
- [61] U. Pudasaini, M. Kelley, G. Ereemeev and C. Reece, "Local Composition and Topography of Nb₃Sn Diffusion Coatings on Niobium," in *17th International Conference on RF Superconductivity*, Whistler, BC, Canada, 2015.
- [62] A. Palczewski, C. Reece, F. Stevie, M. Kelley and J. Tuggle, "Investigation of Nitrogen Absorption and Nitride Growth on SRF Cavity Grade RRR Niobium as a Function of Furnace Temperature," in *Proceedings of LINAC 2016*, East Lansing, MI, 2016.
- [63] U. Pudasaini, G. Ereemeev, J. T. C.E. Reece and M. Kelley, "Initial Growth of Tin on Niobium for Vapor Diffusion Coating of Nb₃Sn," *Superconductor Science and Technology*, vol. Accepted, 2019.

- [64] M. Seah and W. Dench, "Quantitative Electron Spectroscopy of Surfaces: A Standard Data Base for Electron Inelastic Mean Free Paths in Solids," *Surface and Interface Analysis*, vol. 1, no. 1, pp. 2-11, 1979.
- [65] J. Watts and J. Wolstenholme, *An Introduction to Surface Analysis by XPS and AES*, West Sussex: Wiley, 2003.
- [66] A. Dacca, G. Gemme, L. Mattera and R. Parodi, "XPS Characterization of Niobium for RF Cavities," in *Proceedings of the 1997 Workshop on RF Superconductivity*, Abano Terme, 1997.
- [67] B. Feddes, A. Vredenberg, J. Wolke and J. Jansen, "Determination of Photoelectron Attenuation Length in Calcium Phosphate Ceramic Films Using XPS and RBS," *Surface and Interface Analysis*, vol. 35, pp. 287-293, 2003.
- [68] H. Tian, A.-M. Valente and M. Kelley, "Near-Surface Composition of Electropolished Niobium by Variable Photon Energy XPS," in *Proceedings of the 11th Workshop on RF Superconductivity*, Lubeck, Germany, 2003.
- [69] H. Tian, C. Reece, M. Kelley, S. Wang, L. Plucinski, K. Smith and M. Nowell, "Surface Studies of Niobium Chemically Polished under Conditions for Superconducting Radio Frequency Cavity Production," *Applied Surface Science*, vol. 253, pp. 1236-1242, 2006.
- [70] A. Darlinski and J. Halbritter, "Angle-resolved XPS Studies of Oxides at NbN, NbC, and Nb Surfaces," *Surface and Interface Analysis*, vol. 10, pp. 223-237, 1987.
- [71] C. Powell and A. Jablonski, "NIST Electron Effective-Attenuation-Length Database," *NIST Standard Reference Database 82*, 2011.
- [72] P. Dhakal, S. Chetri, S. Balachandran, P. Lee and G. Ciovati, "Effect of Low Temperature Baking in Nitrogen on the Performance of a Niobium Superconducting Radio Frequency Cavity," *Physical Review Accelerators and Beams*, vol. 21, no. 032001, 2018.
- [73] D. Hall, M. Liepe, J. Maniscalco and S. Posen, "Recent Studies on the Current Limitations of State-of-art Nb₃Sn Cavities," in *6th International Particle Accelerator Conference*, Richmond, 2015.
- [74] J. Tuggle, U. Pudasaini, A. Palczewski, C. Reece, F. Stevie and M. Kelley, "Secondary Ion Mass Spectrometry for SRF Cavity Materials," *arXiv preprint*, 2018.
- [75] D. Stojakovic, "Electron Backscatter Diffraction in Materials Characterization," *Processing and Application of Ceramics*, vol. 6, no. 1, pp. 1-13, 2012.
- [76] V. Randle, "Electron Backscatter Diffraction: Strategies for Reliable Data Acquisition and Processing," *Materials Characterization*, vol. 60, pp. 913-922, 2009.

- [77] T. Maitland and S. Sitzman, Chapter exert from "Scanning Microscopy for Nanotechnology Techniques and Applications", Springer, 2007.
- [78] R. Borrajo-Pelaez and P. Hedstrom, "Recent Developements of Crystallographic Analysis Methods in the Scanning Electron Microscope for Applications in Metallurgy," *Critical Reviews in Solid State and Materials Sciences*, pp. 1-20, 2017.
- [79] T. Britton, J. Jiang, Y. Guo, A. Vilalta-Clemente, D. Wallis, L. Hansen, A. Winkelmann and A. Wilkinson, "Tutorial: Crystal Orientations and EBSD - Or which way is up?," *Materials Characterization*, vol. 117, pp. 113-126, 2016.
- [80] A. Wilkinson, G. Moldovan, T. Britton, A. Bewick, R. Clough and A. Kirkland, "Direct Detection of Electron Backscatter Diffraction Patterns," *Physical Review Letters*, vol. 111, no. 6, 2013.
- [81] A. Wilkinson and T. Britton, "Strains, Planes, and EBSD in Materials Science," *Materials Today*, vol. 15, no. 9, 2012.
- [82] A. Schwartz and B. A. M. Kumar, *Electron Backscatter Diffraction in Materials Science*, Springer, 2009.
- [83] K. Baba-Kishi, "Review Electron Backscatter Kikuchi Diffraction in the Scanning Electron Microscope for Crystallographic Analysis," *Journal Of Materials Science*, vol. 37, pp. 1715-1746, 2002.
- [84] F. Humphreys, "Review Grain and Subgrain Characterization by Electron Backscatter Diffraction," *Journal of Materials Science*, vol. 36, pp. 3833-3854, 2001.
- [85] S. Zaefferer, "A Critical Review of Orientation Microscopy in SEM and TEM," *Crystal Research and Technology*, vol. 46, no. 6, pp. 607-628, 2011.
- [86] D. Dingley, "Progressive Steps in the Developement of Electron Backscatter Diffraction and Orientation Imaging Microscopy," *Journal of Microscopy*, vol. 21, no. 3, pp. 214-224, 2003.
- [87] J. Tuggle, A. Palczewski, C. Reece, F. Stevie and M. Kelley, "Investigation of Low-Level Nitrogen in Niobium by Secondary Ion Mass Spectrometry," in *Proceedings of LINAC 2016*, East Lansing, 2016.
- [88] J. Tuggle, G. Ereemeev, C. Reece, H. Xu and M. Kelley, "Structure and Composition of Nb₃Sn Diffusion Coated Films on Nb," in *Proceedings of SRF 2015*, Whistler, 2015.
- [89] U. Pudasaini, G. Ereemeev, C. Reece, J. Tuggle and M. Kelley, "Examination of Cutouts Inner Surfaces From Nb₃Sn Coated Cavity," *Proceedings of LINAC*, 2016.
- [90] S. Posen, Writer, *Nb₃Sn SRF Coatings at FermiLab*. [Performance]. NAPAC, 2016.
- [91] S. Posen, A. Romanenko, Y. Trenikhina, O. Melnychuk and D. Sergatskov, "Cutout Study of a Nb₃Sn Cavity," in *Pocceedings of SRF2015*, Whistler, BC, 2015.

- [92] D. Hall, J. Kaufman, M. Liepe and J. Maniscalco, "Surface Analysis Studies of Nb₃Sn Thin Films," in *IPAC 2016 Proceedings*, Busan, Korea, 2016.
- [93] U. Pudasini, G. Ereemeev, M. Kelley, C. Reece and J. Tuggle, "Surface Studies of Nb₃Sn Coated Samples Prepared Under Different Coating Conditions," in *18th International Conference on RF Superconductivity*, Lanzhou, 2017.
- [94] D. Hall, M. Liepe, R. Porter, T. Arias, P. Cueva, D. Liarte, D. Muller, J. Sethna and N. Sitaraman, "High Performance Nb₃Sn Cavities," in *18th International Conference on RF Superconductivity*, Lanzhou, 2017.
- [95] D. Hall, *New Insights into the Limitations on the Efficiency and Achievable Gradients in Nb₃Sn SRF Cavities*, PhD Thesis Cornell University, 2017.
- [96] J. Tuggle, U. Pudasini, G. Ereemeev, A. Palczewski, C. Reece and M. Kelley, "Materials Characterization for SRF Cavities: Gaining Insight Into Nb₃Sn," in *IPAC Conference Proceedings*, Copenhagen, 2017.
- [97] Z. Yang, X. Lu, L. Lin, J. Zhao, D. Yang and W. Tan, "TOF-SIMS Study of Nitrogen Doping Niobium Samples," in *Proceedings of SRF 2015*, Whistler, 2015.
- [98] Z. Yang, X. Lu, D. Xie, L. Lin and W. Tan, "Plasma Cleaning: A New Possible Treatment for Niobium Superconducting Cavity After Nitrogen Doping," Peking University, Beijing, 2015.
- [99] Y. Trenikhina, A. Grassellino, O. Melnychuk and A. Romanenko, "Characterization of Nitrogen Doping Recipes For the Nb SRF Cavities," in *Proceedings for SRF 2015*, Whistler, 2015.
- [100] J. P. Sethna and G. Catelani, "Temperature dependence of the superheating field for superconductors in the high-k London limit," *Physical Review B*, vol. 224509, p. 78, 2008.
- [101] A. Romanenko, "Breakthrough Technology for Very High Quality Factors in SRF Cavities," in *LINAC2014*, Geneva, 2014.
- [102] M. Merio, A. Crawford, A. Grassellino, A. Rowe, M. Wong, M. Checchin and M. Martinello, "Furnace N₂ Doping Treatments at Fermilab," in *Proceedings of SRF 2015*, Whistler, 2015.
- [103] J. Maniscalco, D. Gonnella, G. Hoffstaetter, P. Koufalis and M. Liepe, "Studies on the Field Dependence of the BCS Surface Resistance," in *Proceedings of IPAC 2016*, Busan, 2016.
- [104] G. Jouve, C. Severac and S. Cantacuzene, "XPS study of NbN and (NbTi)N Superconducting Coatings," *Thin Solid Films*, vol. 287, pp. 146-153, 1996.
- [105] E. Hand, "Can triniobium tin shrink accelerators?," *Nature*, p. 465, 2 12 2008.

- [106] D. Gonnella, R. Eichhorn, F. Furuta, M. Ge, T. Gruber, G. Hoffstaetter, J. Kaufman, P. Koufalis, M. Liepe and J. Maniscalco, "Improved N-Doping Protocols for SRF Cavities," in *Proceedings of IPAC 2016*, Busan, 2016.
- [107] D. Gonnella, T. Gruber, J. Kaufman, P. Koufalis, M. Liepe and J. Maniscalco, "Fundamental Studies on Doped SRF Cavities," in *Proceedings of SRF 2015*, Whistler, 2015.
- [108] D. Gonnella, F. Furuta, M. Ge, J. Kaufman, P. Koufalis, M. Liepe and J. Maniscalco, "Dependance of Surface Resistance on N-Doping Level," in *Proceedings of IPAC 2016*, Busan, 2016.
- [109] O. Florencio, P. S. d. S. Jr., T. Stefanini and C. Grandini, "Determination of the Oxygen and Nitrogen Interstitial Diffusion Coefficient in Niobium by Mechanical Spectroscopy," *Materials Research*, vol. 9, no. 4, pp. 431-434, 2006.
- [110] M. Bobra, "Niobium," *Symmetry*, 01 09 2005.
- [111] Cameca, "NanoSIMS application in materials research," Cameca, 2016. [Online]. Available: <http://www.cameca.com/applications/materials/ns-trace-element-yag.aspx>. [Accessed 11 January 2017].